Master of Science Thesis

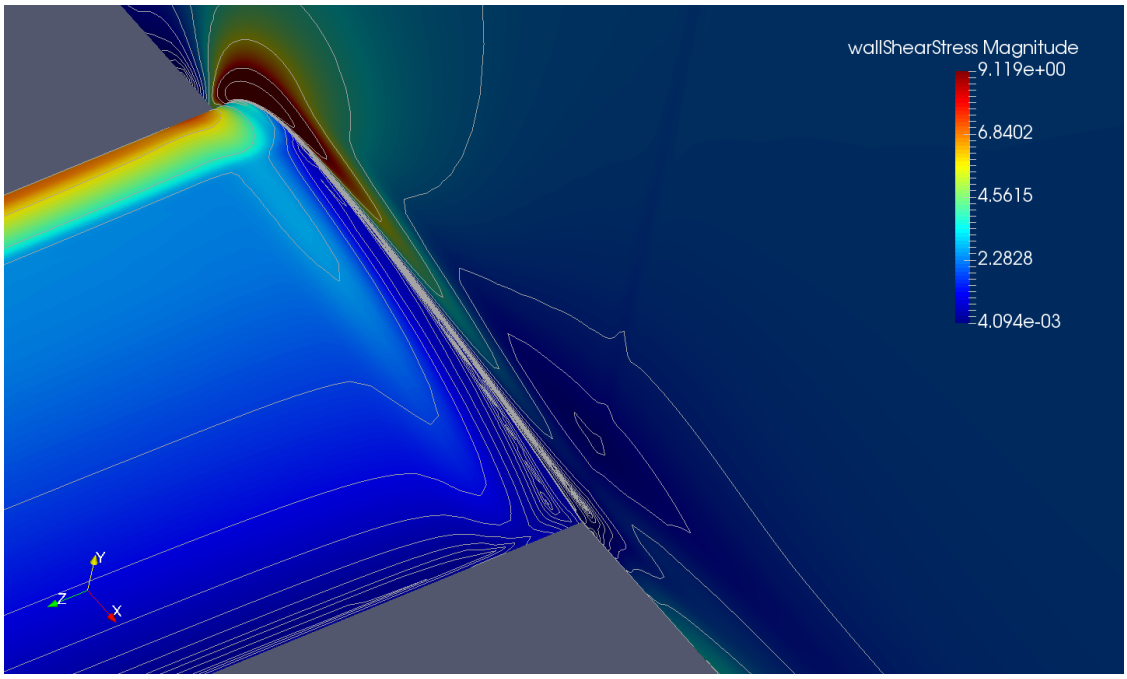

A Study of Global-Coefficient Non-Linear Eddy Viscosity Models

M.F. Döpke

March 29, 2018

Aerodynamics

Faculty of Aerospace Engineering

TU Delft

Delft University of Technology

A Study of Global-Coefficient Non-Linear Eddy Viscosity Models

Master of Science Thesis

For obtaining the degree of Master of Science in Aerospace Engineering
at Delft University of Technology

M.F. Döpke

March 29, 2018

Faculty of Aerospace Engineering · Delft University of Technology

Delft University of Technology

Copyright © Aerospace Engineering, Delft University of Technology
All rights reserved.

DELFT UNIVERSITY OF TECHNOLOGY
DEPARTMENT OF AERODYNAMICS

The undersigned hereby certify that they have read and recommend to the Faculty of Aerospace Engineering for acceptance the thesis entitled **"A Study of Global-Coefficient Non-Linear Eddy Viscosity Models"** by **M.F. Döpke** in fulfillment of the requirements for the degree of **Master of Science**.

Dated: March 29, 2018

Supervisors:

dr. R.P. Dwight

dr. S. Hickel

dr. G. Eitelberg

M. Schmelzer, M.Sc.

Preface

This Master of Science Thesis is the final part of my journey through the department of Aerodynamics at the Delft University of Technology. I have been blessed to be given this opportunity to work under the supervision of dr. Richard Dwight and Martin Schmelzer. I was granted much freedom to develop my skills, which at times was difficult when I was stuck and struggled to move forward. But whenever I asked for help Richard and Martin were both readily available to listen to my ideas and provide their input. I would like to thank you both for your direct and critical attitude towards my work. This has truly helped me second guess my conclusions and move forward in a meaningful way rather than wandering aimlessly through the world of turbulence modelling. I would also like to thank all the members of the "periodic hills club". I have much enjoyed working together with you and sharing our experiences. We have had some great moments watching each others presentations and talking over coffee breaks learning from each other. I would specially like to thank Mikael Kaandorp for helping me understand some machine learning concepts and Javier Fatou Gómez for the cooperation in working with OpenFOAM. At this point I also would like to thank dr. Alexander van Zuijlen for helping me set up and install my software on the work-station and cluster which I extensively used. I would like to thank my family for providing for me and granting me this opportunity to study abroad in Delft and always supporting me in my decisions. Last but not least I would like to thank my girlfriend for being there for me throughout my Masters. For helping me balance work and life and supporting me through moments of frustration and being there for moments of celebration.

Finally I would like to warn future students from working on turbulence modelling. You will lose your mind, if you are not up for a challenge don't do it. But if you are, the reward from understanding just a tiny bit more of this world is worth it. As the next step in my career I will move on to pursue a Ph.D. under the supervision of dr. Remco Hartkamp in Molecular Dynamics at the Delft University of Technology.

I hope you enjoy reading my Thesis.

Max Döpke
TU Delft
March 14, 2018

Abstract

In this research a global-coefficient non-linear eddy viscosity model (NLEVM) is studied. This model stems from the inherent inability of the Boussinesq approximation to model anisotropy and therefore flow features such as: swirl, stream-line curvature and secondary motions (Lumley, 1970; Pope, 1975; Craft et al., 1996). The focus lies on the limitations of using global-coefficients calibrated on a square-duct flow when applied on a rectangular-duct and a wing-body junction. The calibration is done with the Direct Numerical Simulation (DNS) results from Pinelli et al. (2010) at a Reynolds number of $Re = 1,100$. It is shown that using a global-coefficient NLEVM the velocity prediction on a square-duct and rectangular-duct is successfully corrected, i.e. secondary motions are present. On an attempt to improve the corner flow separation on a wing-body junction poor performance is observed. Stability issues led to only 3 models converge out of 21. Differently to Bordji et al. (2014) who found a large corner flow separation reduction with a Spalart-Allmaras Quadratic Constitutive Relation (SA-QCR) turbulence model when compared to a standard SA model, the global-coefficient NLEVM only showed limited corner flow separation reduction. Apart from correcting the anisotropy the near-wall resolution and treatment is found to be of large importance for flow field predictions. In the square- and rectangular-duct a wall damping function destroyed the secondary motion prediction, whilst in the wing-body junction improving the junction and corner flow prediction.

Table of Contents

List of Figures

List of Tables

Nomenclature

Abbreviations

ANN Artificial Neural Network
BFGS Broyden-Fletcher-Goldfarb-Shanno
CFD Computational Fluid Dynamics
CG Conjugate Gradient
CLS Craft, Launder and Suga
COBYLA Constrained Optimization By Linear Approximation
DNS Direct Numerical Simulation
EM Erhard and Moussiopoulos
HSV HorseShoe Vortex
kde Kernel Density Estimate
L-BFGS-B Limited Memory Broyden-Fletcher-Goldfarb-Shanno
LCL Lien, Chen and Leschziner
LES Large Eddy Simulation
M Million
MC Monte-Carlo
ML Machine Learning
NACA National Advisory Committee for Aeronautics
NASA National Aeronautics and Space Administration
NLEVM Non-Linear Eddy Visocisty Model
NM Nelder-Mead
NS Navier-Stokes
NY Nisizima and Yoshizawa
PIML Physics Informed Machine Learning
QCR Quadratic Constitutive Relationship
RANS Reynolds-Averaged Navier-Stokes
RB Rubinstein and Bartin
SA Spalart-Allmaras
SHN Shih and Lumley

SLSQP Sequential Least Squares Quadratic Programming
SZL Speziale and Ngo
TBNN Tensor Basis Neural Network
TBRF Tensor Basis Random Forest
TNC Truncated Newton Conjugate Gradient

Greek Symbols

α Closure coefficient for $k-\omega$ turbulence model
α_i Coefficient in tensor polynomial
β Global-coefficients of NLEVM
χ Non-dimensional kinematic turbulent viscosity
δ_{ij} Kronecker delta
ϵ_{ij}, ϵ_{kk} Strain rate tensor
γ_j Coefficient in tensor polynomial
κ Von Kárman constant
μ Dynamic viscosity
μ_s Shear modulus
ν Kinematic viscosity
ν_t Turbulent viscosity
ω Specific turbulence dissipation rate
Ω_a Cell area
Ω_{ij} Mean rotation rate
$\overline{\phi}$ Mean of a variable
ϕ' Perturbation of a variable
Π_{ij} Production tensor
ρ Density
$\rho_{(l,r)}$ Tensor alignment
σ Closure coefficient of SA turbulence model
σ_ω Closure coefficient for $k-\omega$ turbulence model
σ_ε Closure coefficient for $k-\varepsilon$ turbulence model
σ_k Closure coefficient for $k-\omega$ and $k-\varepsilon$ turbulence model
σ_{ij} Stress tensor
τ^* Time scale
τ_{ij} Reynolds stresses
$\tilde{\nu}$ Kinematic turbulent viscosity
ε Turbulence dissipation rate
ε_{ij} Turbulence dissipation rate tensor
ξ Ramping factor

Latin Symbols

$\tilde{S}_{ij}$ Mean strain rate

A_ν	Closure coefficient for wall damping
a_{ij}	Anisotropy tensor
AE	Closure coefficient for wall damping
B	Hessian matrix
C	Fourth order stiffness
c	Closure coefficient
C_μ	Closure coefficient for $k-\varepsilon$ turbulence model
C_D	Drag coefficient
C_{β^*}	Closure coefficient for $k-\omega$ turbulence model
C_β	Closure coefficient for $k-\omega$ turbulence model
$C_{\varepsilon 1}$	Closure coefficient for $k-\varepsilon$ turbulence model
$C_{\varepsilon 2}$	Closure coefficient for $k-\varepsilon$ turbulence model
c_{b1}	Closure coefficient of SA turbulence model
c_{b2}	Closure coefficient of SA turbulence model
C_{ijk}	Molecular and turbulent diffusion
E	Additional dissipation term
f_2	Wall damping function
f_μ	Wall damping function
f_i	Volume forcing
f_{t1}	Constitutive relationship of SA turbulence model
f_{t2}	Constitutive relationship of SA turbulence model
f_{v1}	Constitutive relationship of SA turbulence model
f_w	Constitutive relationship of SA turbulence model
h	Duct height or step height
K	Bulk modulus
k	Turbulent kinetic energy
l	Turbulent length scale
$L(x)$	Loss function
L_τ	Loss function in terms of Reynolds stress
l_m	Mixing length
L_U	Loss function in terms of velocity
n	Dimension
p	Pressure
p_k	Search direction at step k
$S1$	First order Sobol index
$S2$	Second order Sobol index
S_{ij}	Mean strain rate
ST	Total order Sobol index
t	Time
t^*	User defined input as iteration at which $\xi = 0.5$

t_i	Iteration
T_{ij}	Tensor
u	Velocity
u_m	Mixing velocity
y^*	Dimensionless wall distance
y^+	Dimensionless wall distance
$\mathbf{a}$	Vector
$\mathbf{b}$	Vector

Superscripts

$*$	Approximated
o	Exact

Chapter 1

Introduction

Computational Fluid Dynamics (CFD) has become an integral part in engineering and science. Three main types of CFD approaches exist, in order of decreasing computational cost; 1) Direct Numerical Simulations (DNS), 2) Large Eddy Simulations (LES) and 3) Reynolds-Averaged Navier-Sokes (RANS) simulations. DNS solves the Navier-Stokes (NS) equations exactly, involving no modelling of eddies. Whilst this method can be very accurate it requires to resolve flow features down to the Kolmogorov scale, meaning that the number of grid cells scales with $Re^{9/4}$ in three dimensions (Davidson, 2004). LES uses the scale separation approach modelling only the smallest encountered eddies whilst resolving the larger ones. This approach has received much development in the past decades, however Slotnick et al. (2014) describes it as impractical in the foreseeable future for industrial applications. Following Gatski and Jongen (2000) and more recently Slotnick et al., RANS is expected to remain the main workhorse of industry for the following decades. RANS solves the Navier-Stokes equation in a time averaged manner which requires the modeling of all turbulent scales in the form of the Reynolds stresses

$$\tau_{ij} = -\overline{u_i' u_j'}. \tag{1.1}$$

Whilst this expression can be solved with equation (A.33) and additional transport equations, it is most often modeled with the Boussinesq approximation (1.2) introduced in 2.2 (Schmitt, 2008).

$$\tau_{ij} = -\frac{2}{3}k\delta_{ij} + \nu_t \left(\frac{\partial u_i}{\partial x_j} + \frac{\partial u_j}{\partial u_i} - \frac{2}{3}\frac{\partial u_k}{\partial u_k}\delta_{ij} \right) \tag{1.2}$$

The Boussinesq approximation has served RANS turbulence modeling for many decades. It is mostly used in simulations at high Reynolds number on industrial test cases. These are mostly shear flow dominated with the goal of obtaining large scale flow features, i.e. average flow field (Slotnick et al., 2014). When the interest lies however on more detailed flow features, the Boussinesq approximation (1.2) has some well known deficiencies. It is known to be incapable of representing anisotropy, and therefore flow features such as: swirl, streamline curvature or secondary motions (Lumley, 1970; Craft et al., 1996). As a first

attempt to improve upon the anisotropy prediction Lumley (1970) proposed to expand the Boussinesq approximation using a tensor polynomial and including the mean rotation rates. Continuing on this idea Pope (1975) derived the most commonly known non-linear eddy viscosity model (NLEVM) for RANS. This model was proven to correct the anisotropy and improve predictions of streamline curvature, but was not extensively tested. Furthermore, Pope limited his derivation of the arising constitutive relations to two-dimensional flows. From this work many groups attempted to derive a non-linear eddy viscosity model that could serve as replacement for the Boussinesq approximation. However until today no universally good candidate has been found and eventually never will be. The turbulence problem was best put by Werner Heisenberg (1901-1976).

> *"When I meet God, I am going to ask him two questions: Why relativity? And why turbulence? I really believe he will have an answer for the first."*

The continuous search of an improved non-linear eddy viscosity model has generated a zoo of models of which little knowledge on universality and applicability exists. Whilst non-linear eddy viscosity models might predict better some flow features, they either under preform in the mean flow field or come at a too expensive cost compared to linear models. It was suggested by Edeling et al. (2014) that for a linear model "no single best choice of turbulence model or closure coefficients" exists. Then the model needs to be changed before calibration becomes relevant again.

In this introduction a state of the art literature review of turbulence modelling, machine learning and a relation from Reynolds stresses to secondary motions are provided. Finalizing the introduction with the research proposal and thesis outline.

1.1 State of the art

1.1.1 Non-linear eddy viscosity modelling and machine learning

The NASA CFD vision study (Slotnick et al., 2014) sees RANS modelling as the industry workhorse in 2030. This calls for further development in terms of uncertainty quantification and turbulence modelling. Here the state of the art of non-linear eddy viscosity modelling is presented.

Non-linear eddy viscosity models (NLEVM) have been derived due to the limitations of the Boussinesq approximation (1.2). Pope (1975) derived the most commonly known NLEVM by extending the one-term tensor representation given by the Boussinesq approximation to the generalized form of (2.35) and expressed the tensor basis in terms of the mean strain and rotation rates. Other NLEVM have been derived by Akira Yishizawa (1984), Speziale and Ngo (1987), Rubinstein and Barton (1990), Shih and Lumley (1993), Craft et al. (1996); Craft, Launder, and Suga (1997), Lien, Chen, and Leschziner (1996) and Wallin and Johansson

(2000). An overview of the models is given in table 2.1. The abundance of NLEVM and little agreement between closure coefficients stands as proof for the difficulty of effective turbulence modelling. Whilst these models on the calibrated test cases out-performed their linear counter parts (Boussinesq approximation), when applied to different flow cases the results were not always convincing.

From the lack of an improved general turbulence model Edeling et al. (2014) decided to quantify the uncertainties. They evaluated the posterior distributions of the linear Launder (1972) $k-\varepsilon$ turbulence model when calibrated against a variety of flow cases. This allowed them to create confidence intervals for the RANS result. Finally they concluded that the "the practice of tuning a set of deterministic closure coefficients for specific applications seems futile". The reasoning behind the conclusion was that the model error cannot be substantially reduced by parameter tuning. This author attributes this conclusion to the Boussinesq approximation, since the turbulence model used is inherently unable to predict anisotropy and therefore certain flow features. Also using a linear turbulence model Ling and Templeton (2015) developed markers to identify regions of high RANS uncertainty. They compared three common RANS assumptions by comparing RANS and DNS results: 1) non-negative eddy viscosity, 2) isotropic flow and 3) linear relationship between Reynolds stress and mean strain rate. They found that the first two assumptions were violated in most boundary layers and the third in regions of stream-line curvature. It is now clear that linear turbulence models using the Boussinesq approximation (1.2) fail to represent anisotropy and the model-form error cannot be substantially reduced. Then more advanced models need to be derived.

More advanced turbulence models exist in the form of Reynolds stress model's (RSM), however these suffer from robustness issues and the requirement to solve at least six additional transport equations. This increases the computational cost considerably giving only slightly better predictions. Other improved RANS turbulence models are the Explicit Algebraic Reynolds Stress Model's (EARSM) such as the Wallin and Johansson (2000) EARSM. These turbulence models use constitutive relationships to close the non-linear stress-strain relationship (2.35). Whilst they have shown improvements in anisotropy prediction at a reduced computational cost and improved robustness when compared to the RSM model's, they are still subject to calibration and can therefore not be universally used. Of course then to obtain better turbulence predictions a new approach needs to be proposed.

One step towards a new approach in turbulence modelling was the introduction of Machine Learning (ML) algorithms. One can understand these algorithms as an optimization problem such as least squares. A function is optimized given a specific set of training data. Two main approaches of implementing ML algorithms in turbulence modelling have been seen over the past years: 1. learning a functional form and 2. tuning a set of coefficients.

1. When learning a functional form the ML algorithm is provided with a set of inputs it can use to create a new function to replicate the training data. Pioneering work with this approach was done by Tracey (2015) whose algorithm learned the functional form of the Spalart and Allmaras (1992) (SA) turbulence model source term. Following Tracey's success Weatheritt and Sandberg (2016) proposed a gene expression program-

ming (GEP) algorithm intending to find a functional for the anisotropy using the tensors proposed by Pope (1975) from (2.36). This approach almost grants full freedom of the algorithm to impose a functional form. Due to dimensionality a constraint was set on the dimensional form.

2. In tuning coefficients the first works where presented by Duraisamy and Durbin (2014) who calibrated a multiplicative function added to the production term of a variation of the $k-\omega$ turbulence model given by Ge et al. (2014). Wu et al. (2016) and Xiao et al. (2016) constructed a calibration procedure where the Reynolds stresses would be corrected based on training data. As a result the calibration can only be used to predict flows on the same geometry. From the success of EARSM models Ling et al. (2016) used an Artificial Neural Network (ANN) to improve the anisotropy prediction using the tensor basis functions from Pope (1975) to imply invariance and local coefficients. However this type of ML was not very efficient when predicting flows in which different features than in the training data were present. Training on a very extensive set of flows would be required to make the model universally usable. Improving upon the lack of physics implemented in the ML process in the previous approaches Wang, Wu, and Xiao (2017) and Wang, Wu, Ling, et al. (2017) proposed a Physics Informed Machine Learning (PIML) algorithm in which a baseline Reynolds stress is corrected by a learned functional form. Their results on the square duct were very good. However no extrapolation towards different geometries was made, rendering the work incomplete. Kaandorp (2018) trained a random forest given anisotropy results from DNS simulations and input features from RANS results. This approach proved to be very successful in predicting flows similar to that used during training with less good results when applied to different flows.

1.1.2 Square duct and wing-body junction

The square duct and wing-body junction are two test cases on which the Boussinesq approximation is known to be inaccurate (Craft et al., 1996; Dandois, 2014; Bordji et al., 2014).

The secondary motions present in the form of corner vortices in the square duct cannot be reproduced with the Boussinesq approximation (1.2) due to the isotropy condition. The corner vortices are stress induced vortices generated by an imbalance of normal Reynolds stresses τ_{yy} and τ_{zz} as shown in expression (1.5). The implied isotropy condition in the Boussinesq approximation limits $\tau_{xx} = \tau_{yy} = \tau_{zz}$. Therefore the Boussinesq approximation fails in predicting secondary motions in the form of corner vortices in a square-duct flow.

On the wing-body junction the Boussinesq approximation is known to significantly overpredict the corner flow separation (Dandois, 2014). This flow is characterized by two orthogonal plates, similar as in a square duct. Bordji et al. (2014) and Bordji and Brunet (2015) compared the Spalart and Allmaras (1992) (SA) and Spalart (2000) and Allmaras Quadratic Constitutive Relationship (SA-QCR) turbulence models with an experiment. They found that at the leading edge both models preformed similarly, whilst at the trailing edge the SA-QCR model outperformed the SA model. This leads to believe that the corner flow region is

influenced by the quadratic constitutive relationship by which the Boussinesq approximation is expanded as shown in section 2.5.3.

Considering the corner region of the wing-body junction is similar to a square duct, the corner vortices from the square duct are thought to be of influence on the wing-body junction. This renders the square duct an ideal case on which to calibrate the NLEVM before predicting the wing-body junction.

1.1.3 Secondary motions

The main focus of using a non-linear eddy viscosity model is the ability to represent anisotropy. The Boussinesq approximation (1.2) assumes isotropic flow by constraining the Reynolds stresses τ_{ij} to the strain rate $S_{ij} = \frac{1}{2}\tau^* \left(\frac{\partial u_i}{\partial x_j} + \frac{\partial u_j}{\partial u_i}\right)$. This implies that $\tau_{xx} = \tau_{yy} = \tau_{zz}$. When using Lumley's anisotropy tensor it then follows that the anisotropy is zero. Let the anisotropy be defined by

$$a_{ij} = \frac{\tau_{ij}}{2k} - \frac{1}{3}\delta_{ij}, \tag{1.3}$$

with

$$k = \frac{1}{2}\left(\tau_{xx} + \tau_{yy} + \tau_{zz}\right). \tag{1.4}$$

Then the diagonals of $\tau_{ii}/2k = 1/3$ and of $a_{ii} = 0$. Introducing non-linear terms as is done in section 2.5 allows for $a_{ii} \neq 0$ and $\tau_{xx} \neq \tau_{yy} \neq \tau_{zz}$. This is a necessary condition in order to represent secondary motions in a square-duct flow. The vorticity equation in a square-duct can be expressed in terms of the Reynolds stresses following Emory (2014) as

$$\begin{gathered}\left(\frac{\partial^2}{\partial z^2} - \frac{\partial^2}{\partial y^2}\right)\tau_{yz} + \frac{\partial}{\partial y}\frac{\partial}{\partial z}\left(\tau_{yy} - \tau_{zz}\right) = \\ \left(\frac{\partial^2}{\partial y^2} - \frac{\partial^2}{\partial z^2}\right)\left(\nu_t\left(\frac{\partial u_y}{\partial z} + \frac{\partial u_z}{\partial y}\right)\right) + 2\frac{\partial}{\partial y}\frac{\partial}{\partial z}\left(\nu_t\left(\frac{\partial u_z}{\partial z} - \frac{\partial u_y}{\partial y}\right)\right).\end{gathered} \tag{1.5}$$

From (1.5) it can be seen that the Boussinesq approximation can only represent

$$\begin{gathered}\left(\frac{\partial^2}{\partial z^2} - \frac{\partial^2}{\partial y^2}\right)\tau_{yz} + \frac{\partial}{\partial y}\frac{\partial}{\partial z}\overbrace{\left(\tau_{yy} - \tau_{zz}\right)}^{\blacktriangleright 0} = \\ \left(\frac{\partial^2}{\partial y^2} - \frac{\partial^2}{\partial z^2}\right)\left(\nu_t\left(\frac{\partial u_y}{\partial z} + \frac{\partial u_z}{\partial y}\right)\right) + 2\frac{\partial}{\partial y}\frac{\partial}{\partial z}\left(\nu_t\left(\frac{\partial u_z}{\partial z} - \frac{\partial u_y}{\partial y}\right)\right).\end{gathered} \tag{1.6}$$

It is well documented that despite the possibility $\left(\frac{\partial^2}{\partial z^2} - \frac{\partial^2}{\partial y^2}\right)\tau_{yz} \neq 0$ no secondary motions are predicted with the Boussinesq approximation in a square duct. Perkins (1970) and Huser and Biringen (1993) argue that $\frac{\partial}{\partial y}\frac{\partial}{\partial z}\left(\tau_{yy} - \tau_{zz}\right)$ is the term responsible for vorticity generation in a square-duct. Therefore in order to represent vorticity the expansion of the Boussinesq approximation to (2.35) is required such that $\tau_{yy} \neq \tau_{zz}$.

1.2 Proposal

In this research the use of global-coefficients is proposed opposed to local coefficients as in Wang, Wu, Ling, et al. (2017), Ling et al. (2016) and Kaandorp (2018). This will reduce the accuracy, but might increase solver robustness. It does have the potential to an easier to implement and use model. This approach is not expected to be universally superior to linear models, but only to investigate the limitations of using global coefficients. The coefficients are calibrated on a square duct in which linear models are known to fail to predict secondary motions. Then the model is used to predict rectangular-duct flow and the corner flow separation of a wing-body junction. From (Dandois, 2014) and (Bordji et al., 2014) it is known that a non-linear eddy viscosity model predicts a more realistic corner flow separation. From the calibration procedure the model will be tuned to predict secondary motions in a corner region which should in return predict a more accurate corner flow separation on a wing-body junction. Due to the use of global coefficients, the mean flow field and other flow features might suffer.

1.3 Thesis outline

The aim of this research project is to further develop the understanding of non-linear eddy viscosity modelling and explore the boundaries of global coefficient calibration approaches using data driven machine learning. Once calibrated the model will be used to on a rectangular-duct flow and wing-body junction to study its predictive capabilities. This research shall stand as a stepping stone and further confirmation that brute force data driven machine learning techniques can provide high accuracy results without the need to resolve to costlier and more complex models. It is aimed to increase the accuracy of the flow solution in terms of secondary motions without a considerable increase in computational cost.

The main project goals can be summarised into several research questions and sub-questions:

- *What are the predictive capabilities of a global-coefficient eddy viscosity model?*
  - *Can the anisotropy be corrected?*
  - *Can secondary motions be predicted?*
  - *Can corner flow separation be reduced?*
- *What are the limitations of data driven machine learning techniques for calibration?*
- *Are secondary motions the driver of corner flow separation?*

The aim of this research is to explore the boundaries of accuracy of using a global-coefficient non-linear eddy viscosity model. This will be explored by training the models coefficients using direct numerical simulation results of a square-duct flow case at a Reynolds numbers of 1100. Different optimization routines will be used in exploring the coefficient space. The

global-coefficient NLEVM model will be applied to a rectangular-duct to investigate the predictive capabilities on a similar flow to judge its performance in terms of overall accuracy and secondary motion prediction. As a far fetched attempt it will also be applied to the wing-body junction to observe the corner flow separation prediction.

The remainder of this Thesis is organized as follows. In chapter 2 RANS turbulence modelling is introduced. In chapter 3 the methods and techniques used throughout this research are presented. Also the test cases used are described in this chapter. The global-coefficient NLEVM calibration procedure is split into two approaches, 1) data-driven and 2) solver-incorporated calibration presented in chapters 4 and 5 respectively. Chapters 6 and 7 display the predictive capabilities and limitations of a global non-linear eddy viscosity model on a rectangular duct and wing-body junction respectively. Finally conclusions and recommendations are presented in chapter 8.

Chapter 2

Reynolds-Averaged Navier-Stokes non-linear eddy viscosity turbulence modeling

The Navier-Stokes (NS) equations describe the motion of Newtonian fluids under the continuum hypothesis. Whilst solving these equations would represent the physics exactly, it is prohibitively expensive. Direct Numerical Simulations (DNS) require the mesh to resolve features down to the Kolmogorov scale, meaning that the number of grid cells scales with $Re^{9/4}$ (Davidson, 2004). This limits DNS to small Reynolds numbers, $Re \sim 5000$, and simple geometries. An alternative to solving the NS equations exactly is Reynolds-Averaged Navier-Stokes (RANS) modelling. As the name implies, there is averaging in the process. RANS equations are derived by splitting the flow into a mean velocity $\bar{u}$ with perturbation u' such that $u = \bar{u} + u'$. Where it is assumed that the time averages of the perturbation are zero such that $\overline{u'} = 0$.

The NS continuity and momentum equations for Newtonian fluids in differential form using Einstein summation convention are

$$\frac{\partial \rho}{\partial t} + \frac{\partial (\rho u_i)}{\partial x_i} = 0, \tag{2.1}$$

$$\frac{\partial (\rho u_i)}{\partial t} + \frac{\partial (\rho u_i u_j)}{\partial x_j} = -\frac{\partial p}{\partial x_i} + \frac{\partial}{\partial x_j}\left[\mu\left(\frac{\partial u_i}{\partial x_j} + \frac{\partial u_j}{\partial x_i}\right)\right] + \rho f_i. \tag{2.2}$$

Throughout this research only incompressible flows are being considered. This means no changes in density $\frac{\partial \rho}{\partial t} = 0$ and $\frac{\partial \rho}{\partial x} = 0$. Furthermore, no volume forcing f_i is considered. Then the NS equations for incompressible Newtonian fluid divided by the density ρ are

$$\frac{\partial u_i}{\partial x_i} = 0, \tag{2.3}$$

$$\frac{\partial u_i}{\partial t} + \frac{\partial u_i u_j}{\partial x_j} = -\frac{1}{\rho}\frac{\partial p}{\partial x_i} + \frac{\partial}{\partial x_j}\left[\nu\left(\frac{\partial u_i}{\partial x_j} + \frac{\partial u_j}{\partial x_i}\right)\right]. \tag{2.4}$$

In this chapter turbulence modelling for RANS is introduced starting at the derivation of the RANS momentum equation in section 2.1. In section 2.2 the Boussinesq approximation is

presented. Boussinesq approximation based turbulence models with corresponding transport equations are discussed in section 2.3. The non-linear expansion to the Boussinesq approximation derived by Pope (1975) is presented in section 2.4. Turbulence models using this expansion are presented in section 2.5. Turbulence models using the Reynolds stress transport equation are given in section 2.6. Finally a discussion of turbulence modelling with a view into the greater picture of RANS turbulence models is presented in section 2.7.

2.1 Momentum equation

The RANS momentum equation is obtained from splitting the flow into mean $\bar{u}$ and perturbation u' and applying time averaging as explained in appendix A. Applying this strategy to the incompressible NS momentum equation (2.4) yields

$$\bar{u}_j \frac{\partial \bar{u}_i}{\partial x_j} = -\frac{1}{\rho}\frac{\partial \bar{p}}{\partial x_j} + \frac{\partial}{\partial x_j}\left[\nu\left(\frac{\partial \bar{u}_i}{\partial x_j} + \frac{\partial \bar{u}_j}{\partial x_i}\right) - \overline{u_i' u_j'}\right]. \tag{2.5}$$

This equation is very similar to (2.4), with an additional term $\tau_{ij} = \overline{u_i' u_j'}$. This additional term is the Reynolds stress tensor which accounts for the momentum transfer between the turbulent and mean flow scales.

From the derivation of (2.5) τ_{ij} is an unknown which needs to be specified. This is typically achieved through a stress-strain relationship and a set of additional transport equations.

2.2 Linear stress-strain relationship

Stress-strain relationships relate the stress and strain of an infinitesimal body. In linear elasticity this relation is known as Hooke's law and is formulated as $\sigma = C : \epsilon$ where σ is the stress tensor, ϵ the strain tensor and C the fourth order stiffness. For homogeneous isotropic materials Hooke's law is defined by the bulk modulus K, shear modulus μ, Kronecker delta δ_{ij} and strain rates

$$\epsilon_{ij} = \frac{1}{2}\left(\frac{\partial u_i}{\partial x_j} + \frac{\partial u_j}{\partial u_i}\right), \tag{2.6}$$

$$\epsilon_{kk} = \frac{\partial u_k}{\partial x_k} \tag{2.7}$$

as

$$\sigma_{ij} = K\epsilon_{kk}\delta_{ij} + 2\mu_s\left(\epsilon_{ij} - \frac{1}{3}\epsilon_{kk}\delta_{ij}\right). \tag{2.8}$$

A similar logic can be applied to fluids. Considering a volume of fluid, the stress and strain will relate following Hooke's law (2.8). However, since it is a fluid instead of using the shear modulus μ_s the viscosity ν should be used. Both these quantities describe the resistance of a

body to deformation. The bulk modulus K, which expresses the resistance to compressibility is changed for the turbulent kinetic energy k which is the root-mean-square of the velocity fluctuations $k = \frac{1}{2}\overline{u_i' u_j'}$. The resulting expression from this analysis is known as the Boussinesq approximation (Schmitt, 2008)

$$\tau_{ij} = -\frac{2}{3}k\delta_{ij} + \nu_t \left(\frac{\partial u_i}{\partial x_j} + \frac{\partial u_j}{\partial u_i} - \frac{2}{3}\frac{\partial u_k}{\partial x_k}\delta_{ij} \right). \tag{(1.2)}$$

Note that $\frac{\partial u_k}{\partial x_k} = 0$ for incompressible flows.

2.3 Linear eddy viscosity models

In this section linear eddy viscosity models are presented. The term linear arises from the use of the linear stress-strain relationship (1.2). Closing the Boussinesq approximation requires the specification of the turbulent viscosity ν_t. It is important to note that ν_t is a flow property and not a fluid property. Which means that ν_t can vary a lot from flow to flow and within the same flow. In this section Boussinesq based zero-equation to two-equation models are presented.

2.3.1 Zero-equation models

Prandtl (1925) postulated the mixing length theory by making relation to kinetic gas theory. He assumed that turbulent eddies cling together and maintain their momentum for a distance l_m propelled at a turbulent velocity u_m. The mixing velocity u_m is further assumed to be equal to the fluctuating velocity of the molecules $u_m = u' = l_m|du/dy|$. From dimensional analysis it is known that the turbulent viscosity has units m^2/s. Then the mixing length turbulent viscosity is written as

$$\nu_t \propto l_m^2 \left| \frac{du}{dy} \right|. \tag{2.9}$$

Models based on Prandtl's mixing length theory are called zero equation models or algebraic models, not to be confused with Reynolds Stress Models (RSM). Algebraic models make use of algebraic relations and empiricism to determine the mixing length l_m. The need to specify l_m limits the generality and applicability of this approach. Celik (1999) and White (1991) provide a nice overview of mixing length models to be used in different flow conditions.

2.3.2 One-equation models

As an alternative for the mixing velocity $u_m = u' = l_m|du/dy|$ the square root of the turbulent kinetic energy k has been proposed. This appears a logical choice given that

$k = 1/2\left(\overline{u'u'} + \overline{v'v'} + \overline{w'w'}\right)$ is the square root of the root-mean-square of the fluctuations. Then the turbulent viscosity is defined as

$$\nu_t \propto k^{1/2} l_m. \tag{2.10}$$

This approach requires however the modelling an additional transport equation for k. This equation is derived in appendix A by taking the trace of the Reynolds stress tensor (A.34) yielding

$$\frac{\partial k}{\partial t} + \bar{u}_j \frac{\partial k}{\partial x_j} = \underbrace{\tau_{ij} \frac{\partial \bar{u}_i}{\partial x_j}}_{\text{Production}} - \underbrace{\nu \overline{\frac{\partial u_i'}{\partial x_k} \frac{\partial u_i'}{\partial x_k}}}_{\text{Dissipation}} + \frac{\partial}{\partial x_j} \left[\underbrace{\nu \frac{\partial k}{\partial x_j}}_{\text{Diffusion}} - \underbrace{\frac{1}{\rho} \overline{p' u_j'} - \frac{1}{2} \overline{u_i' u_i' u_j'}}_{\text{Energytransport}} \right]. \tag{2.11}$$

In this expression the terms on the left-hand side are the rate of change and convective transport of k. On the right-hand side the terms represent the production, dissipation, diffusion and energy transport. The first two terms on the right hand side are a source and sink terms respectively by which turbulent kinetic energy is produced and destroyed. The last two terms represent transport terms that redistribute the turbulent kinetic energy.

The production term represents the kinetic energy an eddy gains due to the mean flow. This term acts as the source. The dissipation represents the energy transfer from the smallest eddies to thermal energy. This term acts as a sink. The third term represents the molecular diffusion of turbulent energy. The energy transport has two parts, transport due to turbulent fluctuations and transport from redistribution of pressure fluctuations.

In order to solve equation (2.11) some correlation for the production, dissipation, turbulent diffusion and pressure diffusion need to be specified. For the Reynolds stresses τ_{ij} in the production term the Boussinesq approximation (1.2) is used. The eddy viscosity is closed with (2.10) and a constant of proportionality C_μ as

$$\nu_t \approx C_\mu k^{1/2} l. \tag{2.12}$$

The dissipation and production terms are balanced as

$$-\overline{u_i' u_j'} \frac{\partial \bar{u}_i}{\partial x_j} = \nu \overline{\frac{\partial u_i'}{\partial x_k} \frac{\partial u_i'}{\partial x_k}} = \varepsilon. \tag{2.13}$$

From dimensional analysis the above expression has units m^2/s. The dissipation can be expressed by

$$\varepsilon \propto \frac{u^3}{l}. \tag{2.14}$$

This is also in accordance with White (1991) who used physical reasoning to derive the dissipation. White described the dissipation to be proportional to a velocity u times drag $\rho u^2 l^2$ divided by the mass ρl^3. Taking as characteristic velocity the turbulent kinetic energy and as constant of proportionality the drag coefficient C_D, White's dissipation is defined by

$$\varepsilon \approx C_D \frac{k^{3/2}}{l}. \tag{2.15}$$

This expression has the same units as (2.14) m^2/s.

The pressure diffusion and turbulent fluctuations are modeled assuming a gradient diffusion transport mechanism

$$\frac{\nu_t}{\sigma_k}\frac{\partial k}{\partial x_j} = -\frac{1}{2}\overline{u_i' u_i' u_j'} - \frac{1}{\rho}\overline{p' u_j'}. \tag{2.16}$$

The modelled k equation can then be written as

$$\frac{\partial k}{\partial t} + \bar{u}_j\frac{\partial k}{\partial x_j} = \tau_{ij}\frac{\partial \bar{u}_i}{\partial x_j} - \varepsilon + \frac{\partial}{\partial x_j}\left[\left(\nu + \frac{\nu_t}{\sigma_k}\right)\frac{\partial k}{\partial x_j}\right]. \tag{2.17}$$

To close the turbulent kinetic energy the coefficients C_μ or C_D and σ_k are specified from a calibration procedure. The length scale l is defined algebraically depending on the flow properties. l is in many ways determined in a similar fashion as l_m from the algebraic models. This last step is the largest source of error and difficulty in use of one-equation turbulence models.

Spalart-Allmaras turbulence model

The Spalart-Allmaras (SA) turbulence model is a one-equation model that does not solve the turbulent kinetic energy k but rather the kinematic turbulent viscosity $\tilde{\nu}$. This model was derived by Spalart and Allmaras (1992) for aerospace applications, specifically wall-bounded flows. The model is characterized by the transport equation for the kinematic turbulent viscosity $\tilde{\nu}$

$$\begin{aligned}\frac{\partial \tilde{\nu}}{\partial t} + u_j\frac{\partial \tilde{\nu}}{\partial x_j} &= c_{b1}(1-f_{t2})\tilde{S}\tilde{\nu} \\ &- \left[c_{w1}f_w - \frac{c_{b1}}{\kappa^2}f_{t2}\right]\left(\frac{\tilde{\nu}}{d}\right)^2 + \frac{1}{\sigma}\left[\frac{\partial}{\partial x_j}\left((\nu+\tilde{\nu})\frac{\partial \tilde{\nu}}{\partial x_j}\right) + c_{b2}\frac{\partial \tilde{\nu}}{\partial x_i}\frac{\partial \tilde{\nu}}{\partial x_i}\right] + f_{t1}\Delta U^2.\end{aligned} \tag{2.18}$$

The turbulent viscosity is defined as

$$\nu_t = \tilde{\nu} f_{v1} \tag{2.19}$$

with

$$f_{v1} = \frac{\chi^3}{\chi^3 + c_{v1}^3} \tag{2.20}$$

and

$$\chi = \frac{\tilde{\nu}}{\nu}. \tag{2.21}$$

In order to solve (2.18) a series of additional terms and closure coefficients are defined as specified in Spalart and Allmaras (1992).

2.3.3 Two-equation models

Most one-equation models still suffer from the need to specify a turbulent length scale. Two-equation models model the turbulent kinetic energy and some length scale or equivalent parameter. In essence this fully closes the problem of turbulent viscosity. This does not mean it is exact. Most two-equation models make the assumption of balancing turbulent production and dissipation and use the Boussinesq approximation to close the Reynolds stresses. This implies that the turbulent length scales are locally proportional to the scales of the mean flow (Celik, 1999). This assumption is only valid on equilibrium flows. The additional variable that is solved with two-equation models is generally the turbulent dissipation rate ε or the specific turbulent dissipation rate ω. Each variable gives rise to its own turbulence model, which are the most commonly used turbulence models in industry, the $k-\varepsilon$ and $k-\omega$ models (Argyropoulos & Markatos, 2015).

Using the Boussinesq approximation implies that the turbulent fluctuations u', v' and w' are locally equal. Thereby enforcing isotropy. The second fundamental assumption is the balancing of local turbulent production and dissipation

$$\tau_{ij}\frac{\partial \bar{u}_i}{\partial x_j} = \nu\overline{\frac{\partial u_i'}{\partial x_k}\frac{\partial u_i'}{\partial x_k}}. \tag{2.22}$$

To allow the Reynolds stresses to be calculated using local scales it is assumed that the production equals the dissipation in the k equation such that $\varepsilon = \tau_{ij}S_{ij}$. Considering for τ_{ij} the Boussinesq approximation (1.2) and using dimensional reasoning the turbulent viscosity is estimated to be

$$\nu_t \propto \frac{k^2}{\varepsilon}, \tag{2.23}$$

for the $k-\varepsilon$ model and for the $k-\omega$ model

$$\nu_t \propto \frac{k}{\omega}. \tag{2.24}$$

The $k-\varepsilon$ model solves as additional transport equation the turbulence dissipation ϵ. The $k-\omega$ model solves as additional transport equation the specific turbulence dissipation ω equation. The k equations for both, the $k-\varepsilon$ and $k-\omega$ models are similar as for the one-equation model. With the variation of some coefficients.

The $k-\varepsilon$ model

The $k-\varepsilon$ turbulence model as expressed in Launder (1972); Launder and Spalding (1974) is by far the most widely used two equation turbulence model. It defines the turbulent viscosity as

$$\nu_t = C_\mu\frac{k^2}{\varepsilon}. \tag{2.25}$$

The additional transport equation solved is for the turbulent dissipation ε. It is obtained from applying the operator $2\nu\frac{\partial u_i'}{\partial x_k}\frac{\partial}{\partial x_k}$ on the incompressible NS equations as shown in appendix

A.5. The modelled turbulence dissipation rate equation neglecting higher order interactions is

$$\frac{\partial \varepsilon}{\partial t} + \bar{u}_j \frac{\partial \varepsilon}{\partial x_j} = \frac{\partial}{\partial x_j}\left[\left(\nu + \frac{\nu_t}{\sigma_\varepsilon}\right)\frac{\partial \varepsilon}{\partial x_j}\right] + C_{\varepsilon 1}\frac{\varepsilon}{k}\tau_{ij}\frac{\partial \bar{u}_i}{\partial x_j} - C_{\varepsilon 2}\frac{\varepsilon^2}{k}. \tag{2.26}$$

The modelled k equation is given by

$$\frac{\partial k}{\partial t} + \bar{u}_j \frac{\partial k}{\partial x_j} = \tau_{ij}\frac{\partial \bar{u}_i}{\partial x_j} - \varepsilon + \frac{\partial}{\partial x_j}\left[\left(\nu + \frac{\nu_t}{\sigma_k}\right)\frac{\partial k}{\partial x_j}\right]. \tag{2.27}$$

The closure coefficients are determined by calibration and physical reasoning as

$$C_\mu = 0.09,\ C_{\varepsilon 1} = 1.44,\ C_{\varepsilon 2} = 1.92,\ \sigma_\varepsilon = 1.3,\ \text{ and } \sigma_k = 1.0.$$

The $k-\omega$ model

The $k-\omega$ model as expressed in Wilcox (1994a) is the second most used two-equation turbulence model. This one solves the specific turbulence dissipation as

$$\omega = c\frac{\sqrt{k}}{l} \tag{2.28}$$

with c being a constant of proportionality and l a turbulent length scale. This model can roughly be stated to be related to the $k-\varepsilon$ turbulence model with the dimensional relation $\omega \propto k/\varepsilon$. The turbulent viscosity is defined as

$$\nu_t = \frac{k}{\omega}. \tag{2.29}$$

The additional transport equation solves the specific turbulence dissipation ω as

$$\frac{\partial \omega}{\partial t} + \bar{u}_j \frac{\partial \omega}{\partial x_j} = \frac{\partial}{\partial x_j}\left[(\nu + \sigma\nu_t)\frac{\partial \omega}{\partial x_j}\right] + \alpha\frac{\omega}{k}\tau_{ij}\frac{\partial \bar{u}_i}{\partial x_j} - C_\beta\omega^2. \tag{2.30}$$

This equation is derived from physical reasoning considering the processes of convection, diffusion, production $\alpha\frac{\omega}{\rho k}\tau_{ij}\frac{\partial \bar{u}_i}{\partial x_j}$ and dissipation $C_\beta\omega^2$. The k equation for the $k-\omega$ model is given by

$$\frac{\partial k}{\partial t} + \bar{u}_j \frac{\partial k}{\partial x_j} = \alpha\frac{\omega}{k}\tau_{ij}\frac{\partial \bar{u}_i}{\partial x_j} - C_{\beta^*}\omega k + \frac{\partial}{\partial x_j}\left[\left(\nu + \frac{\nu_t}{\sigma_\omega}\right)\frac{\partial k}{\partial x_j}\right]. \tag{2.31}$$

The closure coefficients are given by

$$C_{\beta^*} = 9/100,\ \alpha = 5/9,\ C_\beta = 3/40,\ \sigma_\omega = 1/2,\ \text{ and } \sigma_k = 1/2.$$

2.4 Non-linear stress-strain relationship

The Boussinesq approximation (1.2) is known to have some deficiencies. Specifically when representing flows with strong separation, stream line curvature, recirculation or swirls. This

deficiency can best be explained when observing the anisotropy introduced by Lumley (1970)

$$a_{ij} = \frac{\tau_{ij}}{2k} - \frac{1}{3}\delta_{ij}. \tag{1.3}$$

It has been pointed out by several authors including Lumley (1970) and Pope (1975) that the Boussinesq approximation is inadequate for flows that exhibit such behaviour since it assumes the fluid to be isotropic. Which is an invalid assumption for these kind of flow phenomena. Harris et al. (1977) measured the anisotropy in a nearly homogeneous shear flow to be

$$a_{xx} = 0.3,\ a_{yy} = -0.18,\ a_{zz} = -0.12 \text{ and } a_{xy} = 0.33.$$

Where the Boussinesq approximation (1.2) is at best able to predict

$$a_{xx} = a_{yy} = a_{zz} = 0 \text{ and } a_{xy} = 0.33.$$

On a barycentric map introduced by Banerjee et al. (2007), figure 2.1, the DNS results from a square duct exhibit mostly 1-component turbulence, whilst the Boussinesq approximation is only capable of predicting plain strain. Barycentric maps are explained in appendix D.

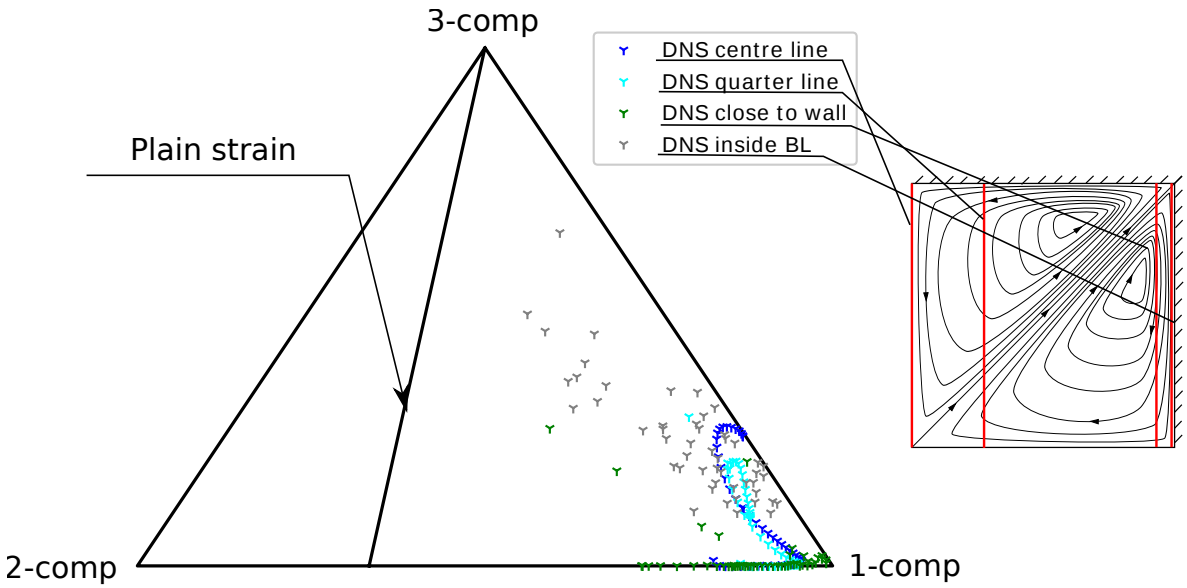

Figure 2.1: Anisotropy representation on a Barycentric map of the square duct

The inability of the Boussinesq approximtion to capture $a_{xx} \neq a_{yy} \neq a_{zz} \neq 0$ can be explained from the theory used behind the derivation. Boussinesq (1877) assumed that a fluid would behave similarly as a material and made a relation based on the mean strain without considering the rotation. Lumley (1970) showed that the rotation effects $\Omega_{ij} = 1/2\tau^* \left(\frac{\partial u_i}{\partial x_j} - \frac{\partial u_j}{\partial u_i}\right)$ cannot be neglected for a gas and went on to deriving a different stress-strain relationship as a function of the strain rate

$$S_{ij} = \frac{1}{2}\tau^* \left(\frac{\partial u_i}{\partial x_j} + \frac{\partial u_j}{\partial x_i}\right) \tag{2.32}$$

and the rotation rate

$$\Omega_{ij} = \frac{1}{2}\tau^* \left(\frac{\partial u_i}{\partial x_j} - \frac{\partial u_j}{\partial x_i} \right) \tag{2.33}$$

using tensor polynomial expansion. The time scale τ^* is used to non-dimensionalize the strain and rotation rates. The most general form of a tensor polynomial is given by

$$\tau_{ij} = \Pi_{i=0}^{\infty}\Pi_{\alpha_i=0}^{\infty}\Pi_{j=0}^{\infty}\Pi_{\gamma_j=0}^{\infty}\beta_{\gamma_1,\gamma_2,\dots}^{\alpha_1,\alpha_2,\dots} S^{\alpha_1}\Omega^{\gamma_1}S^{\alpha_2}\Omega^{\gamma_2}.... \tag{2.34}$$

This tensor polynomial provides an infinite polynomial to describe the Reynolds stress tensor τ_{ij}. Since τ_{ij} is symmetric and has zero trace, only expansions fulfilling those criteria need to be considered. Using the Caley-Hamilton theorem and following the derivation in appendix B, the expression can be simplified to a finite set of linearly independent second-order tensors. Pope (1975) derived the most commonly known non-linear stress-strain relationship in turbulence modeling

$$\tau_{ij} = -\frac{2}{3}k\delta_{ij} + 2\nu_t S_{ij} + k\sum_n \beta^{(n)} T_{ij}^{(n)}. \tag{2.35}$$

T_{ij} represent the tensors expressed in (2.36). The additional terms β represent functions in terms of the invariants $S_{ik}S_{kj}$, $\Omega_{ik}\Omega_{kj}$, $S_{ik}S_{km}S_{mj}$, $\Omega_{ik}\Omega_{km}S_{mj}$ and $\Omega_{ik}\Omega_{km}S_{mn}S_{nj}$.

$$\begin{aligned}
T_{ij}^{(1)} =& S_{ik}\Omega_{kj} - \Omega_{jk}S_{ki} \\
T_{ij}^{(2)} =& S_{ik}S_{kj} - \frac{1}{3}\{S_{km}S_{mk}\}\delta_{ij} \\
T_{ij}^{(3)} =& \Omega_{ik}\Omega_{kj} - \frac{1}{3}\{\Omega_{km}\Omega_{mk}\}\delta_{ij} \\
T_{ij}^{(4)} =& \Omega_{ik}S_{km}S_{mj} - S_{ik}S_{km}\Omega_{mk} \\
T_{ij}^{(5)} =& \Omega_{ik}\Omega_{km}S_{mj} + S_{ik}\Omega_{km}\Omega_{mj} - \frac{2}{3}\{S_{km}\Omega_{mn}\Omega_{nk}\}\delta_{ij} \\
T_{ij}^{(6)} =& \Omega_{ik}S_{km}\Omega_{mn}\Omega_{nj} - \Omega_{ik}\Omega_{km}S_{mn}\Omega_{nj} \\
T_{ij}^{(7)} =& S_{ik}\Omega_{km}S_{mn}S_{nj} - S_{ik}S_{km}\Omega_{mn}S_{nj} \\
T_{ij}^{(8)} =& \Omega_{ik}\Omega_{km}S_{mn}S_{nj} + S_{ik}S_{km}\Omega_{mn}\Omega_{nj} - \frac{2}{3}\{S_{km}S_{mn}\Omega_{nl}\Omega_{lk}\}\delta_{ij} \\
T_{ij}^{(9)} =& \Omega_{ik}S_{km}S_{mn}\Omega_{nl}\Omega_{lj} - \Omega_{ik}\Omega_{km}S_{mn}S_{nl}\Omega_{lj}
\end{aligned} \tag{2.36}$$

2.5 Non-linear eddy viscosity models

Non-linear eddy viscosity models are derived from the linear eddy viscosity models using instead of Boussinesq approximation (1.2) the non-linear stress strain relationship (2.35) to express the Reynolds stress tensor. This substitution can either be complete, using all tensors, or partial, using a subset of the tensors. Although non-linear eddy viscosity models have been derived for many turbulence models, in this section only those derived from the $k-\varepsilon$, $k-\omega$ and SA turbulence models are discussed.

2.5.1 Non-linear $k-\varepsilon$ turbulence models

Over the years a variety of non-linear $k-\varepsilon$ non-linear eddy viscosity models have been developed. Some of the most common models are presented in table 2.1. The coefficients β in table 2.1 correspond to the tensors from (2.36) with the exemptions of β_6 and β_7 which correspond to

$$T_{ij}^{(6)} = S_{ij}S_{kl}S_{kl} \tag{2.37}$$

and

$$T_{ij}^{(7)} = S_{ij}\Omega_{kl}\Omega_{kl}. \tag{2.38}$$

Nisizima and Yoshizawa (1987) (NZ) derived a quadratic relationship for the Reynolds stress tensor from a statistical viewpoint using two-scale direct interaction formalism. Speziale and Ngo (1987) (SZL) derived a similar expression plus an Oldroyd derivative term (2.39) using the material frame indifference, realizability and invariance requirements. Rubinstein and Barton (1990) (RB) used the theory of renormalization group to derive yet another quadratic model from the Yakhot and Orszag (1986) theory. Shih and Lumley (1993) (SHN) derived closure coefficients using up to the quadratic terms proposed by Pope (1975) and Craft et al. (1996, 1997) (CLS) using up to the cubic terms. Lien et al. (1996) (LCL) expanded upon Shih and Lumley's work, adding cubic terms and expressions for the respective additions. Ehrhard and Moussiopoulos (2000) recalibrated the Lien model for flow around buildings.

The Lien model also includes a wall damping function f_μ for near wall treatment. This damping function takes the value of unity far away from the wall and approaches 0 towards the wall. f_μ is expressed in terms of the dimensionless wall distance $y^* = \frac{k^{1/2}y}{\nu}$ and coefficients C_μ, κ and A_ν as

$$f_\mu = [1-\exp(-A_\nu y^*)]\left[1+\frac{2\kappa}{c_\mu^{0.75}y^*}\right]. \tag{2.42}$$

This damping function is included in the $k-\varepsilon$ model by multiplying the turbulent viscosity

$$\nu_t = C_\mu f_\mu \frac{k^2}{\varepsilon}. \tag{2.43}$$

This upsets the balance of turbulence production and dissipation near the wall (Launder & Spalding, 1974). In order to keep the production and dissipation balance assumption the modelled energy dissipation equation (2.26) is modified to (2.46) by introducing an additional term

$$E = C_{\varepsilon 2}C_\mu^{0.75}f_2\sqrt{k}\varepsilon\frac{1+\frac{2\kappa}{c_\mu^{0.75}}}{\kappa y}\exp\left(-AEy^{*2}\right) \tag{2.44}$$

and damping function

$$f_2 = 1-0.3\exp\left(-\left(\frac{k^2}{\nu\varepsilon}\right)^2\right) \tag{2.45}$$

yielding

$$\frac{\partial\varepsilon}{\partial t}+\bar{u}_j\frac{\partial\varepsilon}{\partial x_j} = \frac{\partial}{\partial x_j}\left[\left(\nu+\frac{\nu_t}{\sigma_\varepsilon}\right)\frac{\partial\varepsilon}{\partial x_j}\right]+C_{\varepsilon 1}\frac{\varepsilon}{\rho k}\tau_{ij}\frac{\partial\bar{u}_i}{\partial x_j}-C_{\varepsilon 2}f_2\frac{\varepsilon^2}{k}+E. \tag{2.46}$$

Table 2.1

	NY	SZL	RB	SHN	CLS	LCL	EM
C_μ	0.09	0.09	0.0845	$\frac{2/3}{1.25+\bar{S}+0.9\bar{\Omega}}$	(2.40)	$\frac{2/3}{1.25+\bar{S}+0.9\bar{\Omega}}$	(2.41)
β_1	0.72		0.56	$\frac{15}{1000+\bar{S}^3}$	0.4	$\frac{15}{1000+\bar{S}^3}$	0.4
β_2	-3.04	-0.15	2.72	$\frac{3}{1000+\bar{S}^3}$	-0.4	$\frac{3}{1000+\bar{S}^3}$	-0.2
β_3	4.16		-2.24	$\frac{-19}{1000+\bar{S}^3}$	1.04	$\frac{-19}{1000+\bar{S}^3}$	$2-\exp\{-(\bar{S}-\bar{\Omega})^2\}$
β_4					$-80C_\mu^2$	$-80C_\mu^2$	$-32C_\mu^2$
β_5					0	0	0
β_6					$-40C_\mu^2$	$-16C_\mu^2$	$-16C_\mu^2$
β_7					$40C_\mu^2$	$16C_\mu^2$	$16C_\mu^2$

$$\frac{-0.3\nu_t}{\varepsilon\left(S_{ij}-S_{kk}\frac{\delta_{ij}}{3}\right)} \tag{2.39}$$

$$C_\mu = \frac{0.3\left[1-\exp\left\{\left(-0.36\exp\left\{\left(0.75\max\left(\bar{S},\bar{\Omega}\right)\right)\right\}\right)\right\}\right]}{1+0.35\left(\max\left(\bar{S},\bar{\Omega}\right)\right)^{1.5}} \tag{2.40}$$

$$C_\mu = \min\left[\frac{1}{0.9\bar{S}^{1.4}+0.4\bar{\Omega}^1.4+3.5}, 0.15\right] \tag{2.41}$$

2.5.2 Non-linear $k-\omega$ turbulence models

Wallin and Johansson (2000) derived a non-linear variation of the $k-\omega$ model which closes the Reynolds stresses with the full expansion of the non-linear stress strain relationship (2.35) using constitutive relationships for the arising functions β. This model is commonly known as explicit algebraic Reynolds stress model (EARSM) where the Reynolds stresses are defined as in the Boussinesq approximation plus an additional anisotropy term

$$\begin{aligned} a_{ij}^{(3D)} =& \beta_3\left(\Omega_{ik}\Omega_{kj}-\frac{1}{3}II_\Omega\delta_{ij}\right)+\beta_4\left(S_{ik}\Omega_{kj}-\Omega_{ik}S_{kj}\right) \\ &+\beta_6\left(S_{ik}\Omega_{kl}\Omega_{lj}+\Omega_{ik}\Omega_{kl}S_{lj}-II_\Omega S_{ij}-\frac{2}{3}IV\delta_{ij}\right) \\ &+\beta_9\left(\Omega_{ik}S_{kl}^*\Omega_{lm}\Omega_{mj}-\Omega_{ik}\Omega_{kl}S_{lm}^*\Omega_{mj}\right), \end{aligned} \tag{2.47}$$

$$a_{ij}^{(2D)} = \beta_4^{(2D)}\left(S_{ik}\Omega_{kj}-\Omega_{ik}S_{kj}\right). \tag{2.48}$$

2.5.3 Non-linear Spalart-Allmaras turbulence model

The quadratic constitutive relation (QCR) expanding the SA turbulence model was derived by Spalart (2000) by expanding the Boussinesq approximation as

$$\tau_{ij,QCR} = \tau_{ij,\text{Boussinesq}} - C_{cr1}\left[O_{ik}\tau_{jk,\text{Boussinesq}} + O_{jk}\tau_{ik,\text{Boussinesq}}\right] \tag{2.49}$$

with

$$O_{ik} = \frac{2\Omega_{ik}}{\sqrt{\frac{\partial u_m}{\partial x_n}\frac{\partial u_m}{\partial x_n}}}. \tag{2.50}$$

2.6 Reynolds stress models

The Reynolds Stress Models (RSM) avoid the isotropic turbulence assumption by not making use of the Boussinesq approximation 1.2. Instead the RSM models solve the Reynolds stress equation

$$\frac{\partial \tau_{ij}}{\partial t} + \bar{u}_k\frac{\partial \tau_{ij}}{\partial x_k} = -\tau_{jk}\frac{\partial \bar{u}_i}{\partial x_k} - \tau_{ik}\frac{\partial \bar{u}_j}{\partial x_k} + \varepsilon_{ij} - \Pi_{ij} + \frac{\partial}{\partial x_k}\left[\nu\overline{\frac{\partial \tau_{ij}}{\partial x_k}} + C_{ijk}\right]. \tag{2.51}$$

This expression is derived in appendix A.3. The terms on the left-hand side represent the rate of change and transport by convection respectively. The first two terms on the right-hand side are the stress production terms, ε_{ij} is the dissipation, Π_{ij} is the pressure-strain interaction and C_{ijk} represents the molecular and turbulent diffusion. The additional terms ε_{ij}, Π_{ij} and C_{ijk} are expressed as

$$\varepsilon_{ij} = \overline{2\mu\frac{\partial u_j'}{\partial x_k}\frac{\partial u_i'}{\partial x_k}}, \tag{2.52}$$

$$\Pi_{ij} = \overline{p'\left[\frac{\partial u_i'}{\partial x_j} + \frac{\partial u_j'}{\partial x_i}\right]}, \tag{2.53}$$

and

$$C_{ijk} = \overline{p'u_i'}\delta_{jk} + \overline{p'u_j'}\delta_{ik} + \overline{u_i'u_j'u_k'}. \tag{2.54}$$

The Reynolds stress equation provides six equations, one for each τ_{ij} component due to symmetry. The production term Π_{ij} is commonly modeled with the gradient diffusion assumption and the dissipation with an additional transport equation. RSM models typically require solving seven transport equations, hence some authors call RSM models seven-equation turbulence models. However variations exist with more or less additional transport equations.

The biggest disadvantage of RSM models is their complexity. The user needs to be very skilled with tensor mathematics to comprehend different models. Furthermore, whilst they increase the realism, their stability is worse making the models unattractive for industrial applications.

2.7 Discussion

In this chapter the RANS momentum equation was derived from the incompressible NS equations. From this derivation an additional Reynolds stress tensor was found which needed to be modelled. Three approaches were presented; 1) linear eddy viscosity modelling based on the Boussinesq approximation 2) non-linear eddy viscosity modelling and 3) Reynolds stress modelling. In order to put all these models into perspective, Gatski and Jongen (2000) proposed figure 2.2. This figure shows the cost and complexity vs realism and dynamic range of a variety of turbulence models. One can see that the linear, non-linear and algebraic models are all considered viscosity models. This is due to the necessity to model the turbulent viscosity ν_t and stress-strain relationships (1.2) or (2.35). The RSM model on the other hand solves the differential Reynolds stress equation (2.51), eliminating this requirement. Within the viscosity models a distinction can be made between linear and non-linear stress-strain relationship based models. The linear ones assumes the flow to behave isotropically, $a_{xx} = a_{yy} = a_{zz} = 0$. The non-linear ones circumvent this by also considering flow rotation rates Ω_{ij}. There already exist several tested non-linear eddy viscosity models. However none have acquired a large degree of usage due to stability problems and limitations of universal applications due to calibration. Explicit algebraic stress models take the non-linear stress-strain relationship to the next level solving the arising coefficients using more exact algebraic functions as in Wallin and Johansson (2000). However these models also suffer from stability problems and are also dependent on calibration. Finally, the most exact model, but also most complex are the RSM models. In this framework, a global-coefficient non-linear eddy viscosity model is presented in chapter 3 which is calibrated on a square duct. By global-coefficient the coefficients β are considered to be a single scalar over the entire flow field. This model shall be situated on par with other non-linear stress-strain relationship models offering a similar realism for lower complexity and cost.

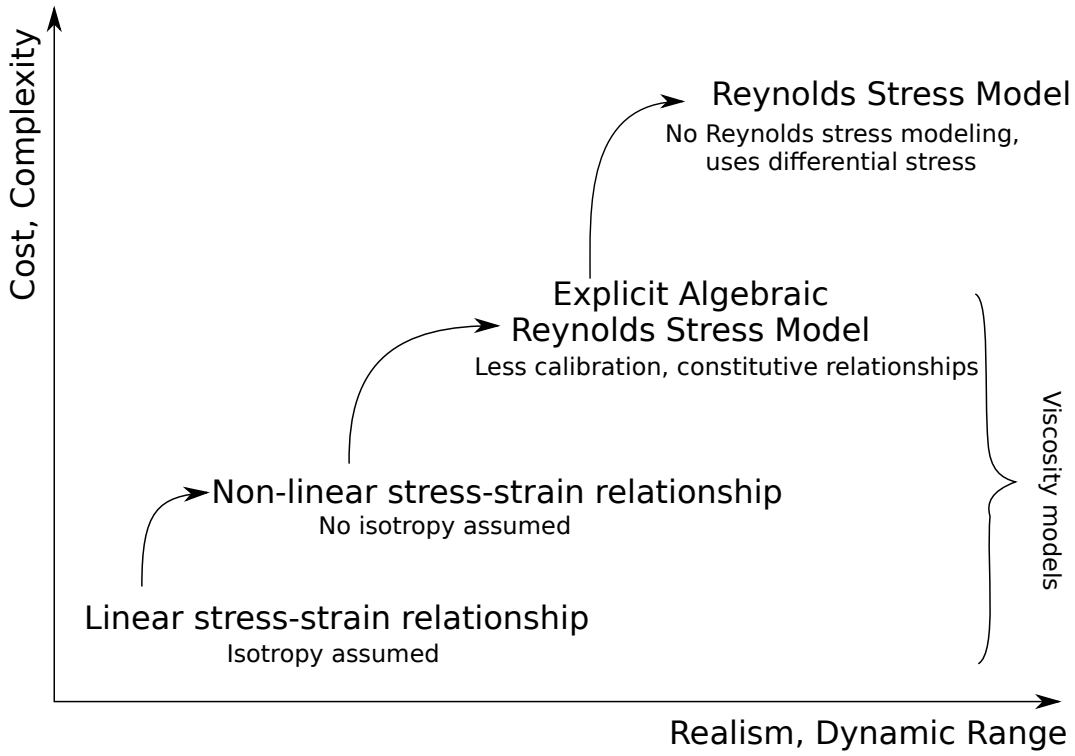

Figure 2.2: Hierarchy of RANS turbulence models.

Chapter 3

Proposed methodology

In this chapter the proposed methodology is discussed. First the newly proposed model is given in section 3.1. The training data is presented in section 3.3. Section 3.2 provides the minimization problems used for calibration and section 3.4 describes the optimization routines used. The last section presents the square-duct and wing-body junction test cases and convergence studies.

3.1 Proposed model

In section 2.5 some non-linear eddy viscosity models have been presented. The little agreement in coefficients shows the difficulty of deriving a universal non-linear eddy viscosity model. In this section a non-linear eddy viscosity model with global coefficients is presented. This means the coefficients β are assigned a single value for the entirety of the flow field. The proposed model is based on the $k-\omega$ model. The Boussinesq approximation (1.2) is expanded as described in Pope (1975) by the addition of 9 non-linear tensors (2.36) resulting in (2.35). The tensor $T_{ij} = S_{ij}$ corresponds to the Boussinesq approximation and is considered the 0^{th} and linear tensor. The functions β are treated as global coefficients to be calibrated. The remaining $k-\omega$ coefficients are left untouched.

A ramping factor ξ is constructed to increase solver stability. This factor is included by multiplying the non-linear stresses as

$$\tau_{ij} = \tau_{ij,\text{linear}} + \xi\tau_{ij,\text{non-linear}} \tag{3.1}$$

This factor is defined as a function of the number of iterations t_i with the first 100 iterations being $\xi = 0$ for the solver to stabilize. After 100 iterations ξ increases up to 1. Figure 3.1 shows the behavior of ξ vs the number of iterations. The mathematical expression for ξ is

given by

$$\xi = \begin{cases} 0, \text{ if } t_i < 100 \\ \left(1 + e^{10\left(1 - t_i/t_i^*\right)}\right)^{-1}, \text{ if } 100 < t < 2t^* \\ 1, \text{ if } t_i > 2t_i^*. \end{cases} \tag{3.2}$$

t_i^* is the only user defined input necessary to determine the iteration at which $\xi = 0.5$ is desired.

The turbulence model is implemented in OpenFOAM and used in combination with the simpleFoam solver. The implementation and verification is provided in appendix C.

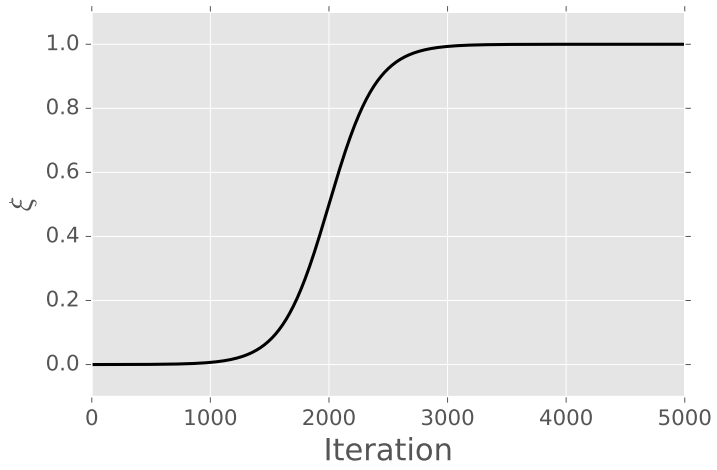

Figure 3.1: Relaxation factor ξ vs iterations (t_i) with a $t_i^* = 2000$

3.2 Minimization problems

This section outlines the minimization problems used throughout this project. These are defined as $\min_x L(x)$ with $L(x)$ being the loss function to be minimized by varying the input x. In this research the loss function is always defined as the L-2 norm of the difference between the exact f_{exact} and approximated $\bar{f}(x)$ result value as

$$L(x) = \left(f_{exact} - \bar{f}(x)\right)^2. \tag{3.3}$$

Since the quantity of interest f is a vector or tensor in this study, the loss function is summed over its components and each component weighted by the maximum over the flow field (over all cells) of the exact result. The loss function for a vector is then given by

$$L(x) = \sum_i \frac{\left(f_{exact,i} - \bar{f}_i(x)\right)^2}{\max\left(f_{exact,i}\right)} \tag{3.4}$$

and for a tensor by

$$L(x) = \sum_{ij} \frac{\left(f_{exact,ij} - \bar{f}_{ij}(x)\right)^2}{\max\left(f_{exact,ij}\right)}. \tag{3.5}$$

As is common in Computational Fluid Dynamics simulations graded meshes are used with varying cell sizes. In order to circumvent boundary layer cells to dominate the calibration procedure an area weighting is included in all loss functions by integrating every cell of the loss function over its cell area as

$$\int_{\Omega_a} L(x) d\Omega_a. \tag{3.6}$$

For the calibration two loss functions are evaluated. One to reduce the difference between exact and approximated Reynolds stresses and one to evaluate the difference between the exact and approximated velocities. The first loss function comes logically since the non-linear eddy viscosity is built to give a better prediction of τ_{ij}. However, as has been argued by Xiao et al. (2016) and also confirmed in this study, the mapping from Reynolds stresses to velocity field is not unique. By this is meant that when modifying the turbulence model (changing closure coefficients), the same Reynolds stresses can predict different or the same velocity fields and vice-versa. Therefore also the velocity differences are evaluated as loss function. The loss function in terms of Reynolds stresses is given by

$$L_\tau(\beta) = \sum_{ij} \int_{\Omega_a} \frac{\left(\tau_{exact,ij} - \bar{\tau}_{ij}\left(\beta\right)\right)^2}{\max(\tau_{exact,ij})} d\Omega_a \tag{3.7}$$

and that in terms of velocity by

$$L_U(\beta) = \sum_{i} \int_{\Omega_a} \frac{\left(u_{exact,i} - \bar{u}_i\left(\beta\right)\right)^2}{\max(u_{exact,i})} d\Omega_a. \tag{3.8}$$

The determination of $\bar{\tau}_{ij}$ can be achieved in two ways; 1) evaluating solely the Reynolds stresses without solving the RANS equations and 2) solving the RANS equations and evaluating the turbulence model at the same time. Option 1 is cheaper in terms of computation cost since only $\bar{\tau}_{ij}$ are unknowns whilst the velocity u_i, turbulent kinetic energy k and specific turbulence dissipation ω are prescribed from the training data. Then only the Reynolds stress tensor (2.35) needs to be solved. However due to the mapping not being unique, this does not guarantee an optimum solution of the flow field once solving the RANS equations. Therefore option 1 needs to be compared to option 2. Option 2 solves the RANS equations for each combination of coefficients β. This implies recomputing all quantities for each combination.

In order to evaluate the Reynolds stresses by not solving the RANS equations the specific turbulence dissipations is computed from the training data. This is done by solving the ω equation (2.30) from the $k-\omega$ turbulence model with coefficients as prescribed by Wilcox (1994a). The training data u_i and τ_{ij} is propagated into (2.30).

3.3 Training data

The training data was obtained from Direct Numerical Simulations (DNS) on a square-duct performed by (Pinelli et al., 2010). Simulations at bulk Reynolds numbers $Re_h = U_b h/\nu$ from 1100 to 3500 were performed to evaluate the Reynolds number dependence on the flow structure and turbulence. The flow was treated as incompressible with no volume forcing. The results were validated with experiments from Gavrilakis (1992) and Kawahara and Kamada (2000) at $Re_h = 2205$ and $Re_h = 3535$ respectively.

The data from Pinelli et al. (2010) contained the mean velocities and perturbation. From the perturbations the turbulent kinetic energy and Reynolds stresses are computed. The turbulent kinetic energy from

$$k = \frac{1}{2}\left(u'u' + v'v' + w'w'\right) \tag{3.9}$$

and the Reynolds stresses from

$$\tau_{ij} = \begin{bmatrix} u'u' & u'v' & u'w' \\ u'v' & v'v' & v'w' \\ u'w' & v'w' & w'w' \end{bmatrix}. \tag{3.10}$$

The specific turbulence dissipation is computed from (2.30) using the closure coefficients from Wilcox (1994a) and velocity field as an input from Pinelli et al. (2010).

In this research only the data for $Re_h = 1100$ is considered.

3.4 Optimization routines

The loss functions from section 3.2 are evaluated using standard optimization routines implemented in Python. The Nelder-Mead, L-BFGS-B, BFGS, powell, CG, TNC, COBYLA and SLSQP optimization routines implemented in Python were all evaluated. The Nelder-Mead and L-BFGS-B functions were deemed as the most suitable for this problem. Furthermore Monte-Carlo simulations were performed to increase computational speed by allowing parallelized random samples to be taken as evaluations of the loss functions to approximate the optimum.

3.4.1 Nelder-Mead

The Nelder-Mead method or downhill simplex method finds the maximum or minimum of a multi-dimensional loss function $L(x)$ without requiring its derivative. As initial condition $n+1$ points (n=dimension) are evaluated forming the initial simplex. In 2D this simplex has the form of a triangle as shown in figure 3.2. Based on the evaluations of $L(x)$ at each point the simplex is updated. The simplex update can be in the form of

- Reflection: moving the highest or lowest evaluation through the opposing face conserving the volume of the simplex
- Expansion: by moving one point further away and increasing the simplex volume to allow for larger search steps
- Shrinkage: moving one point closer to the others reducing the simplex volume and the search step

The simplex method is very sensitive to the initial condition in case of a non-convex optimization problem. Based on the initial condition a local optimum might be found instead of a global optimum. This is also showcased in figure 3.2 where the initial condition captured a gradient towards the local optimum in the left bottom corner and the Nelder-Mead function will optimize to that region.

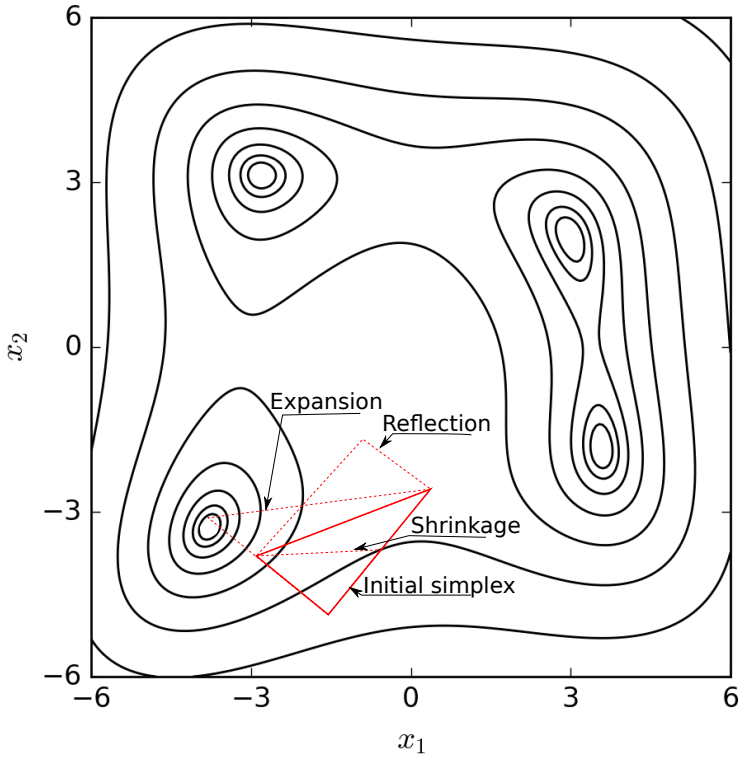

Figure 3.2: Nelder-Mead simplex for 2D minimization problem.

3.4.2 L-BFGS-B

The L-BFGS-B method is chosen due to its good ability of solving high dimensional problems. The dimension of this problem is between 1 and 9, one for each coefficient β to be optimized. The L-BFGS-B algorithm sets as goal to minimize a function $L(x)$ in a specific search direction

obtained from the gradient of the loss function. Starting at the initial condition x_0 the search direction p_k is found from

$$B_k p_k = -\nabla L(x_k). \tag{3.11}$$

with B_k being the approximate Hessian matrix and $\nabla L(x_k)$ an approximate of the gradient of the loss function. The gradient is not provided to the optimization routine but approximated within the routine itself. For the next iteration the Hessian matrix B is updated following the quasi-Newton condition as

$$B_{k+1}(\mathbf{x}_{k+1} - \mathbf{x}_k) = \nabla f(\mathbf{x}_{k+1}) - \nabla f(\mathbf{x}_k). \tag{3.12}$$

The optimization is summarized in 5 steps which are repeated until a specific convergence criteria is fulfilled:

1. Select the initial condition x_k and define initial search direction p_k.
2. Perform a 1-dimensional line search on $\alpha_k = \arg\min f(\mathbf{x}_k + \alpha \mathbf{p}_k)$.
3. Update $s_k = \frac{1}{y_k^T \alpha_k}$ and set $x_{k+1} = x_k + s_k$
4. Update $y_k = \nabla L\left(x_{k+1}\right) - \nabla L\left(x_k\right)$.
5. Determine the new Hessian matrix

$$B_{k+1} = B_k + \frac{y_k y_k^T}{y_k^T s_k} - \frac{B_k s_k s_k^T B_k}{s_k^T B_k s_k}. \tag{3.13}$$

In mathematical terms the Hessian matrix is a square matrix of second-order partial derivatives

$$B = \frac{\partial^2 f}{\partial x_i \partial x_j} \tag{3.14}$$

used to describe the local curvature of a function. With the curvature in the L-BFGS-B and other Newton and quasi-Newton optimization routines the search direction can be established.

3.4.3 Monte-Carlo

Monte-Carlo simulations are random evaluations of $L(x)$ on a defined search field. At every sample point x_k the loss function $L(x_k)$ is evaluated and the result stored. Combining all found results the optimum is approximated. Monte-Carlo methods can be considered as brute force optimization which find an approximate of the optimum. They require many evaluations more compared to other minimization routines. However they can be implemented in parallel. This means that if the computer resources are available a similar result can be obtained in less time. In this study the RANS equations were solved for random β and the results stored. This allowed for modifications of the loss function $L(x)$ after completing the Monte-Carlo simulation without having to redo the entire optimization routine. The sample size

considered is at least 200 samples between the margins of $-10 \leq \beta \leq 10$ for each degree of freedom.

The cluster available during this research limited the computation time on each core to 48 hours allowing a maximum of 96 iterations per optimization routine when solving the RANS equations. This was not sufficient for convergence. Using a Monte-Carlo method CFD runs could be performed on a random search space on all available cores and the results stored. This eliminates issues arising from the time limitation of 48 hours allowing to perform many more CFD runs and comparing the results once a large enough sample space was solved.

3.5 Test cases

In this section the numerical set-up for the calibration and prediction are discussed. For the calibration a square-duct was used. Predictions were made on a rectangular-duct and wing-body junction. All cases are built for OpenFOAM. All cases will showcase the domain set-up with initial and boundary conditions and a mesh convergence study. First the square-duct is discussed, followed by the rectangular-duct and wing-body junction.

3.5.1 Square-duct

The square-duct was used for the calibration. This geometry has been selected for two reasons: 1) the existence of secondary motions in the form of corner vortices and 2) the availability of DNS results.

A flow passing through a square duct experiences 8 corner vortices, 2 per quadrant, as depicted in figure 3.3. The corner vortices are a phenomenon not predicted by linear eddy viscosity models due to the Boussinesq approximation (1.2). Non-linear eddy viscosity models can represent this kind of fluid motion. Making the square-duct an ideal test case for calibrating and studying a global-coefficient NLEVM.

For this research a square-duct mesh of 2,500 cells is constructed after a mesh convergence study. The mesh is constructed with the blockMesh utility from OpenFOAM. Due to symmetry only one quarter of the duct is solved and cyclic boundary conditions are used to simulate an infinite length duct. No-slip boundary conditions are used on the walls. The solved quadrant is marked with grey in figure 3.4. The grid spacing is uneven with a 0.1 grading such that the cells close to the walls are smaller than those close to the symmetry lines. The bulk velocity is selected to be unity with the viscosity being adjusted to obtain the desired Reynolds number of $Re_h = 1100$.

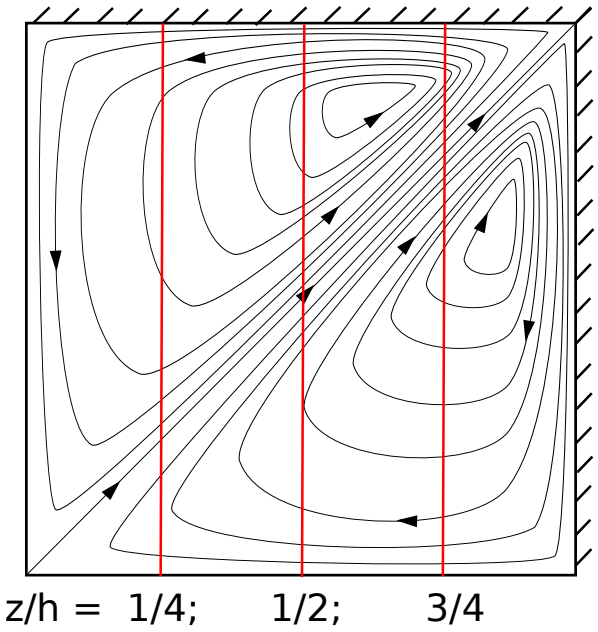

Figure 3.3: Contour plot of stream function of the right upper quadrant of a square duct flow and location of samples lines $z/h = 1/4$; $1/2$ and $3/4$ within the square duct.

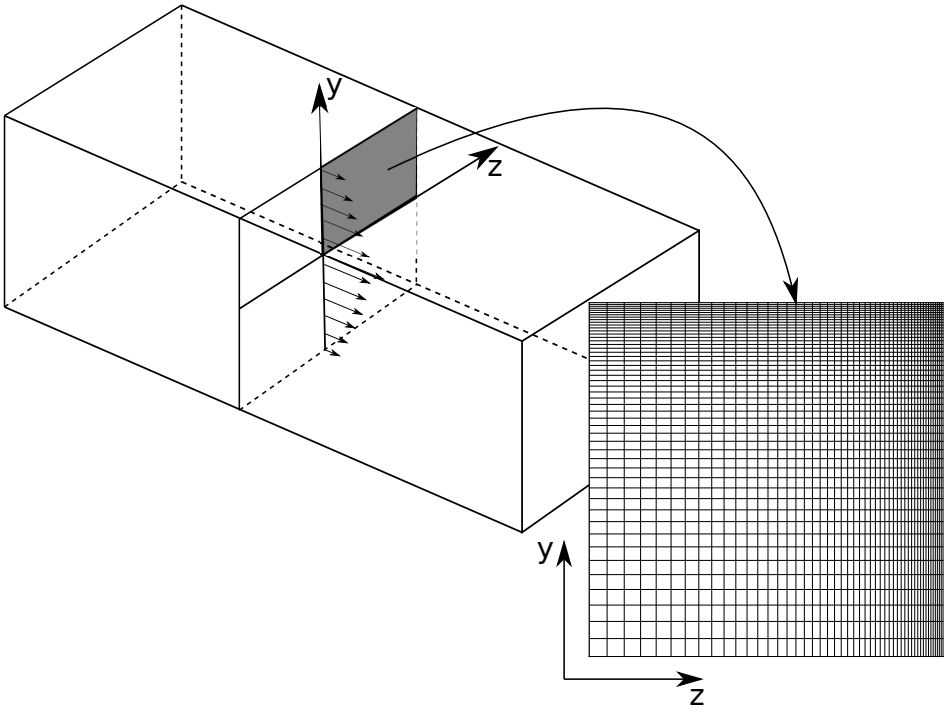

Figure 3.4: Designation of quadrant to be solved and mesh spacing.

Mesh convergence study

The mesh convergence study is performed by evaluating the friction coefficient on the side wall. Grids with increasing number of cells are evaluated from a very coarse 225 cell mesh to

a very fine 10,000 cell mesh. The friction coefficient for all meshes is plotted in figure 3.5. At increasing number of cells the friction coefficient converge to a similar line. Grids with 225 and 625 cells are considered too coarse whilst the differences between 5,625 and 10,000 cells is very small. A compromise of 2,500 cells is chosen for the calibration. This grid offers good accuracy at at least half the computational cost when compared to the finer meshes. The final grid is wall resolved with the first cell height being inside the viscous layer with $y^+ < 1$. In appendix E the near wall behavior of a fluid is discussed.

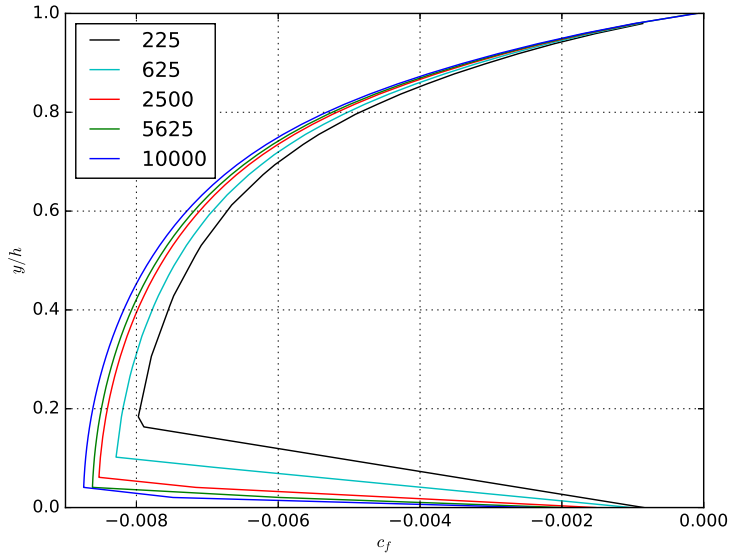

Figure 3.5: Mesh convergence based on friction coefficient c_f on side wall of square duct.

The residuals for the square duct are lowered to at least 1e-6 which is reached at approximately 25,000 iterations. The linear models fail to predict the secondary motions and pressure differences within the duct, meaning the residuals for these variables do not converge. The residuals for a linear and non-linear eddy viscosity are given in figure 3.6.

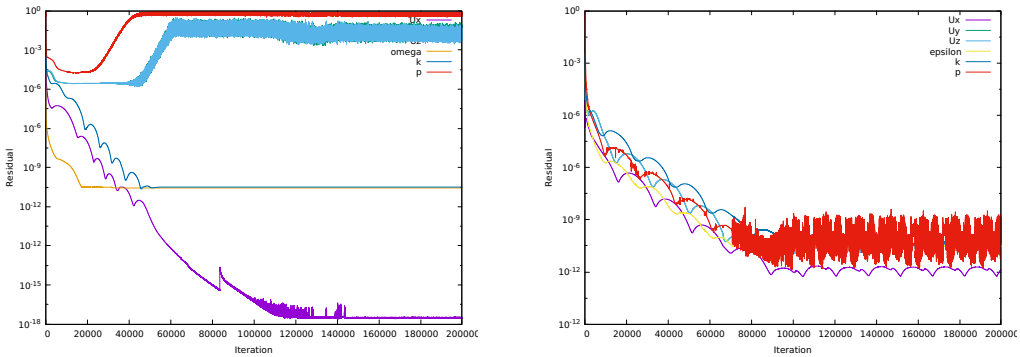

Figure 3.6: Residuals with a linear (left) and non-linear (right) eddy viscosity turbulence model.

3.5.2 Rectangular duct

The rectangular-duct is used for the first predictions. This is aimed at providing insight in predicting a similar flow. The mesh is set-up similarly to the square-duct. One of the two sides is doubled to $2h$. Similarly the number of cells for that side is doubled. Leaving the total number of cells of 5,000. The mesh is considered converged based on the mesh convergence study of the square duct. The bulk Reynolds number based on the smaller side is $Re_h = u_b h/\nu = 1100$. The convergence criteria was set to 1e-6.

3.5.3 Wing-body junction

The wing-body junction is a more complex 3D case on which linear eddy viscosity models are known to be inaccurate. Bordji et al. (2014) has shown that the Spalart and Allmaras (1992) (SA) turbulence model over predicts the corner separation whilst the SA model expanded with a Quadratic Constitutive Relationship (QCR) (Spalart, 2000) provides better predictions. This makes this test case ideal to evaluate the improvements possible by using a square-duct calibrated global-coefficient non-linear eddy viscosity model.

The wing body junction is set up similar to the experiment carried out by Devenport and Simpson (1990). A 3:2 elliptical nose is joined with a NACA0020 tail at the thickest point. The wing is mounted to a flat plate with a boundary layer thickness of $\delta_{99} = 36$ mm 2.15 thicknesses in front of the wing. The momentum thickness Reynolds number is $Re = 6,700$ and the free-stream Reynolds number $Re = 132,560$. Due to symmetry only half the domain is solved. The coordinate system is x in the free stream direction, y normal to the wing centre-line and z along the wing-span. A schematic depicting this construction is given in figure 3.7. The plate and wing are treated as no-slip walls with wall functions.

The numerical set-up was generated with a plate length in front of the wing of 2.158 m. This length was computed based on the theoretical boundary layer thickness of a flat plate, given by

$$\delta \approx 0.37x/Re_x^{1/5}. \tag{3.15}$$

The domain is extended in the x, y and z direction by 8.8, 3.75 and 8 chord lengths respectively.

The mesh is generated in Pointwise with a grading of 1e-4 towards the plate and wing. This resulted in a $y^+ < 1$ close to the junction and $y^+ < 80$ on the coarsest cell with an average $y^+ < 25$. This is considered sufficient with the use of wall functions where a $y^+ < 30$ is recommended as explained in appendix E. For stability all simulations are started from a converged laminar solution. From a mesh convergence study 725,200 (149x50x101) cells were found sufficient for converged results. The grid set-up is shown in figure 3.8. This figure does not correspond to 725,200 cells, but the coarse mesh of 240,100 cells.

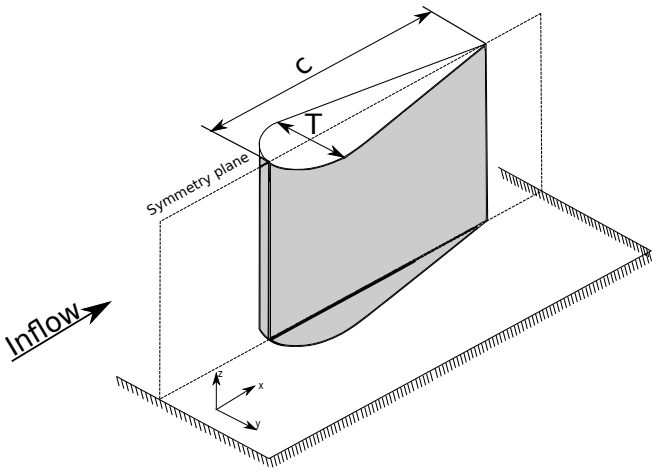

Figure 3.7: Wing-body junction set-up with $c/T = 4.254$.

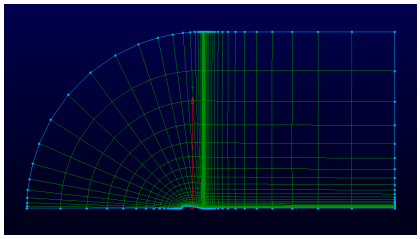

Figure 3.8: Wing-body junction grid in the x-y plane.

Mesh convergence study

The mesh convergence of the fuselage wing junction is evaluated in terms of the flat plate boundary layer growth and based on the corner flow separation. Dandois (2014) found the corner flow separation to be very sensitive towards grid refinement. Three different refinements are evaluated with 725,200, 1,960,200 and 5,900,400 cells. Based on the flat plate boundary layer, figure 3.9, the coarse and fine mesh follow the theoretical growth. The medium mesh appears to exhibit a larger, unphysical boundary layer growth. The reason for this could not be determined. The mesh is set-up in exactly the same form as the other meshes with the difference being the number of cells and refinement. In general problems of solver instabilities were observed for all meshes requiring a start from a laminar solution. Eventually the laminar solution was not converged. This mesh was discarded from further analysis. For the two remaining grids the corner separation region is plotted in figure 3.10. Both refinements predict corner vortices. The size of the vortices appear similar in both refinements with the only difference being the flow parallel to the wing at the trailing edge. The coarse mesh predicted parallel flow till closer to the plate than the fine mesh. For the purposes of this study the coarse mesh is considered sufficiently refined for the comparison of turbulence models. Residuals are always lowered to at least 1e-6. For a linear $k-\omega$ model figure 3.11 shows the iterations necessary to reach convergence. For the coarse case a good convergence is reached after 4,000 iterations starting at a laminar converged result.

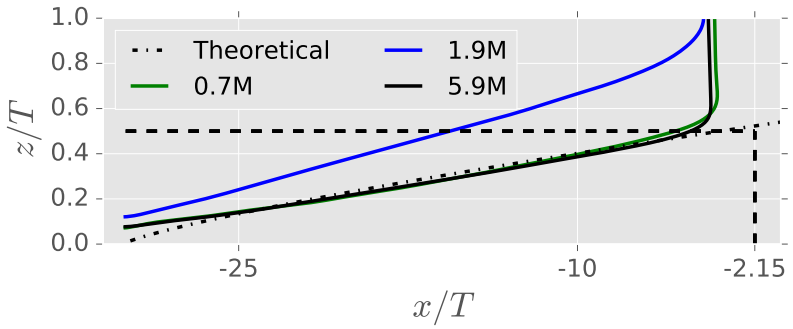

Figure 3.9: $0.99u_x$ (free-stream velocity) contour to represent boundary layer thickness on flat plate in front of wing with different number of mesh cells. Dotted line (- -) represents measured flat plate (without wing) boundary layer thickness by Devenport and Simpson (1990).

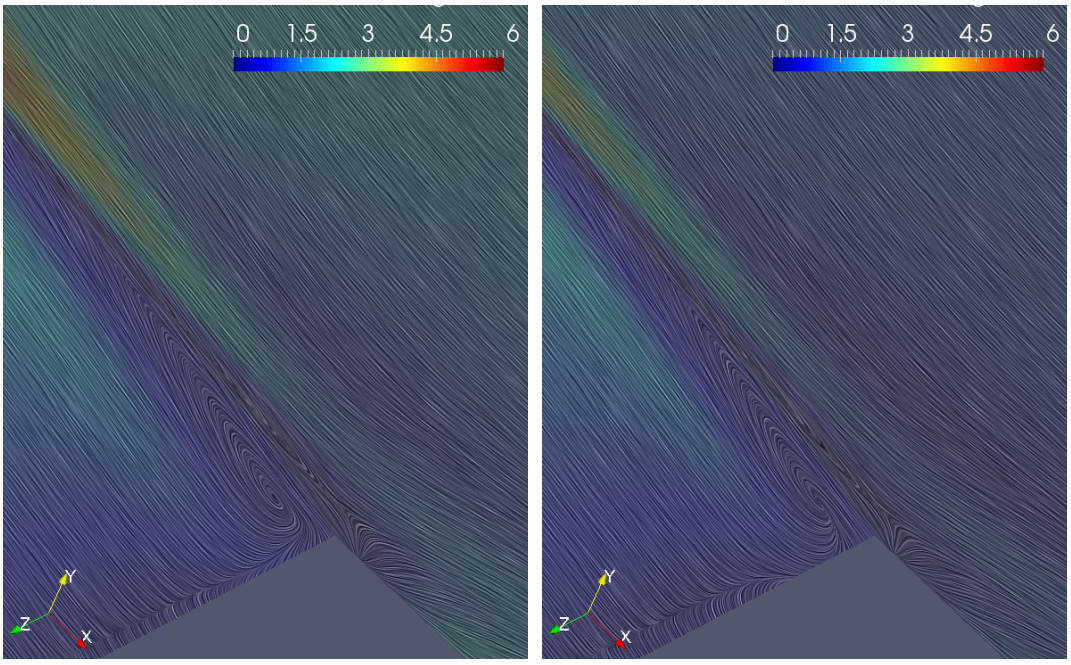

(a) 725,200 **(b)** 5,900,400

Figure 3.10: Wall shear stress stream-lines and color plot for different grids. Subcaption is the number of cells.

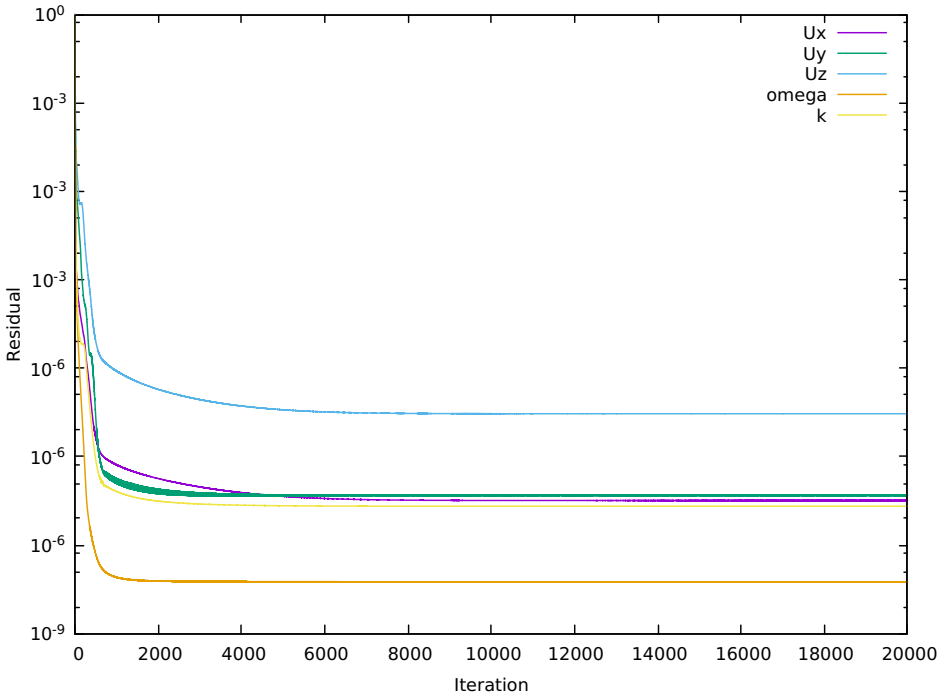

Figure 3.11: Residuals wing-body junction with linear $k-\omega$ model.

Chapter 4

Data-driven calibration

The calibration procedure was split in two approaches: 1) data-driven calibration explored in this chapter and solver-incorporated calibration explored in chapter 5.

This chapter describes the data-driven calibration. In this approach the DNS velocity field, turbulent kinetic energy and specific turbulence dissipation rate are used as inputs to evaluate the non-linear stress-strain relationship (2.35). The coefficients β are found from minimizing the differences between the exact $\tau_{exact,ij}$ and predicted $\bar{\tau}_{ij}$ Reynolds stresses with the loss function (3.7)

$$L_\tau(\beta) = \sum_{ij} \int_{\Omega_a} \frac{\left(\tau_{exact,ij} - \bar{\tau}_{ij}\left(\beta\right)\right)^2}{\max(\tau_{exact,ij})} d\Omega_a. \tag{3.7}$$

The remainder of this section is organized as follows: a sensitivity analysis in terms of Sobol indices is presented in subsection 4.1. Different optimization routines are studied in section 4.2. Section 4.3 analyses the tensors and identifies similarities between them. Section 4.4 explores the anisotropy and Reynolds stress to velocity relation. Using the calibrated coefficients β in the RANS solver is discussed in section 4.5. Finally a discussion concluding the data-driven calibration is made in section 4.6.

4.1 Sobol sensitivity analysis

In this subsection the sensitivity analysis for (3.7) is presented. The influence of the coefficients β towards minimizing (3.7) is evaluated using Sobol indices (Sobol, 2001). These can be of first order $S1$, second order $S2$ and total ST. The first order Sobol indices indicate the influence of each coefficient towards the total variance as a stand alone. The second

order Sobol indices indicate the influence of a coefficient when interacting with another coefficient. The total Sobol indices are the sum of all Sobol indices, including first, second and higher order indices, which indicate further interactions between coefficients. The sum of $\sum(S1 + S2 + \text{higher order interactions}) \leq 1$ whilst $\sum ST \geq 1$ because ST sums interaction terms multiple times. In example $S2_{12} = S2_{21}$ is the same effect, which in ST is considered twice as $S2_{1,2} + S2_{2,1}$. Hence $\sum S1 = 1$ and $\sum ST = 1$ iff[1] no interactions take place. The samples to be evaluated were obtained from Saltelli sampling with bounds of -10 and 10 for all coefficients (Saltelli, 2002; Saltelli et al., 2010). Saltelli sampling is a form of Monte-Carlo sampling that allows for variance-based sensitivity analysis with the SALib library in Python. This library is known to have some numerical inaccuracies where negative Sobol indices are possible. If negative Sobol indices occur the sample size needs to be increased or the 95% confidence interval needs to include 0. Then the negative Sobol indices can all be rounded up to 0.

The first coefficient β_1 is found to be the most influential towards the total variance, having the largest first order Sobol index $S1$ as show in figure 4.1. Its total Sobol index ST is also the largest, indicating it has the greatest influence when interacting with other coefficients. The second and third coefficients have small first order Sobol indices, but large total Sobol indices. From figure 4.2 it is seen that these two coefficients interact as shown by a large $S2_{2,3}$. Coefficients 6 to 8 show interactions with the first coefficient and amongst themselves. However these coefficients are of much less importance than the first 3. The remaining coefficients, 4, 5 and 9 have little to no influence towards the total variance as shown by all Sobol indices $S1$, $S2$ and ST approximately 0.

From the sensitivity analysis it is concluded that non-linear models with only the first three tensors should suffice to represent secondary motions, whilst higher order tensors likely only lead to over-fitting and have little to no impact on the predictions.

[1] If and only if

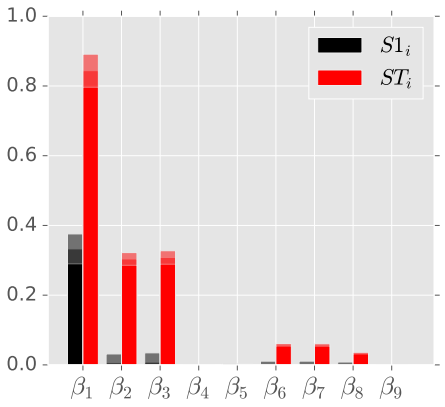

Figure 4.1: Sobol indices $S1$ (black) and ST (red).

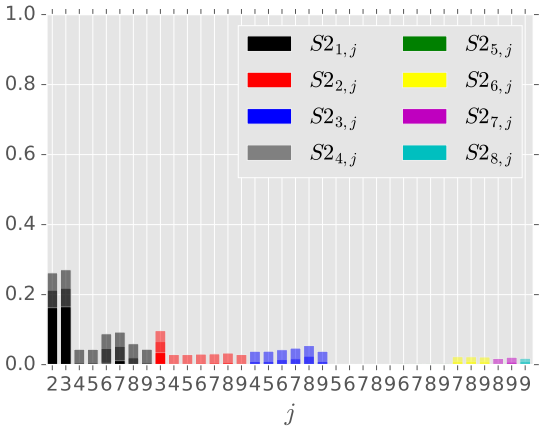

Figure 4.2: Sobol indices $S2_{i,j}$ indicating interactions between coefficients i and j. $S2_{i,j} = S2_{j,i}$

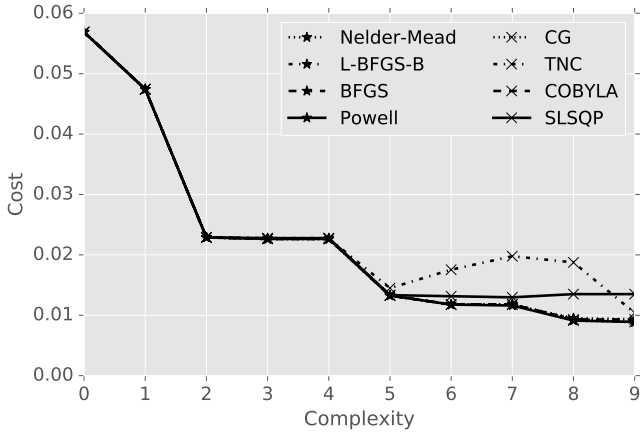

Figure 4.3: Cost vs complexity plot for data-driven calibration. Cost is expressed as the loss function value L_τ from (3.7). Complexity is expressed as the number of non-linear tensors considered, meaning coefficients $\beta \neq 0$ from (2.36) in (2.35).

4.2 Optimization

In this subsection different optimization routines are evaluated on the minimization of the loss function L_τ given in expression (3.7).

The optimization routines are divided into two groups, gradient based, and non-gradient based. The gradient based routines are preferred for convergence speed. However for high dimensional non-linear problems their derivative may not be known or difficult to obtain and the algorithm may fail. Therefore also a non-gradient based approaches are considered. A total of 8 optimization routines implemented in Python's Scipy package are considered: 1. gradient based; BFGS, L-BFGS-B, CG, TNC and SLSQP. 2. non-gradient based: Nelder-

Mead, Powell and COBYLA.

1. Within the gradient based methods several approaches exist. The conjugate gradient (CG) method is a modified steepest descent method that evaluates the gradient of the search vector in terms of the residual. This method is very popular for solving large sparse systems of positive definite matrices. Other gradient based methods require the Hessian matrix. Newton based methods such as the Truncated Newton algorithm or Newton Conjugate Gradient (TNC) and the Sequential least squares quadratic programming (SLSQP) routines. These compute the exact Hessian to obtain the Taylor series expansion and search direction. Determining the Hessian can be expensive or impossible, resulting in some optimization routines to approximate the Hessian matrix. These methods are known as quasi-Newton methods. The Broyden-Fletcher-Goldfarb-Shanno (BFGS) and Limited memory Broyden-Fletcher-Goldfarb-Shanno (L-BFGS-B) algorithms are quasi-Newton methods. Once the Hessian is approximated, the BFGS method stores the entire $n \times n$ Hessian matrix with the L-BFGS-B algorithm only storing a few vectors that represent the approximation. This makes the L-BFGS-B algorithm well suited for high dimensional problems.

2. Non-gradient based optimization methods determine repeated local minima expanding their search direction in the direction of the minima. Nelder-Mead makes use of a simplex of size $n + 1$ whose corners are updated as new evaluations are made. Powell's method establishes two search directions and updates these every iteration. The Constrained optimization by linear approximation (COBYLA) method is a version of Powell's method which allows specification of bounds.

In section 3.4 the L-BFGS-B and Nelder-Mead methods are explained in more detail.

The cost-complexity plot arising from the different optimization routines evaluating L_τ (3.7) is shown in figure 4.3. Cost is evaluated by the loss function L_τ (3.7) and complexity as the number of non-linear tensors (2.36) included in (2.35). Being a complexity of 0 equivalent to the Boussinesq approximation.

When including only the first non-linear tensor $T_{ij}^{(1)}$ from (2.36) a cost reduction of 17% is achieved. Considering the first 2 tensors a cost reduction of 60% is seen. Including tensors 5 to 9 a reduction of $\approx 77\%$ is attained. This is partially in accordance with the sensitivity analysis. From the Sobol indices it was found that the first three coefficients were the most influential with the remaining coefficients having little influence. Tensor 3 shows no influence in figure 4.3. This can be explained from its relation to the second tensor. Making the use of both redundant. Surprisingly the fifth tensor has a large impact, reducing the cost by an additional 17%. This also contradicts other non-linear models from table 2.1 which always calibrated this tensor with a zero coefficient as shown in table 2.1.

It is found that different optimization routines, though obtaining the same cost reduction at same number of coefficients, differ in their value for the coefficients. This is shown in table 4.1 for the Nelder-Mead and L-BFGS-B routines. These two optimization routines coincide almost perfectly in figure 4.3 whilst having differing coefficients, specially when considering

all 9 non-linear tensors. In accordance with the sensitivity analysis relations can be found between the coefficients. For all combinations of tensors $\beta_1 + \beta_2 - \beta_3 \approx 9$ and $\beta_2 - \beta_3 \approx 6$ are found. $\beta_6 + \beta_7 \approx 7$ is found when considering 7 tensors and $\beta_6 + \beta_7 + \beta_8 \approx -4$ when considering 8 tensors. No relation can be found for the 9^{th} coefficient.

Table 4.1: Coefficients for lowest cost at each complexity level. Loss function value L_τ is expressed as $L_\tau/10000$.

Nelder-Mead

$L_{\tau,1}$	$L_{\tau,2}$	L_U	β_1	β_2	β_3	β_4	β_5	β_6	β_7	β_8	β_9
569	345	142									
474	323	119	1.05								
229	248	137	3.47	6.48							
226	248	137	3.48	-5.86	-12.36						
226	248	137	3.48	-5.86	-12.36	0.34					
133	210	130	3.46	8.13	1.46	5.42	-5.75				
118	195	099	4.67	7.27	0.88	0.04	-5.82	-7.37			
117	195	097	4.72	3.49	-2.85	-2.50	-5.79	-16.70	9.12		
095	157	111	6.40	-1.02	-12.06	1.85	-5.65	-1.53	-10.37	7.84	
093	155	113	6.45	5.70	-5.56	3.32	-5.74	-3.83	-8.20	8.15	-1.10

L-BFGS-B

$L_{\tau,1}$	$L_{\tau,2}$	L_U	β_1	β_2	β_3	β_4	β_5	β_6	β_7	β_8	β_9
569	345	142									
474	323	119	1.05								
229	248	137	3.47	6.48							
228	248	137	3.48	3.23	-3.27						
228	248	137	3.48	3.23	-3.27	-0.03					
133	211	128	3.49	3.27	-3.30	0.01	-5.67				
118	195	098	4.67	3.29	-3.10	0.29	-5.79	-7.35			
118	195	098	4.66	3.24	-3.15	0.13	-5.79	-3.67	-3.62		
094	155	111	6.48	5.74	-5.41	0.38	-5.72	-6.14	-6.01	8.04	
089	151	101	6.95	-1.03	-12.25	1.42	-5.62	-104.53	88.64	8.10	-149.10

4.3 Tensor similarity analysis

In this subsection the tensor similarity will be analyzed to understand the coefficient sensitivity presented in subsection 4.1 and the cost-complexity relation from subsection 4.2. In order to show correlations between coefficients the cosine similarity between two tensors, defined by Weatheritt and Sandberg (2016) as tensor alignment

$$\rho_{(l,r)} = \frac{T^{(l)}_{ij} T^{(r)}_{ij}}{T^{(l)}_{mn} T^{(l)}_{nm} T^{(r)}_{pq} T^{(r)}_{qp}} \tag{4.1}$$

is used. This expression can be understood similar to the vector alignment

$$\frac{\mathbf{ab}}{\|\mathbf{a}\|\|\mathbf{b}\|}. \tag{4.2}$$

The tensor alignment is only a valid measure when the tensors are symmetric. Then the tensor alignment represents the alignment of the eigenvectors of the tensor. The measure $\rho_{(l,r)}$ expresses parallelity between two tensors with $\rho_{(l,r)} = \pm 1$, with 1 indicating same orientation and -1 indicating opposite orientation. $\rho_{(l,r)} = 0$ indicates orthogonal tensors. It has to be noted that the alignment is the combination of the three eigenvectors . This means that if two eigenvectors align, but not the third no alignment might be found by (4.1). In example, it is unknown what the tensor alignment says of two tensors if the 3 eigenvectors are parallel with equal orientation, parallel with opposing orientation and orthogonal respectively. This renders this metric delicate to interpretation and not to be considered as universal truth.

In order to increase anisotropy it is desired to have additional non-linear tensors to be orthogonal to the Boussinesq approximation term $T_{ij}^{(0)}$ and between each other. Table 4.2 provides an overview of the alignment between tensors. For clarity first focus on the tensor alignments with $T_{ij}^{(0)}$, the Boussinesq term, is put, followed by a discussion of the interactions between the non-linear tensors.

Table 4.2: Tensor alignment as expressed by (4.1). When alignment is not uniform reference to figure displaying alignment is given.

$T_{ij}^{(1)}$	0								
$T_{ij}^{(2)}$	4.4a	0							
$T_{ij}^{(3)}$	4.4b	0	4.4h						
$T_{ij}^{(4)}$	0	4.4e	0	0					
$T_{ij}^{(5)}$	-1	0	4.4i	4.4k	4.4m				
$T_{ij}^{(6)}$	0	1	4.4j	0	4.4n	0			
$T_{ij}^{(7)}$	0	1	0	4.4l	4.4o	0	4.4s		
$T_{ij}^{(8)}$	4.4c	4.4f	-1	1	0	4.4q	4.4t	4.4v	
$T_{ij}^{(9)}$	4.4d	4.4g	1	0	4.4p	4.4r	4.4u	4.4w	0
	$T_{ij}^{(0)}$	$T_{ij}^{(1)}$	$T_{ij}^{(2)}$	$T_{ij}^{(3)}$	$T_{ij}^{(4)}$	$T_{ij}^{(5)}$	$T_{ij}^{(6)}$	$T_{ij}^{(7)}$	$T_{ij}^{(8)}$

4.3.1 Alignment with the Boussinesq term

Tensors 1, 4, 6 and 7 are found to be orthogonal to the Boussinesq term. Tensor 5 is found to be parallel with opposing orientation. Tensors 2, 3 and 8 are found to be mostly orthogonal with parallelity increasing towards the centre of the square duct (bottom left corner in the figures). From this it is interpreted that all non-linear tensors but $T_{ij}^{(5)}$ provide new information towards the Reynolds stresses that could explain an improvement in anisotropy correction and thereby cost reduction in 4.3. If $T_{ij}^{(5)} \parallel T_{ij}^{(0)}$ that could also explain why in other NLEVM's its coefficient β_5 is always set to 0.

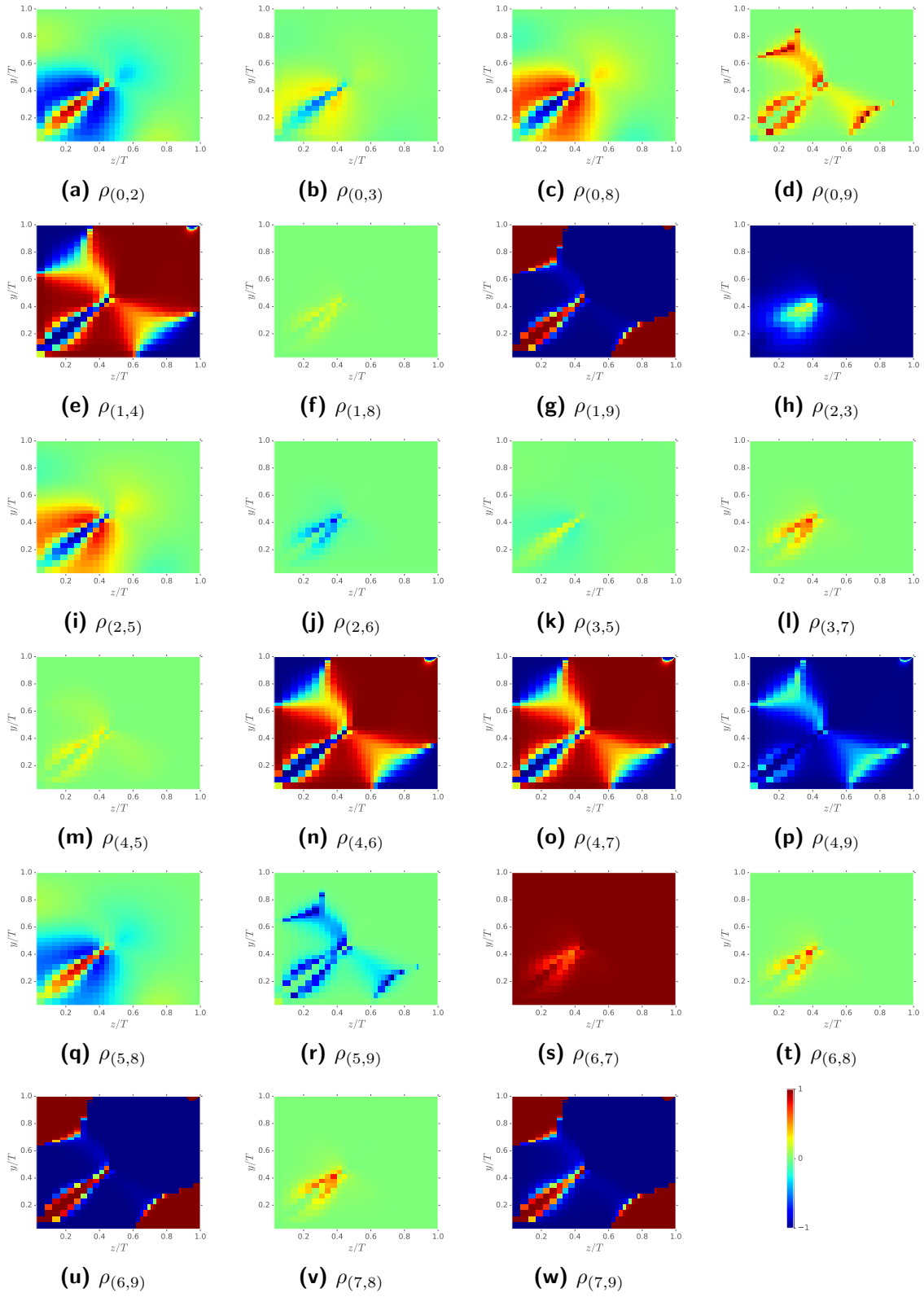

(a) $\rho_{(0,2)}$ **(b)** $\rho_{(0,3)}$ **(c)** $\rho_{(0,8)}$ **(d)** $\rho_{(0,9)}$

(e) $\rho_{(1,4)}$ **(f)** $\rho_{(1,8)}$ **(g)** $\rho_{(1,9)}$ **(h)** $\rho_{(2,3)}$

(i) $\rho_{(2,5)}$ **(j)** $\rho_{(2,6)}$ **(k)** $\rho_{(3,5)}$ **(l)** $\rho_{(3,7)}$

(m) $\rho_{(4,5)}$ **(n)** $\rho_{(4,6)}$ **(o)** $\rho_{(4,7)}$ **(p)** $\rho_{(4,9)}$

(q) $\rho_{(5,8)}$ **(r)** $\rho_{(5,9)}$ **(s)** $\rho_{(6,7)}$ **(t)** $\rho_{(6,8)}$

(u) $\rho_{(6,9)}$ **(v)** $\rho_{(7,8)}$ **(w)** $\rho_{(7,9)}$

Figure 4.4: Tensor alignment plots completing table 4.2.

4.3.2 Alignment between non-linear tensors

Focusing on the interactions between the non-linear tensors, connections between the alignment and Sobol indices are drawn. The second order Sobol indices suggested interactions between the first three tensors. From the alignment measure $\rho_{(1,2)} = 0$ and $\rho_{(1,3)} = 0$ were found, suggesting they act independently when it comes to correcting the anisotropy of the Reynolds stresses. This is in accordance with figure 4.3 where the addition of the first and second tensor have the strongest influence in terms of cost L_τ. $\rho_{(2,3)}$ given by figure 4.4h on the other hand provides an alignment of mostly -1 with a small region of more orthogonality. This is evidence that the tensors are related. This also explains the little influence of adding $T_{ij}^{(3)}$ in figure 4.3 since $T_{ij}^{(2)}$ already carries the same information.

The first non-linear tensor was found in table 4.2 to be aligned with $T_{ij}^{(6)}$ and $T_{ij}^{(7)}$, who are also aligned with each other. This means that these two tensors do not add new information towards the Reynolds stresses which also explains their little influence in terms of cost in figure 4.3.

The information captured by the 2^{nd} tensor appears to be similar to that of the 8^{th} and 9^{th} tensor given their alignments of $\rho_{(2,8)} = -1$ and $\rho_{(2,9)} = 1$. Also the third tensor is related to the 8^{th} tensor by $\rho_{(3,8)} = 1$. This is evidence that the higher order tensors add little information not captured by lower order tensors. Explaining why the cost is not further reduced in figure 4.3 by adding these terms.

Tensors $T_{ij}^{(4)}$ and $T_{ij}^{(5)}$ display some orthogonality towards lower order tensors. From this it can be said that these tensors should still have influence towards improving the Reynolds stress prediction. This is in direct contradiction of the Sobol indices analysis where $S1_4$ and $S1_5$ are found to be approximately 0. From the coefficients found in table 4.1 the fourth tensor is often preceeded by $\beta_4 \approx 0$ and its addition leads to no reduction in cost. This implies the fourth tensor carries undesired information. This is in line with the patterns observed in figure 4.4. The alignments $\rho_{(4,j)}$ display a unique pattern when compared to the others. The 5^{th} tensor on the other hand provides a reduction of cost in figure 4.3 and its preceeding coefficient is $\beta_5 \approx -5.7$ for all cases. This is attributed to the alignment with the Boussinesq term $\rho_{(0,5)} = -1$ which is not varied in this calibration. Then the 5^{th} tensor corrects for calibration errors arising from the eddy viscosity that multiplies the Boussinesq term.

4.3.3 Alignment discussion

Having analyzed the tensor alignment, it is concluded that the tensors 1 and 2 should provide the greatest improvement in Reynolds stresses. The 5^{th} tensor provides limited improvement which corrects for over or under-predictions caused by the Boussinesq term. The 4^{th} tensor is always preceded by $\beta_4 = 0$ and tensors 3 and 6 to 9 are related to lower non-linear tensors. Their addition can lead to over-fitting and also reduce solver robustness.

4.4 Results

In this section the calibrated global-coefficient non-linear eddy viscosity model prediction results on the square-duct are presented. The corection of anisotropy and relation of Reynolds stresses to secondary motions is detailed in sections 4.4.1 and 4.4.2 respectively. It was introduced in the Introduction that the secondary motions depend on the Reynolds stresses. The Boussinesq approximation was incapable of predicting secondary motions due to the isotropic flow assumption $\tau_{xx} = \tau_{yy} = \tau_{zz}$ which can not predict anisotropy. A non-linear eddy viscosity is not bound by this assumption and can therefore represent secondary motions. First the obtained anisotropy from the global-coefficient NLEVM is compared to the DNS data followed by the secondary motion analysis.

4.4.1 Anisotropy

The anisotropy can best be presented with Banerjee's Barycentric map (Banerjee et al., 2007). The construction of a Barycentric map is explained in appendix D. The barycentric map analyzes the eigenvalues of the anisotropy tensor

$$a_{ij} = \frac{\tau_{ij}}{2k} - \frac{1}{3}\delta_{ij} \tag{1.3}$$

which are physically bound by realizability constraints as explained in Schumann (1977) and introduced here in appendix D. One has to note that the model described by (2.35) is not bound by the realizability constraints and results can therefore be found outside of the barycentric map.

On the sample lines $z/h = 1/4$; $1/2$ and $3/4$ shown in figure 3.3 the anisotropy is evaluated for all complexities, 0 to 9. In figure 4.5 the anisotropy for complexities 1, 2, and 5 are given. Complexities higher than 5 exhibit similar anisotropies as a complexity of 5 and complexities 3 and 4 showed a similar result as complexity 2. Almost no differences between the results found from the optimization routines L-BFGS-B and Nelder-Mead can be found. This implies that different turbulence models (different coefficients β) with same velocity field can predict the same Reynolds stresses.

In figure 4.5 it can be seen that only including the first non-linear tensor from (2.36) only corrects the anisotropy slightly being concentrated around the plane strain. Increasing the complexity the anisotropy can be corrected further by shifting it towards the 1-component turbulence (bottom right corner of the triangle). There is always a prediction of plane strain close to $y/h \approx 0$. The data points outside of the barycentric triangle in figure 4.5 display the failure of the global-coefficient NLEVM to satisfy the realizability constraint.

Anisotropy can be corrected with the NLEVM, the next step is to relate the anisotropy corrections to the secondary motions.

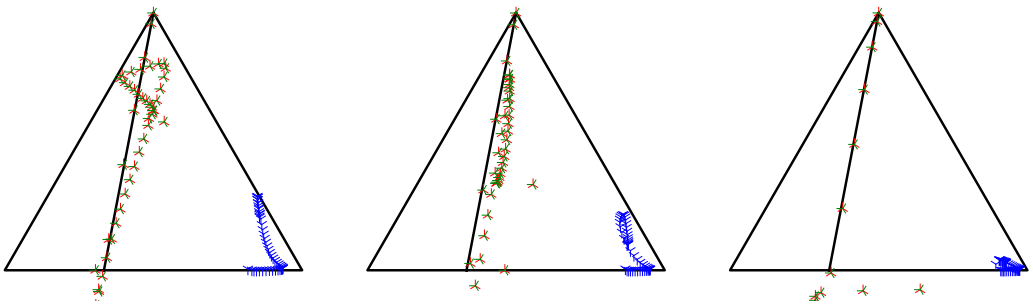

(a) Complexity of 1; $\beta_1 \neq 0$ and $\beta 2, ..., 9 = 0$

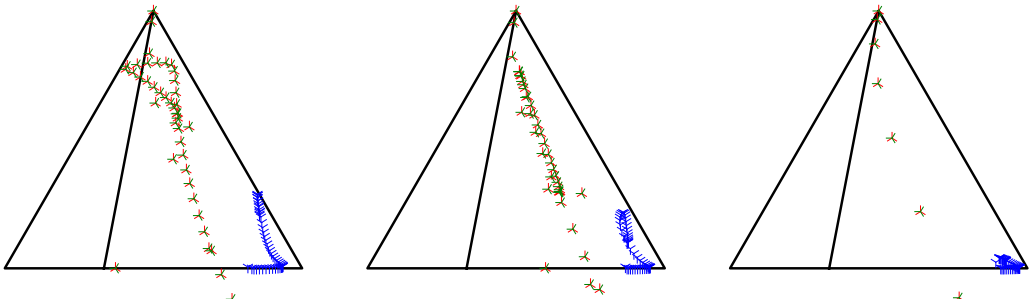

(b) Complexity of 2; $\beta_{1,2} \neq 0$ and $\beta 3, ..., 9 = 0$

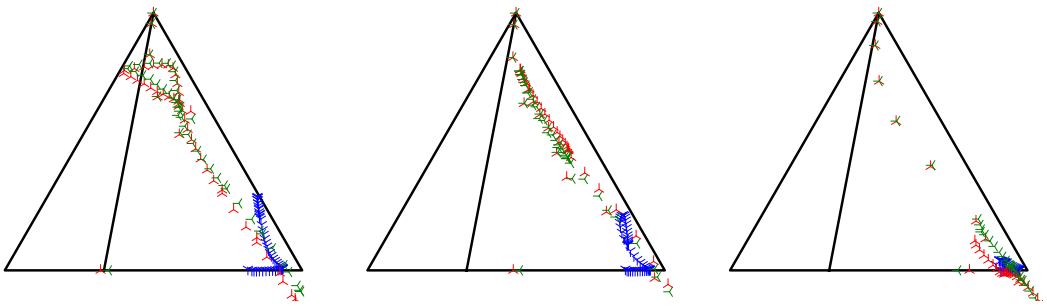

(c) Complexity of 5; $\beta_{1,...,5} \neq 0$ and $\beta 6, ..., 9 = 0$

DNS L-BFGS-B Nelder-Mead

Figure 4.5: Anisotropy on samples lines $z/h = 1/4$ (left); $1/2$ (centre); $3/4$ (right). Anisotropy moves from 1-component (bottom right corner) towards plane strain at increasing y/h. Data points outside of the triangle correspond to anisotropies that do not satisfy the realizability constraint.

4.4.2 Reynolds stress to secondary motion analysis

Having found that the anisotropy can be corrected it needs to be related to the secondary motions. This is done by analyzing the Reynolds stress components responsible for the secondary motions, $(\tau_{yy} - \tau_{zz})$ and τ_{yz} as described in the Introduction from equation (1.5).

$$\left(\frac{\partial^2}{\partial z^2}-\frac{\partial^2}{\partial y^2}\right)\tau_{yz}+\frac{\partial}{\partial y}\frac{\partial}{\partial z}\left(\tau_{yy}-\tau_{zz}\right)= \\ \left(\frac{\partial^2}{\partial y^2}-\frac{\partial^2}{\partial z^2}\right)\left(\nu_t\left(\frac{\partial u_y}{\partial z}+\frac{\partial u_z}{\partial y}\right)\right)+2\frac{\partial}{\partial y}\frac{\partial}{\partial z}\left(\nu_t\left(\frac{\partial u_z}{\partial z}-\frac{\partial u_y}{\partial y}\right)\right) \tag{1.5}$$

Figure 4.6 shows the $(\tau_{yy}-\tau_{zz})$ and τ_{yz} from the training data. From the training data a definite structure in $(\tau_{yy}-\tau_{zz})$ is observed with a positive region above and a negative region below the diagonal from $y/h = z/h$. These regions correspond to the two vortices experienced per corner in a square duct as shown in figure 3.3. The positive region corresponds to the anti-clockwise rotating vortex and the negative region the clock-wise rotating vortex. The strength of these vortices is defined by derivative of $(\tau_{yy}-\tau_{zz})$ in y and z as $\frac{\partial}{\partial y}\frac{\partial}{\partial z}(\tau_{yy}-\tau_{zz})$. Therefore the gradients of $(\tau_{yy}-\tau_{zz})$ generate the vorticity. The strongest gradients in y and z is observed near to the walls. Close to the diagonal line the gradient appears constant meaning the second order derivative is close to 0. The near wall region is then considered to be the source of vorticity. When observing τ_{yz} the second derivative in y and z is considered. This means the changes of gradient in y and z are relevant. Given the symmetry around the diagonal $y = z$, this implies that $\frac{\partial^2\tau_{yz}}{\partial z^2} = \frac{\partial^2\tau_{yz}}{\partial y^2}$ near the diagonal. Near the walls τ_{yz} is constant or at least approximately constant, which means $\frac{\partial\tau_{yz}}{\partial z} = \frac{\partial\tau_{yz}}{\partial y} = 0$. Together with the aforementioned conclusion, this supports the argumentation of (Perkins, 1970) and (Huser & Biringen, 1993) that τ_{yz} does not generate vorticity.

When observing the non-linear models calibrated with global coefficients in figure 4.7, the model with 1 coefficient shows similar patterns in $(\tau_{yy}-\tau_{zz})$ as the training data. The contours of τ_{yz} show a different structure than the training data. Higher complexities displayed similar contours as the model shown here. The Reynolds stress profiles of $(\tau_{yy}-\tau_{zz})$ and τ_{yz} for different complexities using the L-BFGS-B results from table 4.1 are plotted in figure 4.8.

From the contour plot for $(\tau_{yy}-\tau_{zz})$ 4 regions can be distinguished. Two smaller regions near the centre of the square duct and two larger regions towards the walls. These larger regions correspond to those found for the training data in figure 4.7. The origin of the smaller regions remains unexplained. When comparing $(\tau_{yy}-\tau_{zz})$ from the non-linear model and the training data near the walls, it can be seen in figure 4.8 that the gradients near the walls predicted by the non-linear model are smaller than those from the training data. Then the non-linear model is expected to predict weaker secondary motions.

For τ_{yz} the non-linear model predicts two local maxima and minima as in the training data. The magnitudes and sizes of regions are not predicted well. Given that $(\tau_{yy}-\tau_{zz})$ is responsible for the secondary motions, the impact of not predicting τ_{yz} accurately cannot be singled out.

Implementing the coefficients from table 4.1 into the RANS solver and plotting the velocity profiles on the sample lines $z/h = 1/4$; $1/2$ and $3/4$ gives figure 4.9. This figure shows the training data as DNS, Boussinesq approximation as baseline and best results including 1, 2, 5 and 9 non-linear tensors from expression (2.36). It is confirmed that the secondary motions are predicted, but much weaker than in the training data. This is attributed to the difference

in predicted and exact $(\tau_{yy} - \tau_{zz})$.

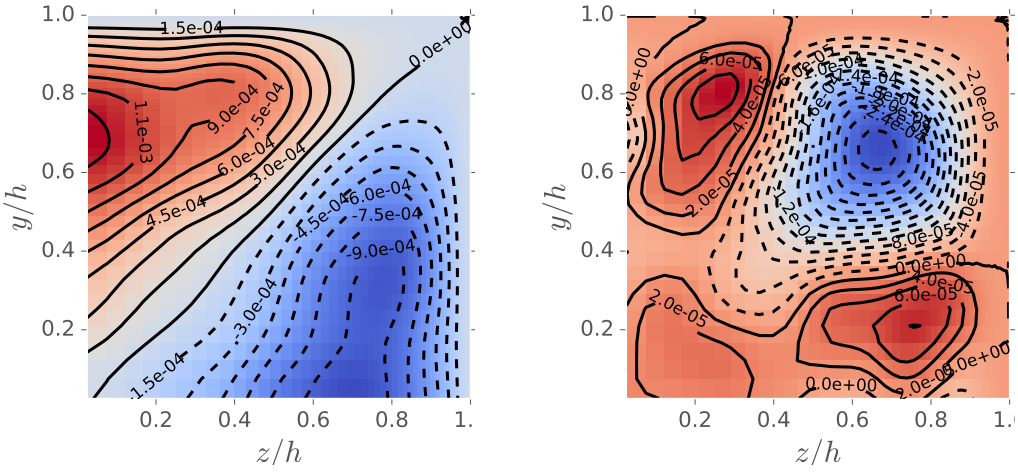

Figure 4.6: Reynolds stress contour plots of $\tau_{yy} - \tau_{zz}$ (left) and τ_{yz} (right) of the training data.

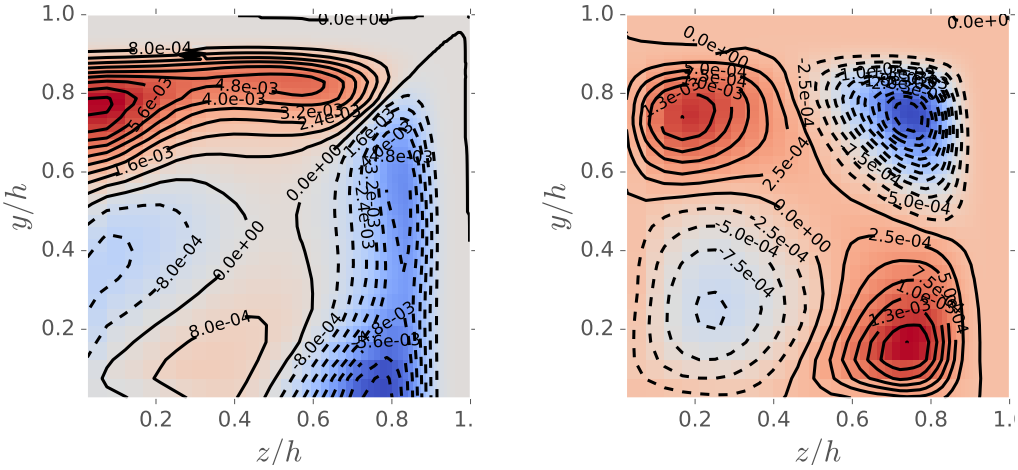

Figure 4.7: Reynolds stress contour plots of predicted $\tau_{yy} - \tau_{zz}$ (left) and predicted τ_{yz} (right) of (2.35) with 1 coefficient.

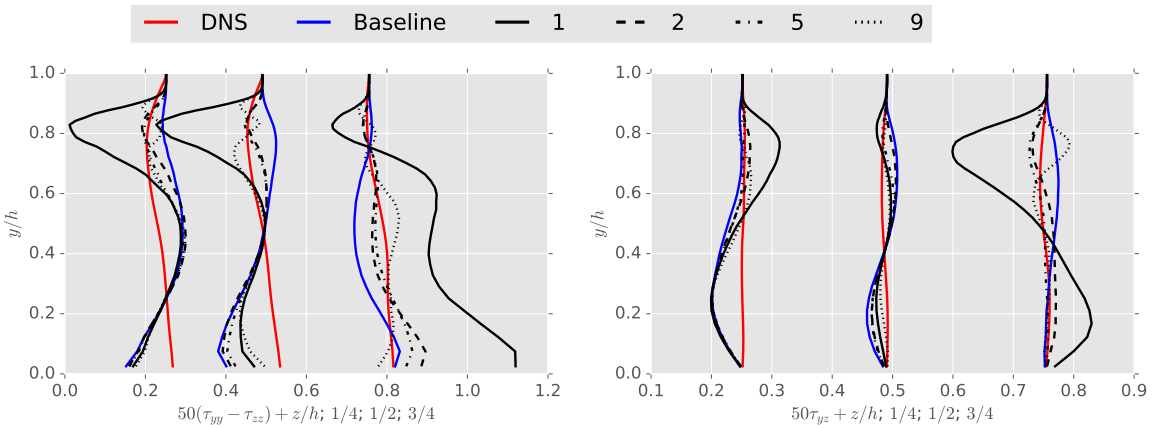

Figure 4.8: Reynolds stress profiles of predicted $\tau_{yy} - \tau_{zz}$ (left) and predicted τ_{yz} (right).

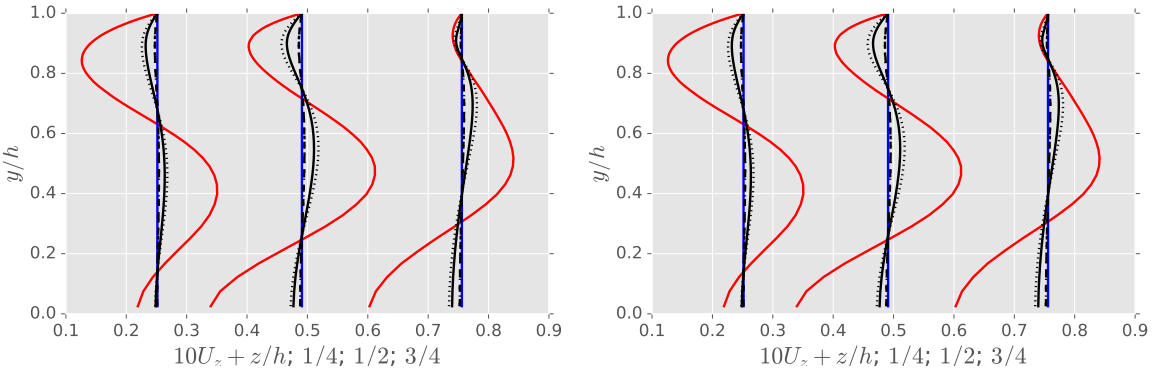

Figure 4.9: Predicted velocity profiles U_y (left) and U_z (right). Training data is DNS, Boussinesq approximation is baseline. 1, 2, 5 and 9 are the best results when including 1, 2, 5 and 9 non-linear tensors in the turbulence model.

4.5 Data-driven vs solver-incorporated calibration

It has been seen that the anisotropy can be corrected given the cost function L_τ from (3.7). Smaller gradients than the training data near the walls for $(\tau_{yy} - \tau_{zz})$ and τ_{yz} were observed. Secondary motions could be predicted in subsection 4.4.2. However these were smaller than those from the training data. Furthermore calibrating the coefficients $\beta_{1,\dots,9}$ assuming the DNS velocity field as input might be flawed due to other sources of error. For example the Boussinesq approximation implies that $u' = v' = w'$, which is not the case in the training data. Therefore even the Boussinesq approximation could predict secondary motions when using the DNS data as input. A connection between the Reynolds-stresses and RANS solver is made in this subsection.

This subsection analyzes the validity of the data-driven calibration by incorporating the RANS solver to the calibration procedure. The optimum coefficients β found from minimizing L_τ (3.7) as defined in table 4.1 for the L-BFGS-B optimization routine were used in the RANS solver. Other sets of optimum β gave the same results and were omitted for clarity. After solving the RANS equations the minimization problem (3.7) was reevaluated with τ_{ij} as a

function of the predicted velocity, turbulent kinetic energy and specific turbulence dissipation instead of the training data. Furthermore the prediction of secondary motions is evaluated with

$$L_U(\beta) = \sum_i \int_{\Omega_a} \frac{\left(u_{exact,i} - \bar{u}_i\left(\beta\right)\right)^2}{\max(u_{exact,i})} d\Omega_a. \tag{3.8}$$

Figure 4.10 shows the relation between using DNS and predicted inputs for the Reynolds stresses τ_{ij} in L_τ (3.7). The improvement to represent secondary motions are evaluated by L_U given by (3.8). All complexities are displayed. From 0, Boussinesq approximation, to 9, considering all non-linear tensors. The axis labels are denoted by $L_\tau^o = L_\tau^o\left(\tau_{ij}^*(U^o, k^o, \omega^o)\right)$ and $L_\tau^* = L_\tau^*\left(\tau_{ij}^*(U^*, k^*, \omega^*)\right)$ with ^{o} being for training data and data-driven and * for predicted data and solver-incorporated. The diagonal line in figure 4.10 shows $L_\tau^* = L_\tau^o = L_U^*$.

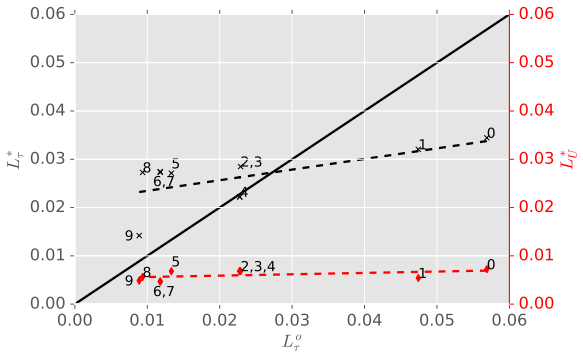

Figure 4.10: Data-driven vs solver-incorporated calibration

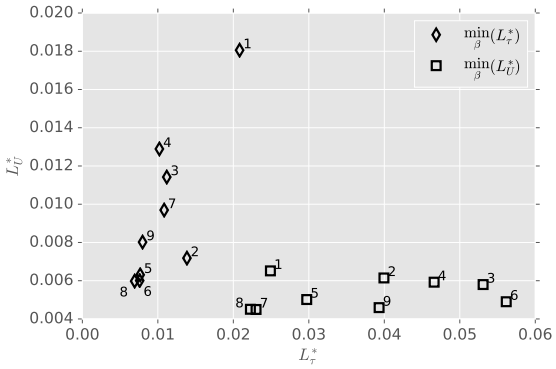

Figure 4.11: Data-driven vs solver-incorporated calibration

In figure 4.10 the points relating to different number of non-linear tensors considered are plotted. It was expected that $L_\tau^* > L_\tau^o$ for all combinations of tensors since L_τ^* is a function of RANS velocity and turbulent kinetic energy fields. However it appears that when using the Boussinesq approximation or only up to and including $T_{ij}^{(1)}$ the RANS data is more accurate in predicting the DNS Reynolds stresses τ_{ij}^o than the DNS data for the given turbulence model. The remaining complexity levels are as expected above the diagonal $L_\tau^* = L_\tau^o$. Despite this peculiarity that some $L_\tau^* < L_\tau^o$, a clear trend is observed. For a reduction of L_τ^o using the data-driven approach a reduction of L_τ^*, being solver-incorporate, is achieved. A linear function is fitted through the data points resulting in the black dotted line. The slope of the function is ≈ 0.4. Meaning that a reduction in $L_\tau^* \approx 0.4 L_\tau^o + 0.01$. This justifies the minimization strategy of minimizing L_τ (3.7) without solving the RANS equations at each iteration but only evaluating the Reynolds stresses τ_{ij} with (2.35).

Since the final goal of this research is to derive coefficients β to better predict secondary motions, L_U (3.8) was evaluated. The relation between L_τ^o and L_U^* is shown by the red markers in figure 4.10. From the markers alone it can already be seen that a reduction in L_τ^o does not lead to a reduction in L_U^*. This is confirmed by making a linear relation through the data points obtaining a slope of ≈ 1. Having found a potential inability to predict secondary motions with the data-driven calibration a Monte-Carlo simulation is preformed solving the RANS model for random β.

A Monte-Carlo simulation was set up with 1 to 9 coefficients with margins -10 to 10 for each coefficient. A total of at least $200n$ samples are considered for each complexity, with n indicating how many non-linear tensors are considered (complexity). Both loss functions L_τ given by equation (3.7) and L_U given by equation (3.8) are considered as minimization problems. The obtained relationship between the minimization problems is given in figure 4.11. The markers indicate the minimization problem, the numbers the complexity and the axis the loss function value. It is observed that no correlation exists between minimizing one or the other loss function. At different complexities, $\min_\beta L_\tau$ is constant in L_U as seen by the squares, and vice-versa $\min_\beta L_U$ is constant in L_τ as seen by the diamonds. The lack of correlation between these loss functions shows that this way of calibrating does not work. Different combinations of β although improving the Reynolds stress prediction do not improve the prediction of secondary motions. This can also mean that the inability to predict secondary motions might not be exclusively the Boussinesq approximation but also other factors within the turbulence model might play a role. Such as the use of global-coefficients or the k or ω transport equations.

4.6 Discussion

Having found that no relation between the two loss functions L_τ (3.7) and L_U (3.8) can be found another calibration procedure is necessary. Two approaches are suggested: 1. Solver-incorporated calibration with optimization routine and 2. solver-incorporated calibration with surrogate modelling.

1. The first approach requires a CFD run per search step in an optimization routine rendering a very expensive approach. With the availability of computational resources also a Monte-Carlo method can be used which can be highly parallelized to evaluate random samples in a given search space and then approximate the optimum.
2. The second approach requires fewer CFD runs and a model that interpolates between the runs. This approach is less computationally expensive, is however dependent on the interpolation. Which can, if not done well, induce additional errors.

Given the availability of a cluster in this research the first approach is selected with a Monte-Carlo simulation and explored in the next chapter.

Chapter 5

Solver-incorporated calibration

In this chapter the solver-incorporated calibration is discussed. A Monte-Carlo simulation is performed with random samples ranging between -10 and 10 for each coefficient. Two separate runs are performed;

1. considering 1 to 9 non-linear tensors or coefficients $\beta \neq 0$ with at least $200n$ converged samples, with n indicating the number of tensors considered or coefficients $\beta \neq 0$.

2. with 5 coefficients considering 24,000 samples of which 15,089 converged which are used for Sobol sensitivity analysis

The loss functions studied as minimization problems are L_τ and L_U given by (3.7) and (3.8).

$$L_\tau(\beta) = \sum_{ij} \int_{\Omega_a} \frac{\left(\tau_{exact,ij} - \bar{\tau}_{ij}\left(\beta\right)\right)^2}{\max(\tau_{exact,ij})} d\Omega_a \tag{3.7}$$

$$L_U(\beta) = \sum_{i} \int_{\Omega_a} \frac{\left(u_{exact,i} - \bar{u}_{i}\left(\beta\right)\right)^2}{\max(u_{exact,i})} d\Omega_a \tag{3.8}$$

The remainder of this section is organized as follows; In section 5.1 a sensitivity analysis is performed including Sobol indices and kernel density estimates. In subsection 5.2 the optimum results in terms of anisotropy and velocity are presented. The global-coefficient non-linear eddy viscosity model is compared to other non-linear eddy viscosity models in section 5.3. In section 5.4 the chapter is concluded with a discussion on the solver-incorporated calibration.

5.1 Sensitivity analysis

In this section a sensitivity analysis is performed. This is done in 3 ways; analyzing a cost-complexity relation, with kernel density estimations (kde's) and Sobol index analysis.

5.1.1 Cost-complexity analysis

The cost-complexity relation is obtained from a Monte-Carlo simulation of at least $200n$ converged samples with $-10 \leq \beta \leq 10$ where n indicates the number of coefficients $\neq 0$. The cost-complexity plot, figure 5.1, analyzes the loss function value L_U^* and L_τ^* as cost in terms of the number of coefficients given as complexity. The superscript * indicates as a function of predicted velocities, turbulent kinetic energy and turbulence dissipation. A complexity of 0 indicates the Boussinesq approximation, 1 indicates $\beta_1 \neq 0$ and $\beta_{2 \text{ to } 9} = 0$ and so on. From figure 5.1 it is observed that tensors 4 and 6 to 9 have the least influence towards the reduction of cost in terms of L_U^* and L_τ^*, whilst tensors 1, 2, 3 and 5 have the largest influence. The cost reduction obtained by minimizing L_U^* by using just 1 tensor is 54% and by using 5 coefficients is 64%. Adding all 9 tensors results in a reduction of 67%. When minimizing L_τ^* reductions of 40% at complexity 1 is observed and a constant 77% reduction from complexities 5 to 9 excluding 7. The low influence of tensors 4 and 6 to 9 in terms of loss function is in accordance with the results found from the data-driven calibration. The largest surprise is the cost reduction of L_U^* and L_τ^* achieved by including the third tensor. This one was found to be correlated to the second tensor and therefore having a smaller impact.

5.1.2 Kernel density estimates

From the same Monte-Carlo simulation as used for the cost complexity analysis the kernel density estimates (kde's) are plotted. The simulation including all 9 coefficients is considered. This one contains $2,140$ converged samples for $-10 \leq \beta \leq 10$. Figure 5.3 shows the kde's of L_U^* and L_τ^* when evaluated as minimization problems and taking the best 100 samples. The blue line represents the kde for the converged samples, the green line the best 100 samples in terms of $\min_\beta L_U^*$ and the red line the best 100 samples in terms of $\min_\beta L_\tau^*$.

In figure 5.3 it is observed that $\min_\beta L_\tau^*$ is better informed than $\min_\beta L_U^*$. The kde's of $\min_\beta L_\tau^*$ and $\min_\beta L_U^*$ do not overlap for coefficients 1, 2 and 3. Coefficients 4 and 6 to 9 are not informed for either minimization problem and also considered of low influence as shown by the cost-complexity analysis. Coefficient 4 is the greatest surprise given that in the data-driven calibration it was found to be approximately 0 for all optimization routines and here it is not well informed for either minimization problem. Meaning that even if $\beta_4 \neq 0$ its tensor $T_{ij}^{(4)}$ has no effect towards the minimization problems.

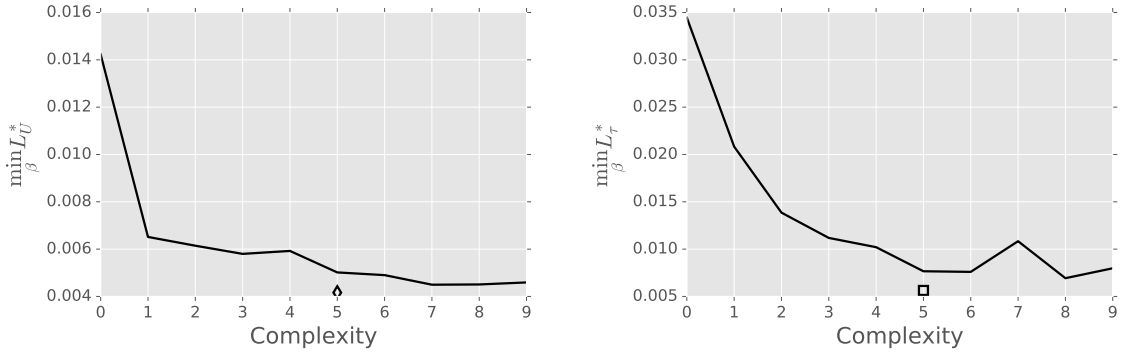

Figure 5.1: Cost complexity plots for $\min_\beta L_U^*$ (left) and $\min_\beta L_\tau^*$ (right). Markers represent the minimum found from the Sobol index analysis with 5 coefficients and 15,089 converged samples.

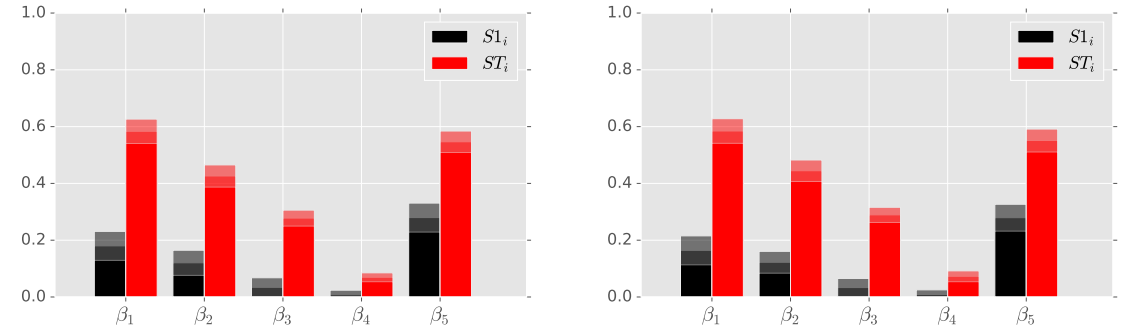

Figure 5.2: Sobol indices $S1$ and ST for for L_U^* (left) and L_τ^* (right).

5.1.3 Sobol indices

The Sobol indices are computed for $\beta_{1 \text{ to } 5} \neq 0$ and $\beta_{6 \text{ to } 9} = 0$. A total of 24,000 samples were evaluated of which 15,089 converged. The Sobol indices were not computed for all 9 coefficients due to the extravagant computational cost of obtaining sufficient samples for Sobol index convergence. Figure 5.2 shows the first order $S1$ and total ST Sobol indices for the first 5 coefficients. It is observed in figure 5.2 that the 1^{st} and 5^{th} coefficients are the most influential towards L_U^* and L_τ^*. Both as stand alone (large $S1$) and in terms of correlations (large ST). Coefficients 2 and 3 have lower influence on L_U^* and L_τ^* shown by smaller $S1$ and ST. With the fourth coefficient having a small influence.

In order to analyze the correlations between the first 5 coefficients scatter plots are created with one coefficient on the y-axis, another on the x-axis and using color to indicate the value of loss function. A binary color scheme is selected to highlight the impact of the loss function. White spaces represent high values for the loss function and black dots low values. Uniform gray regions indicate solver instability where no converged samples exist. In figure 5.4 on the left (L_U^*) it can be observed that the lowest loss function values are found towards the unstable region. Correlations are found between β_1, β_2 and β_3 as $\beta_1 \approx \beta_2$, $\beta_1 \approx -\beta_3$ and

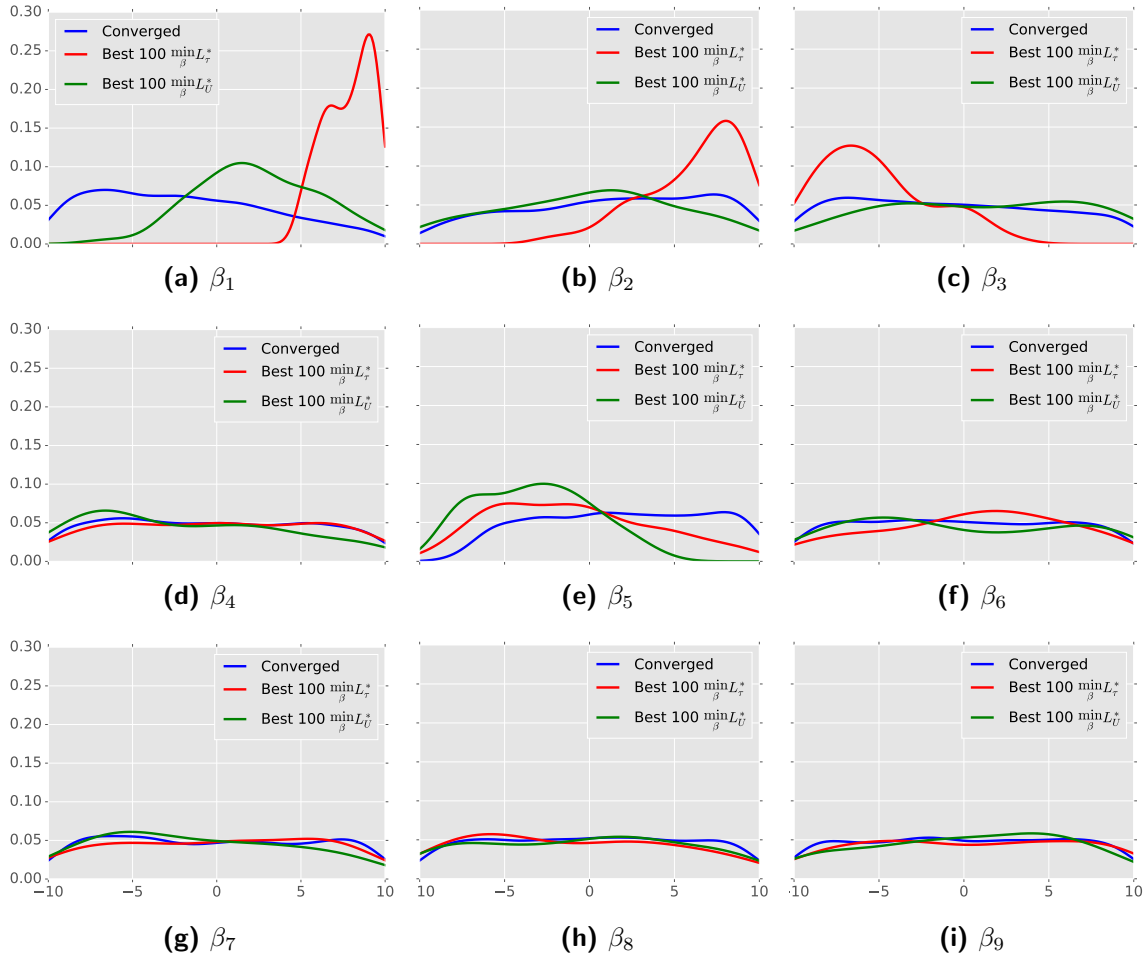

Figure 5.3: Kernel density estimations (kde's) for coefficients β.

$\beta_2 \approx -\beta_3$. The 5^{th} coefficient β_5 is found to be ≈ -5.7 for small loss function values, close to the stability boundary. The 4^{th} coefficient shows no correlations as indicated by its second and total Sobol indices. In figure 5.4 on the right (L_τ^*) a clear pattern is found maximizing β_1 and β_2, whilst minimizing β_3. No correlations for β_4 and β_5 can be made. Comparing the left and right of figure 5.4 it becomes clear again that minimizing L_τ^* will not lead to a minimization of L_U^*. The prediction of correct velocities appears to be more dependent on the choice of turbulence model than correct Reynolds stresses.

5.1.4 Optimum coefficients

From the calibration different sets of optimum coefficients β are selected. From $\min_\beta L_U^*$ the coefficients β were found to vary largely as also indicated by many optimum regions in the scatter plot 5.4. The optimum β selected for further analysis are given in table 5.1. On the square duct all these combinations were found to give identical results. In terms of $\min_\beta L_\tau^*$ the coefficients were better informed in the kde analysis. Therefore fewer models are studied.

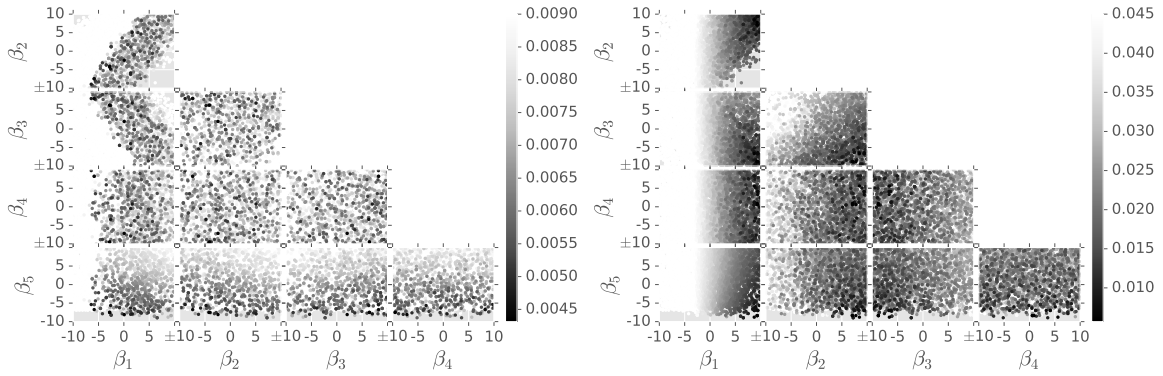

(a) Scatter plot of L_U^*.

(b) Scatter plot of L_τ^*.

Figure 5.4: Scatter plot for the first 5 coefficients indicating the loss function value with a binary colormap. Darker color indicates lower loss function value.

The optimum β selected for further analysis from $\min_\beta L_\tau^*$ are given in table 5.1.

From tables 5.1 and 5.1 the same result as in figure 4.11 is found. There is no correlation between the coefficients from minimizing one vs the other loss function.

Table 5.1: Optimum coefficients β found from $\min_\beta L_U^*$. β_4 is omitted since it is considered of no influence and its coefficient is set to $\beta_4 = 0$ for all combinations.

Model name	Combinations β_1	β_2	β_3	β_5
$\min_\beta L_U$ 1	3.83			
$\min_\beta L_U$ 2.1	-1.19	-8.73		
$\min_\beta L_U$ 2.2	0.61	-5.72		
$\min_\beta L_U$ 2.3	1.74	-3.85		
$\min_\beta L_U$ 3.1	-4.37	-7.81	7.95	
$\min_\beta L_U$ 3.2	-2.78	-7.05	5.72	
$\min_\beta L_U$ 3.3	-3.20	-5.24	8.96	
$\min_\beta L_U$ 3.4	-1.65	-6.01	4.29	
$\min_\beta L_U$ 3.5	1.62	-5.22	-1.63	
$\min_\beta L_U$ 3.6	1.03	-2.38	3.54	
$\min_\beta L_U$ 5.1	-2.80	-4.23	6.44	-7.51
$\min_\beta L_U$ 5.2	-1.46	-0.38	7.43	-7.88
$\min_\beta L_U$ 5.3	-5.85	-7.43	9.50	-5.40
$\min_\beta L_U$ 5.4	1.12	0.56	3.28	-8.50
$\min_\beta L_U$ 5.5	1.06	-7.42	-5.63	-7.93
$\min_\beta L_U$ 5.6	2.28	-2.41	-3.04	-8.35

Table 5.2: Optimum coefficients β found from $\min_\beta L_\tau^*$. β_4 is omitted since it is considered of no influence and its coefficient is set to $\beta_4 = 0$ for all combinations.

Model name	Combinations β_1	β_2	β_3	β_5
$\min_\beta L_\tau$ 1	9			
$\min_\beta L_\tau$ 2	9	9		
$\min_\beta L_\tau$ 3	9	8	-9	
$\min_\beta L_\tau$ 5	9	9	-9	-6

5.2 Results

The calibrated global-coefficient NLEVM results are presented in this section. The results are divided into three subsections. First the anisotropy correction is discussed followed by the Reynolds stress components responsible for secondary motions. Finally the velocity profiles are presented. All results are shown on the sample lines $z/h = 1/4$; $1/2$ and $3/4$ shown by the red lines in figure 3.3.

5.2.1 Anisotropy

The implementation of the non-linear tensors (2.36) was argued by Lumley (1970), Pope (1975) and other authors to correct the anisotropy prediction. In this subsection the anisotropy obtained from the calibrated global-coefficient NLEVM is presented. Figure 5.5 shows the anisotropy on the sample lines $z/h = 1/4$; $1/2$ and $3/4$ for complexities 1, 2 and 5. Higher complexities than 5 showed a similar result figure 5.5 (c) and complexities 3 and 4 are similar to complexity 2. The anisotropies of the training data, Boussinesq approximation and both minimization problems are shown. Different to the results from the data-driven calibration from chapter 4, all predicted anisotropies from the solver-incorporated calibration fulfill the realizability constraints and are located within the barycentric map (Schumann, 1977; Banerjee et al., 2007) (see appendix D).

For complexity 1 both minimization problems are found to have similar anisotropies. Not much anisotropy is corrected given that the anisotropy is similar to that predicted by the Boussinesq approximation. Increasing the complexity also increases the anisotropy. $min_\beta L_\tau^*$ shifts to the right of the plane strain approaching the 1-component turbulence state where also the training data is located. $min_\beta L_U^*$ shifts towards the left of the plane strain. It was expected that $min_\beta L_\tau^*$ performed better in terms of anisotropy since it reduces the error between the exact and predicted Reynolds stresses. It was not expected that $min_\beta L_U^*$ is worse than the Boussinesq approximation in predicting the anisotropy of the flow. This suggests that mapping from Reynolds stresses to velocity field is strongly dependent on turbulence model. Classifying the act of calibrating the NLEVM with global coefficients to improve the velocity prediction by minimizing L_U^*(3.8) to be an act of unphysical mapping from Reynolds stresses to velocity field rather than a physical one. Then completely different Reynolds stress fields from the training data can obtain the same velocity field as the training data.

At increasing complexity $min_\beta L_\tau^*$ continues to correct the anisotropy whilst $min_\beta L_U^*$ shows similar anisotropies for all complexities larger than 1. This is in accordance with the cost complexity 5.1 where the L_U^* showed very limited improvement at increasing complexity after the introduction of the first non-linear tensor whilst L_τ^* continued to reduce the cost at increasing complexity up to complexity 5.

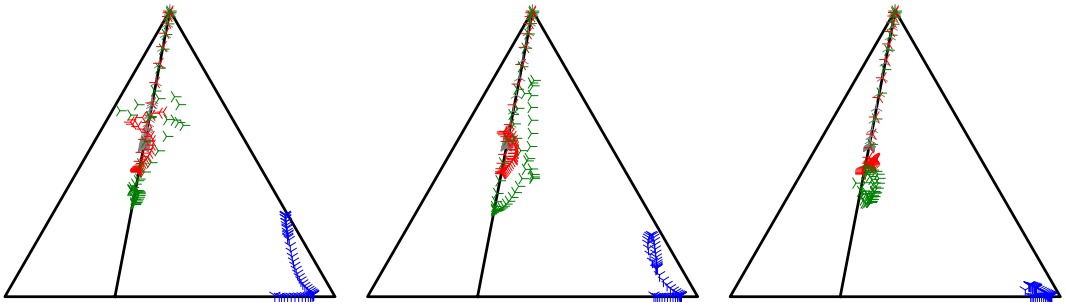

(a) Complexity of 1; $\beta_1 \neq 0$ and $\beta 2, ..., 9 = 0$

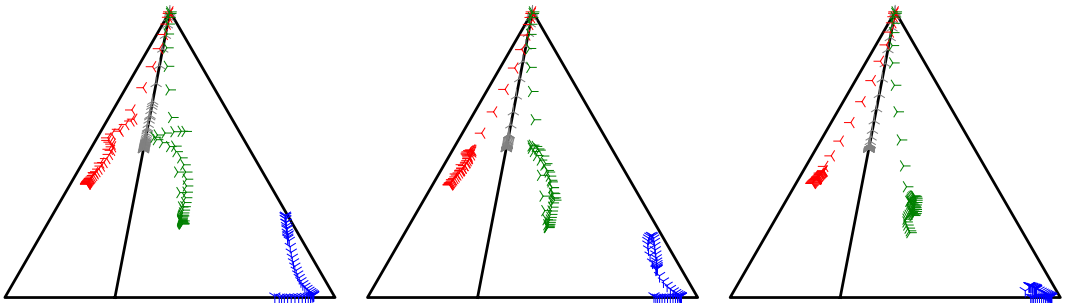

(b) Complexity of 2; $\beta_{1,2} \neq 0$ and $\beta 3, ..., 9 = 0$

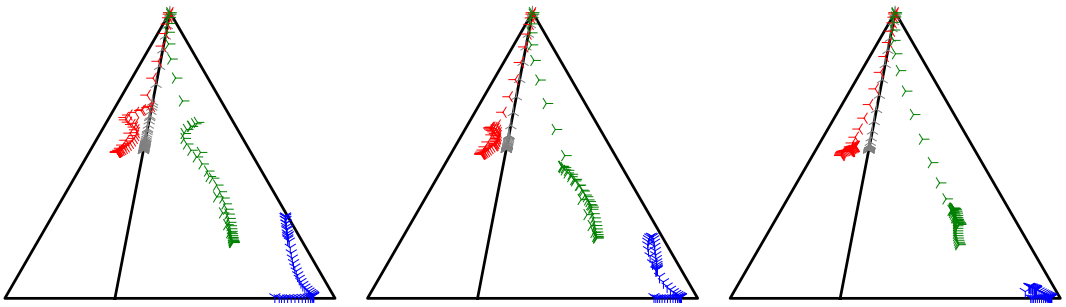

(c) Complexity of 5; $\beta_{1,...,5} \neq 0$ and $\beta 6, ..., 9 = 0$

Figure 5.5: Anisotropy on samples lines $z/h = 1/4$ (left); $1/2$ (centre); $3/4$ (right).

5.2.2 Reynolds stress to secondary motion analysis

The secondary motions described by u_y and u_z are determined with equation (1.5).

$$\left(\frac{\partial^2}{\partial z^2} - \frac{\partial^2}{\partial y^2}\right)\tau_{yz} + \frac{\partial}{\partial y}\frac{\partial}{\partial z}\left(\tau_{yy} - \tau_{zz}\right) = \left(\frac{\partial^2}{\partial y^2} - \frac{\partial^2}{\partial z^2}\right)\left(\nu_t\left(\frac{\partial u_y}{\partial z} + \frac{\partial u_z}{\partial y}\right)\right) + 2\frac{\partial}{\partial y}\frac{\partial}{\partial z}\left(\nu_t\left(\frac{\partial u_z}{\partial z} - \frac{\partial u_y}{\partial y}\right)\right) \tag{(1.5)}$$

This expression depends on $(\tau_{yy} - \tau_{zz})$, τ_{yz}, k and ω. Plotting the profiles of these quantities, using the turbulent viscosity $\nu_t = k/\omega$ instead of ω figure 5.6 is obtained. Adding more coefficients gave only small variations in these plots and are therefore omitted. It is seen

that from using only the first non-linear tensor the secondary motions can be predicted as shown by $(\tau_{yy} - \tau_{zz}) \neq 0$. The predicted Reynolds stress difference follows a similar shape than the training data. In magnitude the prediction of $(\tau_{yy} - \tau_{zz})$ from the global-coefficient NLEVM is approximately 4.5 times larger than that of the training data. τ_{yz} is over predicted by an approximate factor of 3.7 in magnitude. However near the wall, the gradients, which determine the secondary motions, are similar if not smaller, than that of the training data. The turbulent kinetic energy k and turbulent viscosity ν_t are predicted fairly well and show only little variation for different combinations of β (grey lines). From this it can be said that these quantities, which depend on the Reynolds stresses via the production term are not very sensitive to the Reynolds stresses.

For complexity 1, $\beta_1 \neq 0$ and $\beta_{2 \text{ to } 9} = 0$, the contours of $(\tau_{yy} - \tau_{zz})$ and τ_{yz} are plotted in comparison to the DNS data in figure 5.7. Adding further non-linear tensors showed little improvement. From figure 5.7 it can be concluded that the models originating from minimizing L_τ^* and L_U^* predict a similar near wall behavior in terms of $(\tau_{yy} - \tau_{zz})$. Both minimization problems exhibit a larger region of approximately constant $(\tau_{yy} - \tau_{zz})$ near the wall than the training data. In terms of τ_{yz} both minimization problems show different contours as that of the training data. From $(\tau_{yy} - \tau_{zz}) \neq 0$ both minimization problem should predict secondary motions as shown in figure 5.8.

Figure 5.8 shows the quiver plots of the secondary motions in the square duct of the training data and both minimization problems. As expected from the correction of anisotropy $(\tau_{yy} - \tau_{zz}) \neq 0$ secondary motions are present in both calibrated models. $min_\beta L_\tau^*$ displays a different pattern for secondary motions than $min_\beta L_U^*$ for complexity 1. For higher complexities all quiver plots are similar to 5.8 (b). 5.8 (b) displays the existence of secondary motions similar to the training data. The vortices are of similar strength, but the centre of rotations are shifted towards the top right corner. The next subsection will analyze the velocity profiles.

5.2.3 Velocity profiles

The velocity profiles from $\min_\beta L_U^*$ and $\min_\beta L_\tau^*$ when using 1, 2 and 5 coefficients are shown in figure 5.9. Higher complexities show no further improvements and are therefore not shown. The complexities are selected based on their influence as shown in subsection 5.1. The results are compared to the baseline (linear) model and to the training data (DNS). Figure 5.9 shows the velocity u_y and u_z on $z/h = 1/4; 1/2; 3/4$ for varying complexities. These figures show in gray the samples obtained from the Monte-Carlo simulation. Darker gray areas depict higher density of samples. In blue is the baseline model, obtained from the Boussinesq approximation. In red is shown the DNS solution. In black are the results obtained from the minimization problems $\min_\beta L_U^*$ (-) and $\min_\beta L_\tau^*$ (- -).

In figure 5.9 it can be seen that all complexities predict secondary motions. With $\min_\beta L_U^*$ being better in predicting the DNS velocity profiles than $\min_\beta L_\tau^*$. There is little effect of adding more coefficients than 1 when observing $\min_\beta L_U^*$ whilst at least two coefficients are necessary for $\min_\beta L_\tau^*$. At complexities 2 and 5 the solutions for the two minimization problems almost overlap.

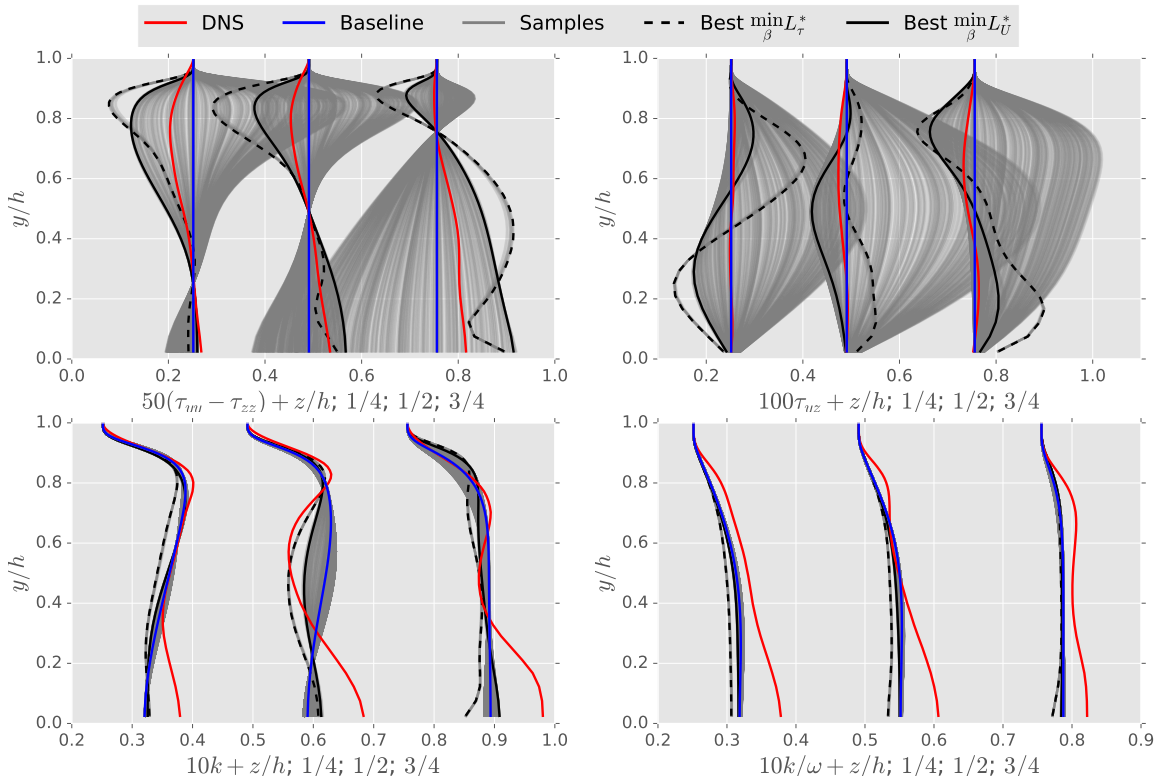

Figure 5.6: Reynolds stress profiles $\tau_{yy} - \tau_{zz}$ (top left), τ_{yz} (top right), turbulent kinetic energy profile k (bottom left) and turbulent viscosity profile $\nu_t = k\omega$ (bottom right) at samples lines $z/h = 1/4; 2/4; 3/4$ considering 1 non-linear tensor.

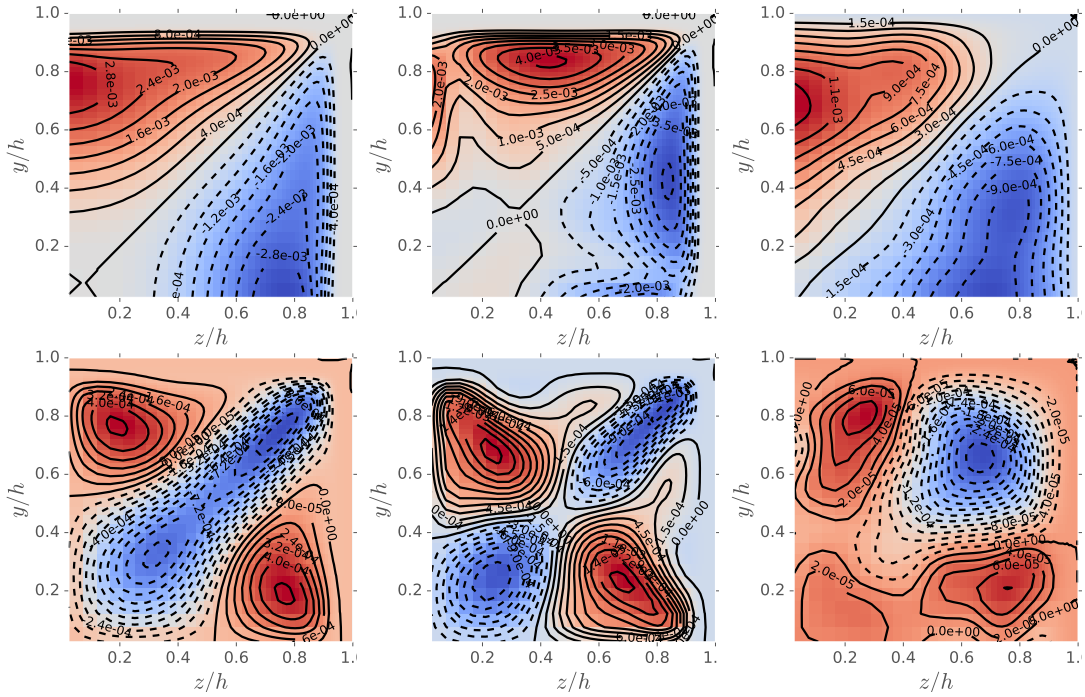

Figure 5.7: Contour plots of $(\tau_{yy} - \tau_{zz})$ (top) and τ_{yz} (bottom) when minimizing L_U^* (left), L_τ^* (centre) and using DNS data (right).

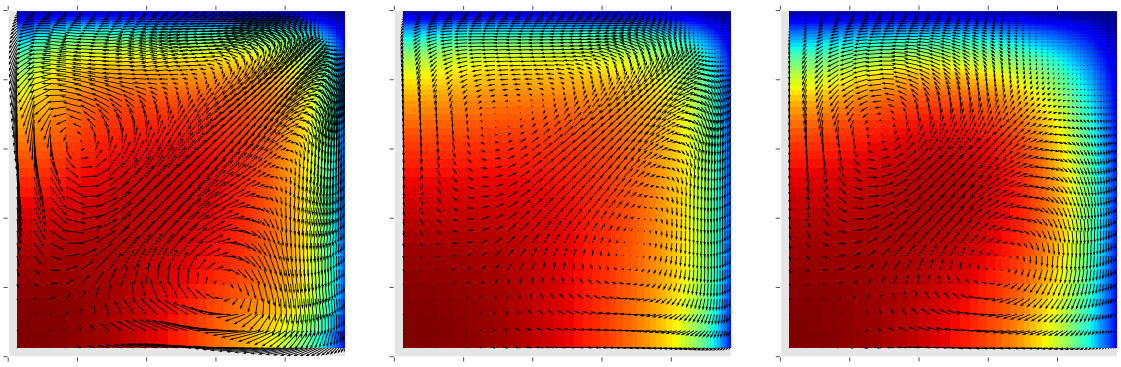

(a) $min_\beta L_\tau^*$ **(b)** $min_\beta L_U^*$ **(c)** DNS

Figure 5.8: Quiver plot of secondary motions of both optimization routines and training data. The colormap represents the stream-wise velocity U_x.

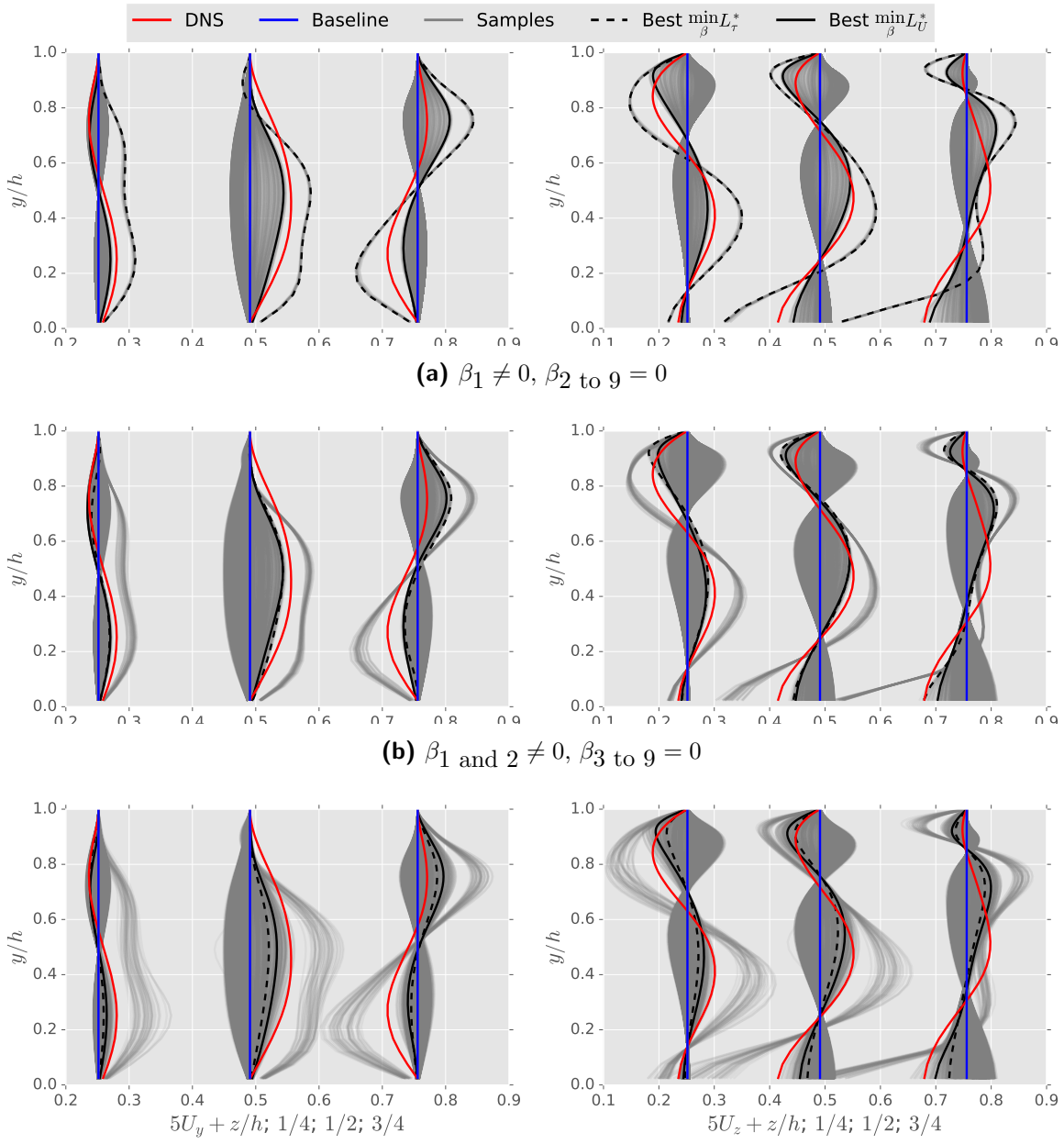

(a) $\beta_1 \neq 0$, $\beta_{2 \text{ to } 9} = 0$

(b) $\beta_{1 \text{ and } 2} \neq 0$, $\beta_{3 \text{ to } 9} = 0$

(c) $\beta_{1 \text{ to } 5} \neq 0$, $\beta_{6 \text{ to } 9} = 0$

Figure 5.9: Velocity profiles U_y (left) and U_z (right) at samples lines $z/h = 1/4; 2/4; 3/4$ considering 1, 2 and 5 non-linear tensors.

5.3 Comparison to other non-linear models

Having displayed the capabilities of a non-linear eddy viscosity model with global coefficients on the training case, it is compared to existing non-linear eddy viscosity models implemented in OpenFOAM. Namely the Shih and Lumley (1993) quadratic and Lien et al. (1996) cubic models. These models are described in chapter 2.

The anisotropy prediction of all the models is depicted in figure 5.10 for complexity 2, $\beta_{1 \text{ and } 2} \neq 0$, $\beta_{3 \text{ to } 9} = 0$. The Shih and Lien model display the same anisotropy. Which is considerably closer to the plane strain than that from the global-coefficient NLEVM. It appears as if the task of the Shih and Lien models is not to improve the anisotropy prediction but rather to predict a good velocity field from a wrong Reynolds stress prediction.

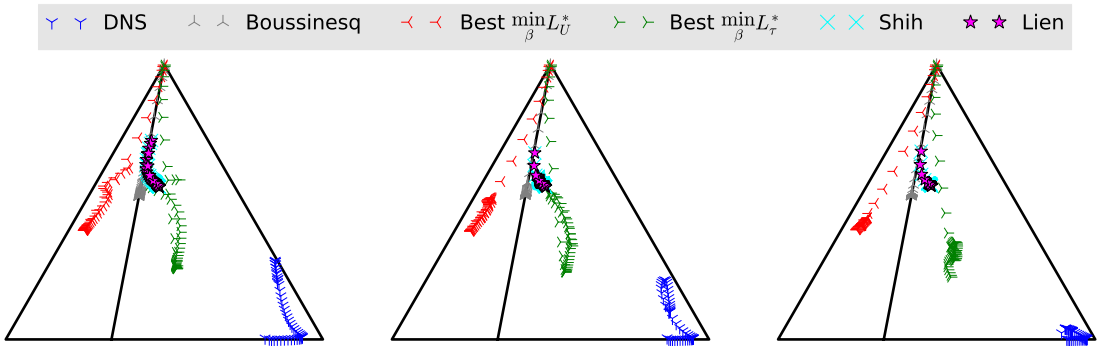

Figure 5.10: Anisotropy on samples lines $z/h = 1/4$ (left); 2/4 (centre); 3/4 (right).

Figure 5.11 shows velocity profiles obtained from the DNS, linear model, global-coefficient NLEVM with 2 non-linear tensors and Shih and Lien models. Surprisingly, despite predicting anisotropy the Lien model fails to predict any secondary motion. The differences between the Shih, Lien and non-linear models with 2 non-linear tensors is the wall treatment. The Shih and Lien models use a function C_μ near the wall that multiplies eddy viscosity ν_t as described in 2.5.1. This function lowers ν_t near the wall, thereby reducing the Reynolds stresses and vorticity. The Lien model furthermore uses a wall damping function f_μ to reduce the turbulent Reynolds stress influence near the wall, leading to $(\tau_{yy} - \tau_{zz}) \approx 0$ near the wall. As a result no vorticity is generated. Figure 7.10 shows the behavior of f_μ near the wall.

In conclusion the wall-treatment appears to have a major effect towards the prediction of flow features such as the secondary motions. The global coefficient models use no wall treatment and reproduce the secondary motions the best. Whilst the Shih model with only making ν_t a function of C_μ still captures secondary motions but it under-predicts them by more than a factor of 10. The Lien model fails to capture the secondary motions in the first place.

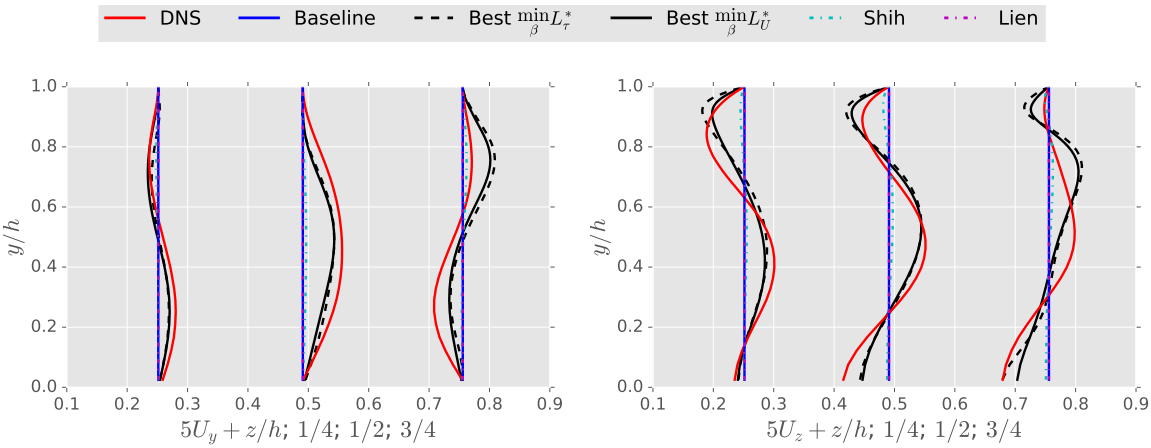

(a) $\beta_{1 \text{ and } 2} \neq 0$, $\beta_{3 \text{ to } 9} = 0$

Figure 5.11: Velocity profiles U_y (left) and U_z (right) at samples lines $z/h = 1/4; 2/4; 3/4$ with 2 non-linear tensors.

5.4 Discussion

In this chapter the calibration of the loss functions L_τ (3.7) and L_U (3.8) using the solver incorporate method was presented. A considerable improvement in terms of anisotropy and secondary motion prediction could be achieved. The global-coefficient calibrated NLEVM outperformed significantly the existing quadratic Shih and cubic Lien models. The main difficulty found was in the determination of optimum β. A variety of combinations of β were found to predict very well the Reynolds stresses or velocities. In fact largely different combinations of coefficients provided identical results. From this it is concluded that the NLEVM rather than being accurate in predicting both, Reynolds stresses and velocities, attempts to create an unphysical map between these quantities.

Chapter 6

Rectangular-duct prediction

The global-coefficient non-linear eddy viscosity model (NLEVM) has improved capabilities of predicting anisotropy and secondary motions. In this chapter the models derived in chapter 5 are used to predict a rectangular-duct flow. A rectangular-duct exhibits similar flow features such as secondary motion in the form of corner vortices making it a good first step to evaluate the performance of the global-coefficient NLEVM. A 2:1 rectangular-duct as presented in subsection 3.5.2 is considered. All combinations from tables 5.1 and 5.2 and the quadratic Shih and cubic Lien models are used for predictions. First the stability and flow field prediction are analyzed followed by an analysis of the anisotropy.

6.1 Solver stability and flow field prediction

Table 6.1 showcases the stability and prediction quality of each combination of coefficients β and the Shih and Lien models on the rectangular-duct. The stability is assessed by whether the solver breaks down (-) or converges (+). A forward slash (/) is used to show fair convergence which means the ramping factor did not reach $\xi = 1$ but the model could be converged with $\xi \geq 0.6$.

The prediction quality is assessed in a qualitative manner by comparing the predictions to the experiment from Xiao et al. (2016) shown in figure 6.1 (a). A good prediction (+) is shown in figure 6.1 (b). Fair predictions (/) are shown in figure 6.1 (c) and (d). Poor predictions (-) are shown in figure 6.1 (e) and (f).

Most converged models with the exceptions of non-linear models $\min_\beta L_U$ 5.6 and $\min_\beta L_\tau$ 1, 3 and 5 and Lien were able to do a good prediction of secondary motions similar to that shown in figure 6.1 (b). Fair predictions were done by non-linear models $\min_\beta L_\tau$ 3 and 5. Non-linear model $\min_\beta L_\tau$ 3 predicted secondary motions as shown in 6.1 (c), with the size of the smaller vortex under predicted. Non-linear model $\min_\beta L_\tau$ 5 predicted both corner vortices, with the

centres of rotation at wrong locations as shown in 6.1 (d). Non-linear models $\min_\beta L_U$ 5.5 and Lien failed to predict secondary motions as shown in figure 6.1 (f) by the lack of two vortices.

The models derived from the minimization problem $\min_\beta L_U$ consistently outperformed those obtained from the minimization problem $\min_\beta L_\tau$. This indicates that improving the Reynolds stress prediction does not guarantee a better prediction of secondary motions. Most models obtained from $\min_\beta L_U$ also outperform the existing non-linear Shih model which predicted weaker secondary motions.

Table 6.1: Stability and quality of prediction of rectangular-duct flow using different global-coefficient NLEVM as defined in tables 5.1 and 5.2 and quadratic Shih and cubic Lien models. + represents good stability and prediction performance, / represents medium stability and prediction performance and - represents instability and poor prediction performance.

Model name	Rectangular-duct Stability	Prediction
$\min_\beta L_U$ 1	+	+
$\min_\beta L_U$ 2.1	+	+
$\min_\beta L_U$ 2.2	+	+
$\min_\beta L_U$ 2.3	+	+
$\min_\beta L_U$ 3.1	+	+
$\min_\beta L_U$ 3.2	+	+
$\min_\beta L_U$ 3.3	+	+
$\min_\beta L_U$ 3.4	+	+
$\min_\beta L_U$ 3.5	+	+
$\min_\beta L_U$ 3.6	+	+
$\min_\beta L_U$ 5.1	+	+
$\min_\beta L_U$ 5.2	+	+
$\min_\beta L_U$ 5.3	+	+
$\min_\beta L_U$ 5.4	-	
$\min_\beta L_U$ 5.5	/	+
$\min_\beta L_U$ 5.6	+	-

Model name	Rectangular-duct Stability	Prediction
$\min_\beta L_\tau$ 1	+	-
$\min_\beta L_\tau$ 2	+	+
$\min_\beta L_\tau$ 3	+	/
$\min_\beta L_\tau$ 5	+	/

Model name	Rectangular-duct Stability	Prediction
Shih	+	+
Lien	+	-

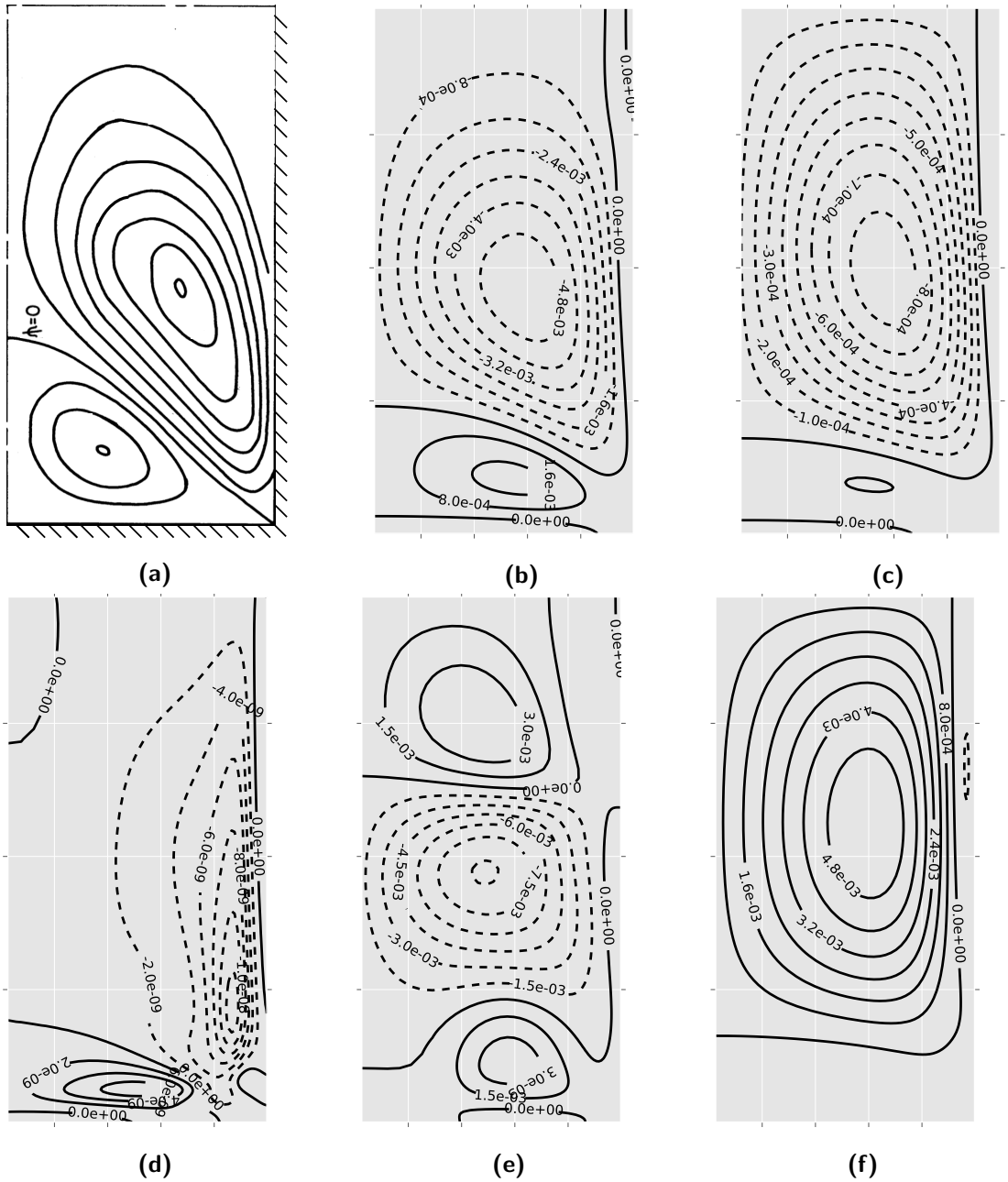

Figure 6.1: Experimental results for rectangular-duct flow. Experiment in (a), good prediction in (b), Fair predictions in (c) and (d), poor predictions in (e) and (f).

6.2 Anisotropy prediction

In this section the anisotropy is evaluated. Due to a lack of high fidelity data on the rectangular-duct only a comparison between the derived global-coefficient NLEVM and the Shih and Lien models can be made. The anisotropy of random cells over the entire flow field is plotted in the barycentric maps in figure 6.2. The data is divided into 5 barycentric maps

for clarity.

From figures 6.2 it can be seen that at increasing complexity, $\min_\beta L_U$ shifts the anisotropy towards the left of the plane strain whilst $\min_\beta L_\tau$ shifts it towards the right. The Shih model predicts mostly plane strain with a small shift towards the 1-component turbulence. The Lien model predicts almost exclusively plane strain. From the result of the square duct, figure 5.10, it is expected that the real anisotropy lies towards the 1-component turbulence (bottom right corner). Only the $\min_\beta L_\tau$ non-linear models correct the anisotropy towards the 1-component turbulence. Together with the secondary motion prediction of the previous section it can be concluded that the turbulence model serves as a mapping function between Reynolds stresses and secondary motions. Not as a means to predicting both accurately.

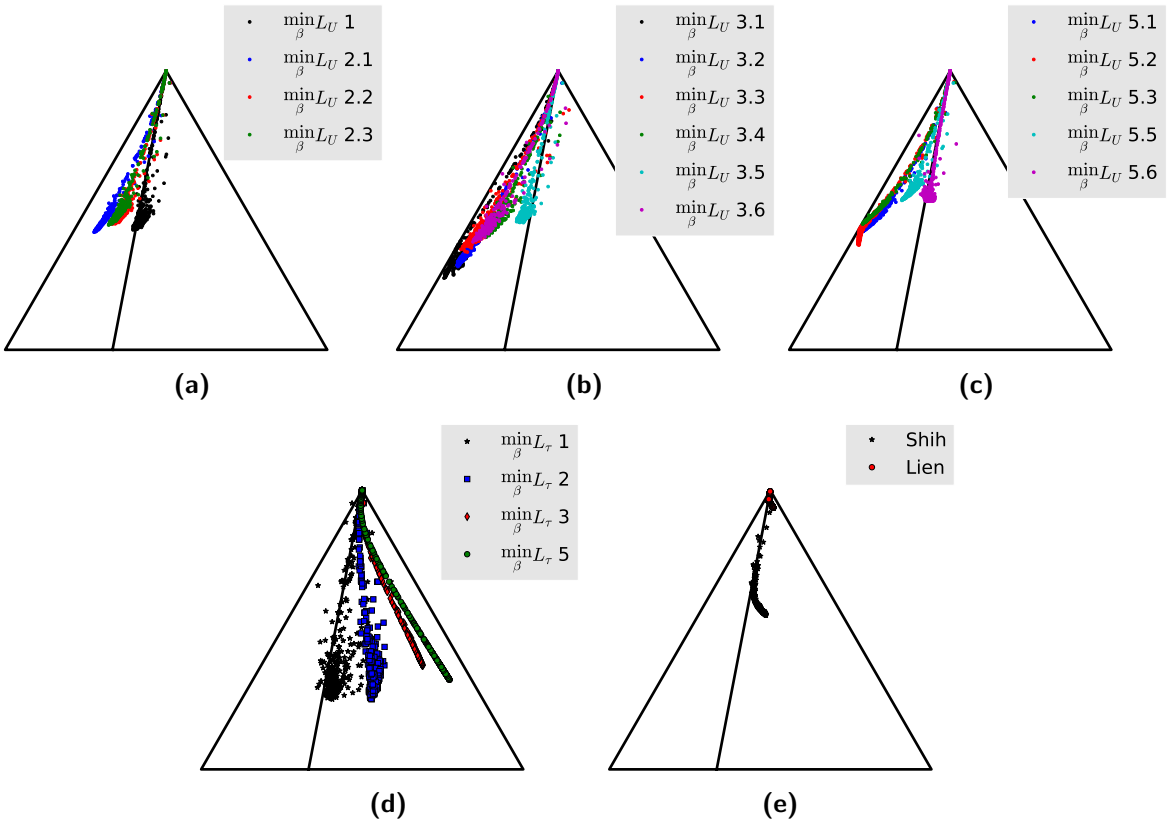

Figure 6.2: Anisotropy in random cells from different turbulence models with naming convention as specified in table 6.1.

Chapter 7

Wing-body junction prediction

The global-coefficient non-linear eddy viscosity model (NLEVM) has improved capabilities of predicting anisotropy and secondary motions on a square- and rectangular-duct. In this chapter the models derived in chapter 5 are used to predict a wing-body junction flow. The wing-body junction set-up and mesh convergence study are given in subsection 3.5.3. The set-up is similar to that used by Devenport and Simpson (1990). A 3:2 cylindrical front is joined with a NACA0020 tail at the thickest point.

The remainder of this chapter is organized as follows; the solver stability of the global-coefficient NLEVMs is evaluated in section 7.1. In section 7.2 the set-up is validated. In section 7.3 the results are presented and the findings are compared to those from Bordji and Brunet (2015) and Dandois (2014). Finally in section 7.4 the chapter is concluded with a discussion.

7.1 Solver stability

The solver stability is analyzed by convergence. All NLEVM predictions are started from a converged linear eddy viscosity model ($k-\omega$). Turbulence models are considered converged if the residuals found were stable and below 1e-6 with $\xi \geq 0.6$. All models from tables 5.1 and 5.2 and the quadratic Shih and Shih* and cubic Lien models are evaluated. The Shih* model is an additional model implemented to evaluate the wall functions. This model is quadratic as the Shih model, but contains near wall treatment as the Lien model. Table 7.1 displays the stability for all these models. Only 3 global-coefficient NLEVMs out of the 21 from tables 5.1 and 5.2 converged with the remainder breaking down.

Table 7.1: Stability and quality of prediction of wing-body junction flow using different global-coefficient NLEVM as defined in tables 5.1 and 5.2. + represents good stability, / represents medium stability and - represents instability.

Model name	Wing-body junction Stability
$\min_\beta L_U$ 1	+
$\min_\beta L_U$ 2.1	-
$\min_\beta L_U$ 2.2	-
$\min_\beta L_U$ 2.3	-
$\min_\beta L_U$ 3.1	-
$\min_\beta L_U$ 3.2	-
$\min_\beta L_U$ 3.3	-
$\min_\beta L_U$ 3.4	-
$\min_\beta L_U$ 3.5	-
$\min_\beta L_U$ 3.6	+
$\min_\beta L_U$ 5.1	-
$\min_\beta L_U$ 5.2	-
$\min_\beta L_U$ 5.3	-
$\min_\beta L_U$ 5.4	-
$\min_\beta L_U$ 5.5	-
$\min_\beta L_U$ 5.6	-

Model name	Wing-body junction Stability
$\min_\beta L_\tau$ 1	+
$\min_\beta L_\tau$ 2	-
$\min_\beta L_\tau$ 3	-
$\min_\beta L_\tau$ 5	-

Model name	Wing-body junction Stability
Shih	+
Shih*	+
Lien	+

7.2 Validation

In this section the validation of the wing-body junction is performed. The set-up is validated in 4 steps. First the boundary layer thickness and growth on the flat plate are evaluated in the symmetry plane in front of the wing. Second the stagnation points are compared. Third the pressure contours are plotted in front of the wing. And fourth the stream-wise velocity profiles are plotted at $X/T = (-0.15, -0.20, -0.25)$. These validation steps are chosen due to the existence of data from Devenport and Simpson (1990).

7.2.1 Boundary layer thickness

The boundary layer thickness is visualized with a $0.99U_x$ contour in figure 7.1. 8 different lines are plotted; the theoretical result from equation (3.15), linear $k-\omega$ turbulence model, the converged global-coefficient NLEVMs from table 7.1 and the Shih, Shih* and Lien turbulence models. The intersecting dashed lines at $z/T \approx 0.5$ and $x/T = -2.15$ represent the measurement point of Devenport and Simpson (1990). The boundary layer thickness was measured by Devenport and Simpson using only a flat plate and no wing to be 36 mm.

The theoretical result crosses exactly through the measurement point. The Linear model follows the theoretical result up to $x/T \approx -5$, where the $0.99U_x$ contour becomes vertical. This change of slope is explained from the presence of the wing which slows down the flow in

the symmetry plane. The quadratic Shih model without wall damping function over predicts the boundary layer thickness over the flat plate. Does however reach the same location for the flow deceleration in front of the wing. The Shih damped model (Shih*) overlays with the Lien cubic model. Both models under predict the boundary layer thickness on the flat plate, and predict the soonest deceleration in front of the wing.

The global-coefficient NLEVM $\min_\beta L_U$ 1 and 3.6 overlap and follow very closely the path of the linear turbulence model approaching slightly the Shih model with no damping. The global-coefficient NLEVM model $\min_\beta L_\tau$ 1 lies in between the Linear and Shih model.

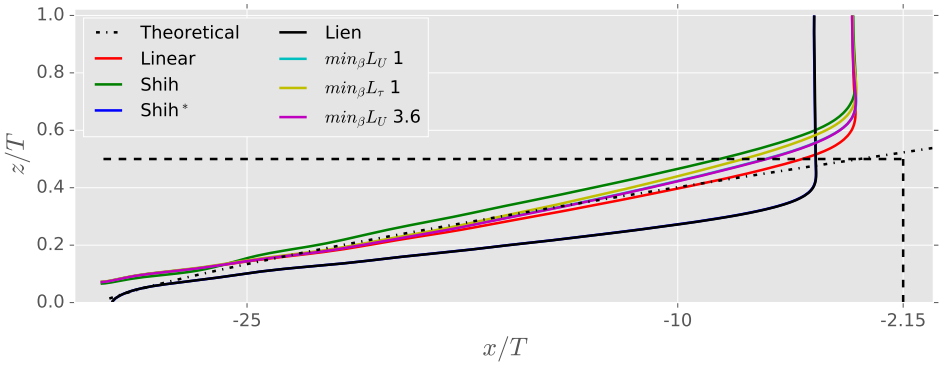

Figure 7.1: $0.99u_x$ (free-stream velocity) contour to represent boundary layer thickness on flat plate in front of wing. Dotted line (- -) represents measured flat plate (without wing) boundary layer thickness by Devenport and Simpson (1990).

7.2.2 Stagnation point

The stagnation point measured by Devenport and Simpson (1990) was found to lie between $x/T \approx -0.4$ and $x/T = -0.46$ from figure 7.2. As shown in figure 7.3 the stagnation point found from the linear, non-linear $\min_\beta L_U$ 1 and quadratic Shih turbulence models lie within that measured during the experiment. The wall damped turbulence models, quadratic Shih* and cubic Lien, on the other hand predict the stagnation point to lie closer to the wing, indicating a smaller boundary layer over the wing. The non-linear $\min_\beta L_\tau$ 1 and $\min_\beta L_U$ 3.6 turbulence models predict a stagnation point further away from the wing which corresponds to a thicker boundary layer over the wing.

7.2.3 Pressure contour

The next step in the validation consisted of comparing pressure coefficient contours between the different models with those measured by Devenport and Simpson (1990). Only the contours of the linear and Lien models are plotted in figure 7.4. The global-coefficient non-linear models and the Shih model contours present close resemblance with the linear model contours and the Shih* model contours coincide with the Lien model contours. From the contours it can be seen that neither model is perfect and differences exist between the experimental and

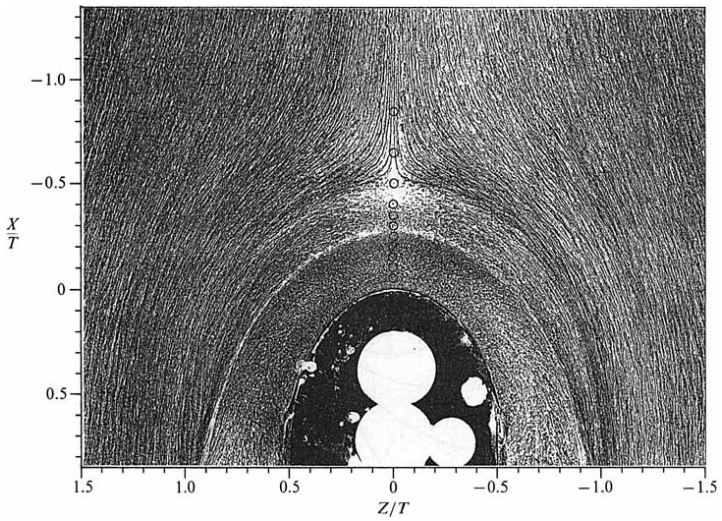

Figure 7.2: Oil-flow visualization from Devenport and Simpson (1990) on the flat plate.

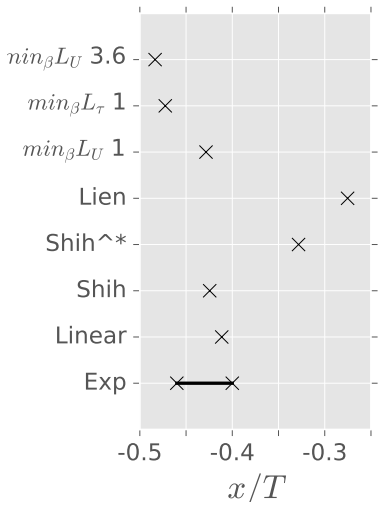

Figure 7.3: Stagnation point in front of wing.

CFD results. The linear model under predicts the C_p close to the wing. On the other hand the Lien model contour lines of $C_p = 0.1$ and $C_p = 0.2$ are predicted further from the symmetry line and wing respectively. The biggest differences between the different turbulence models used are in the near wing region. A close-up is presented in figure 7.5 to show the differences between models.

The most apparent difference noticeable in figure 7.5 is between the models using a wall damping function and those which do not. The wall damping function appears to have its largest effect approximately a quarter of the thickness from the wing where they diverge from the other models. The wall damped models exhibit a larger curvature (smaller radius) close to the wing inducing the diverging lines further away from the wing seen in figure 7.4. Comparing linear to non-linear turbulence models, the non-linear models experience more curvature close to the wing and at $C_p = 0.4$ the linear and non-linear models differ in contour-lines.

It appears that the near wall treatment has a larger effect in predicting the near wing flow than the non-linear expansion of the Boussinesq approximation.

7.2.4 Velocity profiles

The last step in the validation procedure was to compare the velocity profiles in the vicinity of the wing in the symmetry plane at $x/T = -0.25; -0.20; -0.15$. The profiles are shown in figure 7.6. From figure 7.6 it can be seen that all turbulence models represent the free stream velocity accurately, however in the near wall region differences exist. To visualize the near wall region better a log plot is generated and shown in figure 7.7. In this figure it is observed that at $z/T < 0.06$ no model follows the experimental data. Above $z/T = 0.06$ the wall damped models, Shih* and Lien, reproduce the experimental data very well, whilst the

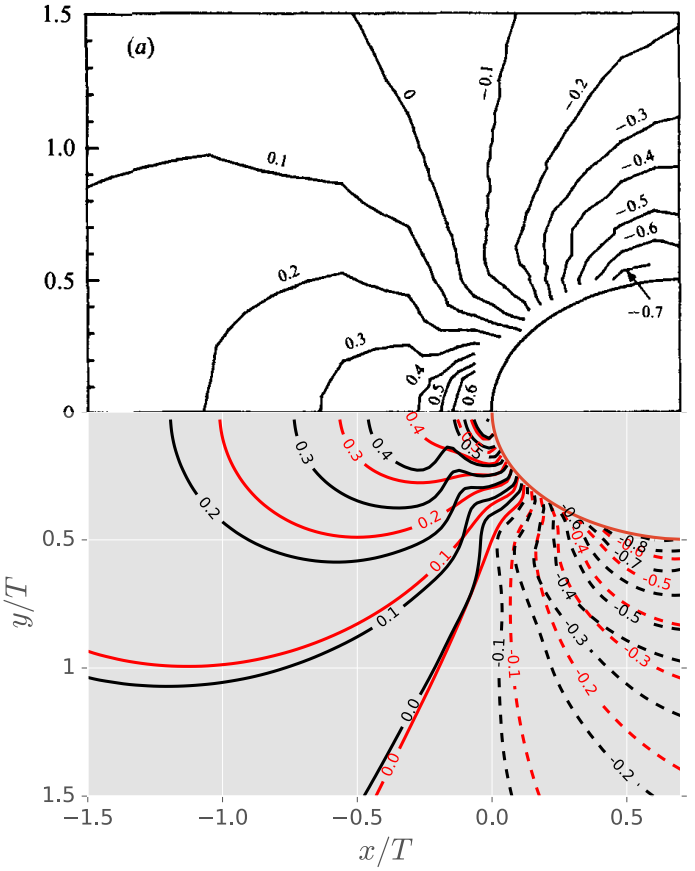

Figure 7.4: Pressure coefficient contours of linear and Lien model. Linear model in red and Lien model in black.

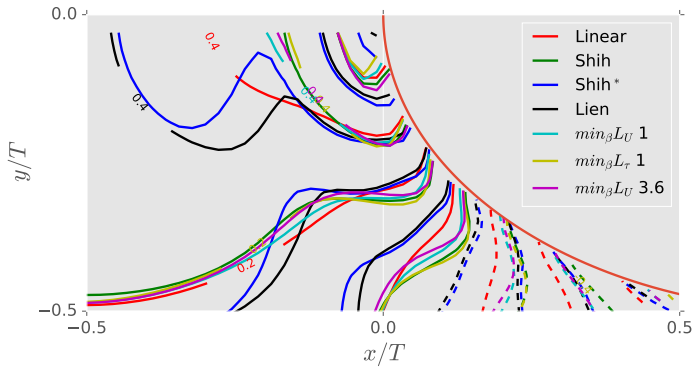

Figure 7.5: Pressure coefficient contours of linear and Lien model. Linear model in red and Lien model in black.

remaining models do not.

NLEVMs $\min_\beta L_\tau$ 1 and $\min_\beta L_U$ 1 follow very closely the lines of the linear turbulence model. These three lines can in occasions not be separated due to overlap. NLEVM $\min_\beta L_U$ 3.6 approximates better the Shih model. This result is explained from the amount of non-linear tensors considered. $\text{Min}_\beta L_\tau$ 1 and $\min_\beta L_U$ 1 consider only $T_{ij}^{(1)}$ which appears to have a minor effect whilst $\min_\beta L_U$ 3.6 uses the first three non-linear tensors similarly as the Shih model, therefore replicating the Shih model rather than the linear model.

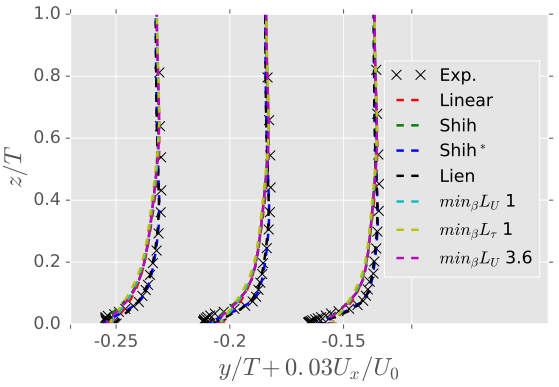

Figure 7.6: U_x/U_{ref} velocity profile in front of the wing at x/T -0.25, -0.20 and -0.15 from the wall up to 1 airfoil thickness.

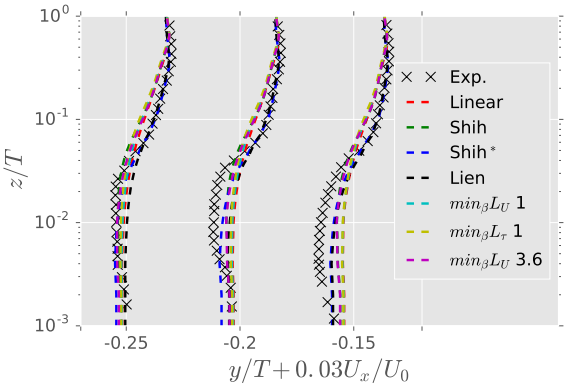

Figure 7.7: $\log(U_x/U_{ref})$ velocity profile in front of the wing at x/T -0.25, -0.20 and -0.15 from the wall up to 1 airfoil thickness.

7.2.5 Discussion

From the validation it is concluded that the test case is set-up correctly. Using a linear turbulence model the boundary layer thickness and stagnation point can be represented accurately. However the near wall results of the linear model are not good. This can be either due to the use of wall functions or insufficient mesh resolution. The models including wall damping under predict the boundary layer thickness and a wrong stagnation point. Their velocity profiles in the boundary layer however match the experimental data the best. As a result for near wall behavior the wall damped models will be taken as most correct whilst for the free stream flow the non damped models are better. This compromise also marks the difficulty of turbulence modeling where more complex models do not necessarily mean better overall predictions, and whilst some flow features might be better predicted, such as secondary motions, others get worse.

7.3 Results

It was argued in Dandois (2014) that with a quadratic constitutive relation (QCR) (Spalart, 2000), used to expand the Spalart and Allmaras (1992) (SA) turbulence model, a more realistic junction flow could be predicted. Specifically in the corner region of wing-body junction.

The standard SA model was found to over predict the corner flow separation region whilst the SA-QCR model predicted a smaller, realistic, corner flow separation. The same corner flow difference between the SA and SA-QCR models was found by Bordji et al. (2014) and Bordji and Brunet (2015) who preformed a comparative study of the SA and SA-QCR models together with a validation experiment. They investigated two regions, the junction region and corner region. In the junction region they found the SA and SA-QCR models show little difference and reproduce the experimental results similarly. Whilst in the corner region the SA model over predicted the corner flow separation with the SA-QCR model being closer to the experimental result.

Here the same regions will be investigated to asses in a qualitative manner the differences between the linear and non-linear eddy viscosity turbulence models. The leading edge region is called the junction region and the trailing edge is the corner region. Furthermore also the effect of the wall damping function is discussed. The near wall treatment was found to be one of the most important factors in the junction and corner flow prediction.

7.3.1 Junction region

The junction region is assessed by the vortices arising from two orthogonal boundary layers. These vortices are said by Gand and Choffat (2015) to determine the corner flow separation. Stronger leading edge vortices energize the flow reducing the corner flow separation. Three distinct vortices are expected: 1. the Horseshoe vortex (HSV), 2. the corner vortex and 3. the wing boundary layer vortex as shown by in figure 7.8.

1. The HSV is generated by the junction of two orthogonal boundary layers, one from the flat plate and one from the wing. This causes the flat plate boundary layer to separate and be transported over the wing. This vortex is characterized by positive vorticity in the stream-wise direction. This is different than the result found by Bordji and Brunet (2015) who characterized it by a negative vorticity due to the vortex investigated being on the other side of the wing.
2. The corner vortex is a counter-rotating vortex to the HSV. This is the vortex closest to the corner region and is argued by Bordji and Brunet (2015) to be the most important to reduce corner flow separation.
3. The wing boundary layer vortex origin is a stress induced vortex argued by Bordji and Brunet (2015) to occur due to large gradients in τ_{xy} and τ_{xz} in the wing boundary layer. This vortex is of the same orientation as the HSV but of smaller magnitude in vorticity and dimension of iso-volume.

The predicted vortices in this framework are provided as the left side of figure 7.9. The viewpoint is from below the flat plate which is therefore omitted to allow looking through. The vortices are visualized as iso-volumes using a variation of the Q criterion, $Nk = |\Omega_{ij}|/|S_{ij}|$. The colormaps on the vortices are the vorticity in stream-wise direction, and the colormap on the wing surface is the wall shear stress.

The HSV could be predicted by all turbulence models. The linear model predicted the weakest HSV and the wall damped models the strongest HSV. With the not damped non-linear models in between. For non-linear models $\min_\beta L_U$ 1 and 3.6, $\min_\beta L_\tau$ 1 and Shih the HSV appears to grow in size over the wing. This is thought to be the merger of the wing boundary layer vortex and the HSV. The wing boundary layer vortex on its own was too weak to represented by the Nk criterion for these models, but a merger between this vortex and the HSV would explain the increase in size of the HSV over the wing. In the non-linear Shih model one can also identify two incoming vortices, the HSV and one from below, which is said to be the wing boundary layer vortex that emanates at the wing boundary layer which was also captured at $Nk = 1.1$. The wall damped models represent the wing boundary layer vortex without any merging with the HSV. The Shih model also predicts a slightly longer HSV over the wing than the global-coefficient NLEVMs.

The corner vortex is visualized by all turbulence models. The linear model predicted the weakest corner vortex. This can be related to the HSV. Since the corner vortex and HSV are counter-rotating vortices, these are co-dependent and the weakest HSV as a result will go accompanied by the weakest corner vortex. The $\min_\beta L_\tau$ 1 model predicts the longest corner vortex. It has to be noted that the wall damped models experience a change sign of this vortex over the wing. This phenomena could not be explained.

In conclusion the global-coefficient NLEVMs and the Shih model showed a merger of the HSV and wing boundary layer vortex and a stronger corner vortex than the linear model. Only the wall damped models could predict clearly all 3 vortices without any merging. From this it is expected that the wall damped models show the weakest corner flow separation and the linear model the largest.

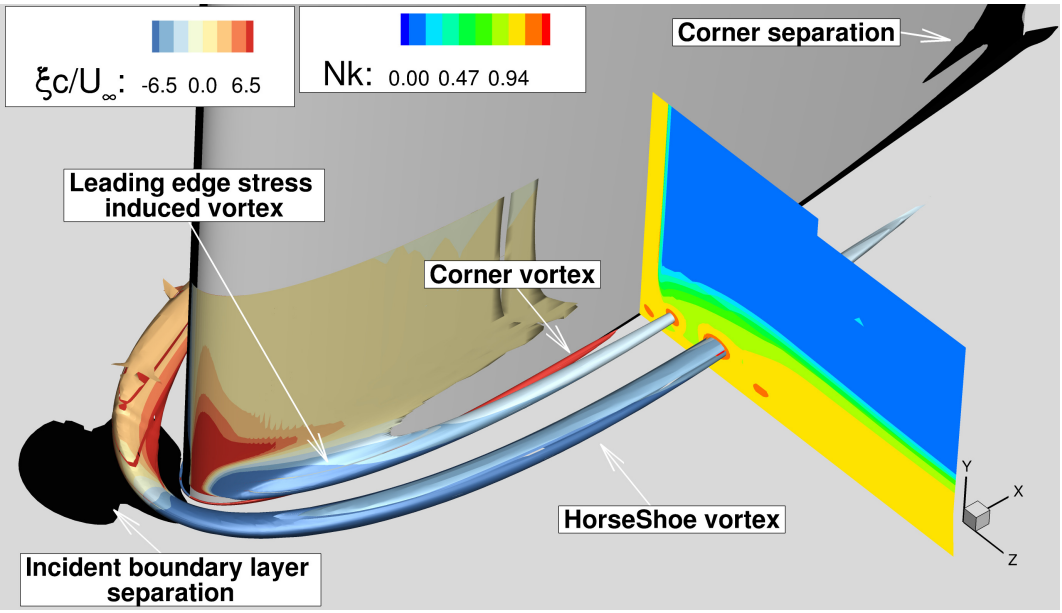

Figure 7.8: Leading edge vortices found from the SA-QCR simulation from Bordji and Brunet (2015).

7.3.2 Corner region

The corner region is shown on the right in figure 7.9. The streamlines of the wall shear stress and the strength of the wall shear stress are plotted to display the corner flow topology. From the streamline patterns the flow separation size can be analyzed with the colormap being used to analyze the strength.

All models display a corner flow separation region, the blue region with circular stream lines next to the junction. This region is largest for the linear model and smallest for the Shih* model. The size of these regions was argued to be influenced by the leading edge vortices and secondary motion prediction. The linear model showed the smallest corner vortex in figure 7.9 (a) and respectively has the largest corner flow separation in figure 7.9 (a). The global-coefficient NLEVMs showed improvements in terms of the corner vortex prediction which is said to be the originating factor in the increase in wall shear stress on the wing near the wall in the right of figures 7.9 (c-d). The corner flow separation is however not reduced considerably compared to that of the linear model. This is attributed at the lack of wing-boundary layer vortex emanating from the leading edge.

The Shih model displayed a bigger combined HSV wing boundary layer vortex in figure 7.9. This fact is used to explain a stronger energizing of the boundary layer over the wing reducing the corner flow separation. Bordji and Brunet (2015) argued that the corner vortex interacta with the corner separation. Comparing the Shih model to global-coefficient NLEVM, the Shih model predicted a weaker corner vortex, larger wing boundary layer and smaller corner flow separation. From this it would be argued that the wing boundary layer vortex is the one that interacts with the corner region to reduce corner flow separation.

The wall damped models, Shih* and Lien were the only models to display all 3 vortices. Consequently these models predict the smallest corner flow separation region. Following the finding from the previous paragraph, the corner separation region appears to be mostly influenced by the presence of the wing boundary layer vortex. This is not conclusive evidence, since the HSV is also predicted stronger than with the non-damped models, but the corner

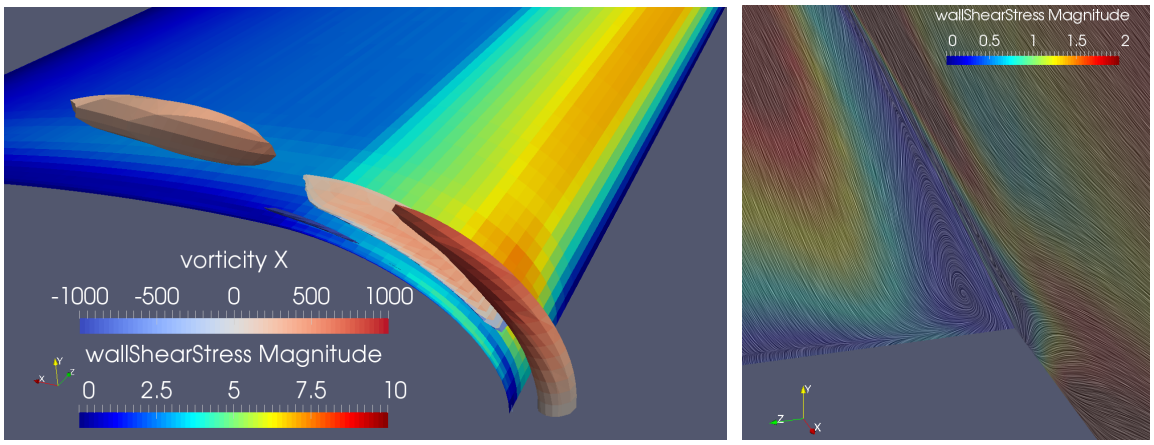

(a) Linear turbulence model.

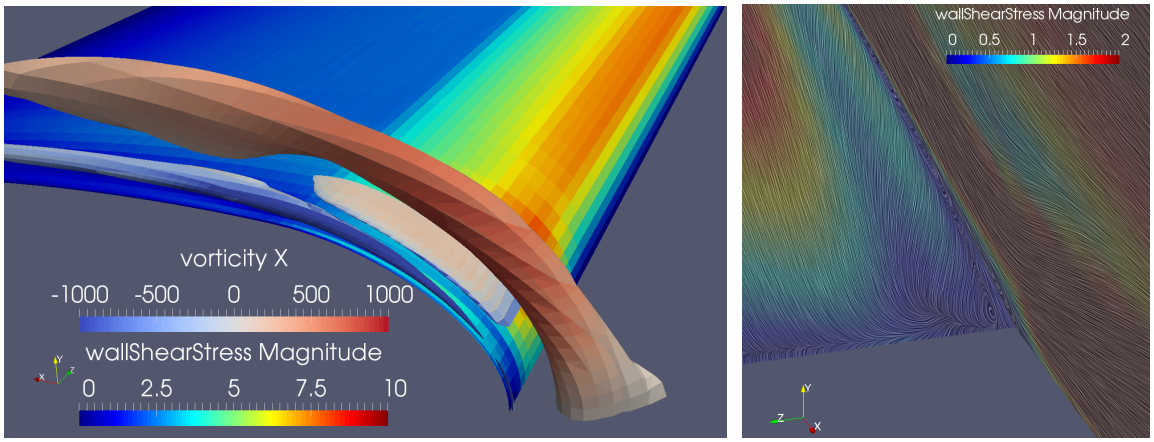

(b) $\min_\beta L_\tau$ 1 turbulence model.

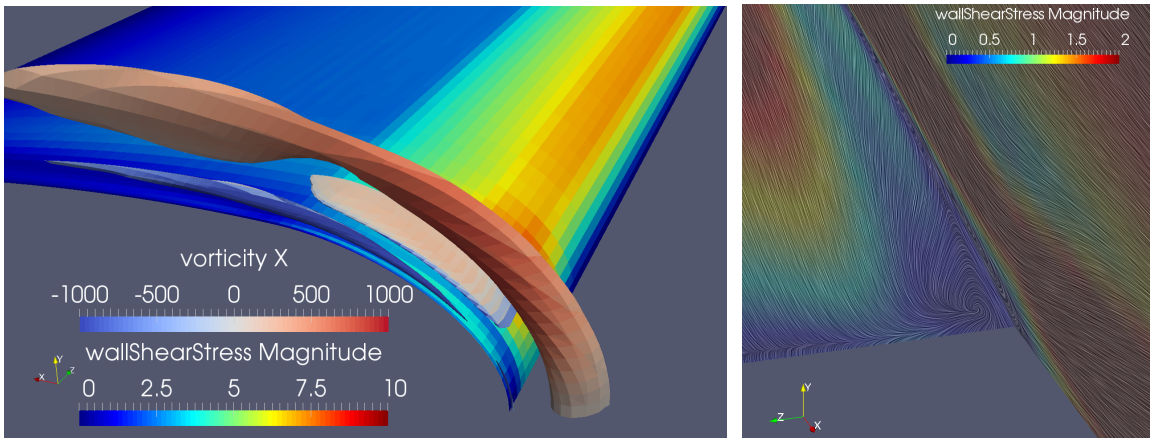

(c) $\min_\beta L_U$ 1 turbulence model.

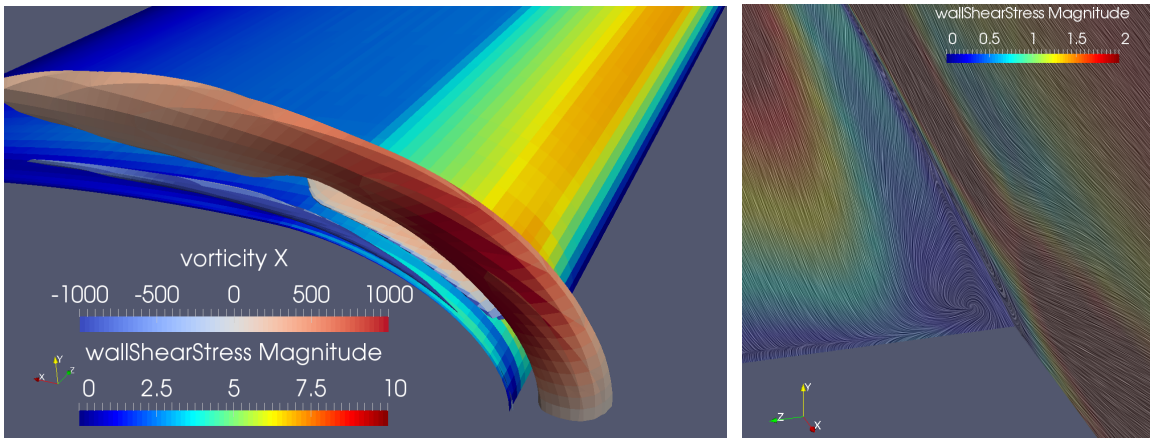

(d) $\min_\beta L_U$ 3.6 turbulence model.

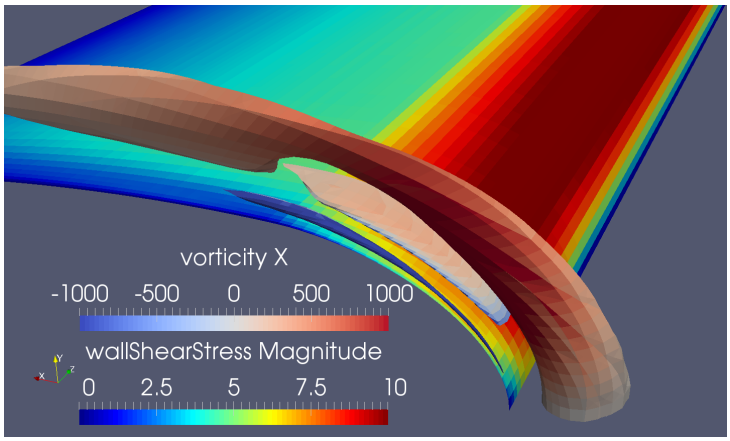

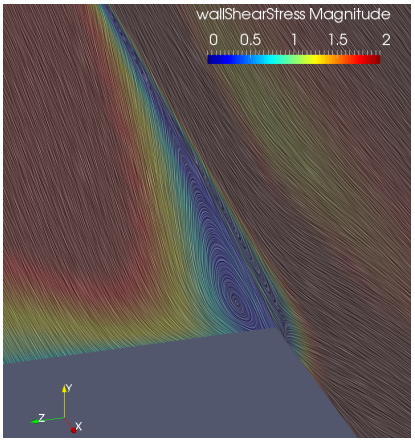

(e) Shih turbulence model.

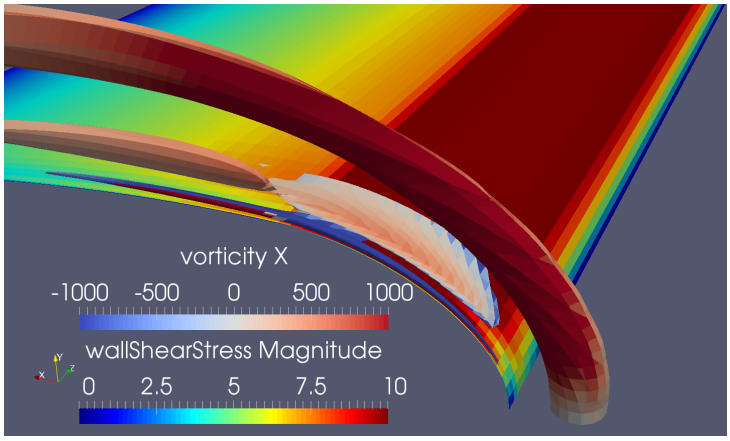

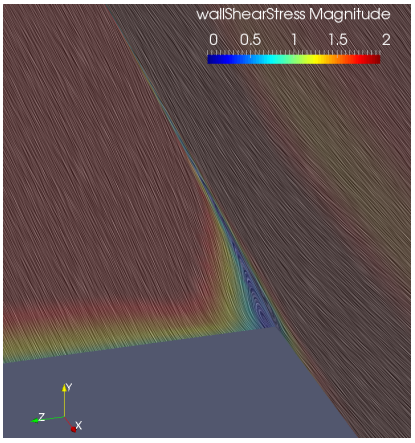

(f) Shih* turbulence model.

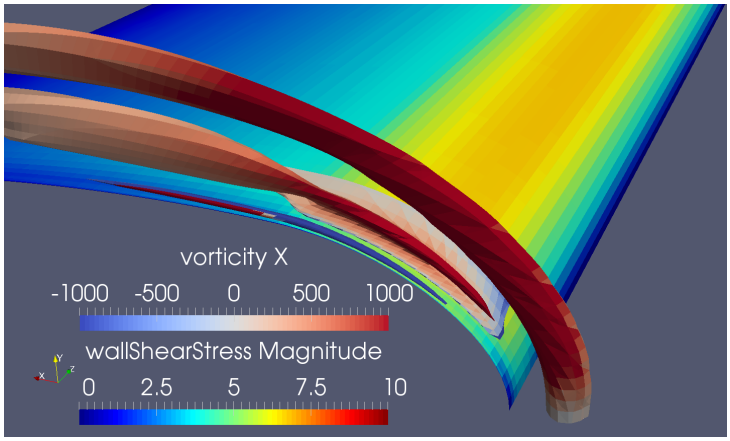

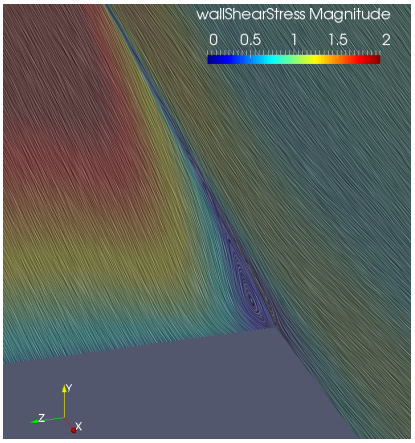

(g) Lien turbulence model.

Figure 7.9: Leading edge vortices (left) and corner flow separation (right) on the wing-body junction for different turbulence models.

vortex is predicted of a similar size. Meaning the corner vortex is likely not the driving factor to determine the corner flow separation.

7.4 Turbulence model differences

In order to assess the differences between the turbulence models the non-linear terms and wall damping functions are evaluated. The wall damping is found to be the most important addition to the turbulence model, with the non-linear terms being less relevant. The Shih model outperformed the global-coefficient NLEVMs. Having as only difference a variable C_μ, which multiplies the eddy viscosity, and local coefficients instead of a global-coefficient approach. The Shih* and Lien models outperformed the global-coefficient NLEVMs and include wall damping. The differences are addressed in 3 steps: 1) wall damping, 2) eddy viscosity (C_μ) and 3) local vs global coefficients

7.4.1 Wall damping

The wall damping was seen as the dominant effect in the prediction of the leading edge vortices and corner flow separation. The wall damping is included as two functions, f_μ and f_2 and an additional term E in the ε equation (see subsection 2.5.1). Conventionally C_μ is also considered a wall damping function, however for the purposes of this study it is considered a constitutive relationship.

The wall damping function f_μ is defined by

$$f_\mu = [1 - \exp(-A_\nu y^*)] \left[1 + \frac{2\kappa}{c_\mu^{0.75} y^*}\right]. \tag{2.42}$$

This function is designed the reduce the turbulent Reynolds stresses in the viscous and buffer layer whilst leaving the far field of the flow intact. f_μ takes a value of $f_\mu \approx 0$ near the wall and $f_\mu = 1$ far away. The behaviour of this function on a backward facing step as predicted by Basara (2006) is shown in figure 7.10. In the viscous sub-layer $f_\mu \approx 0$. In the buffer layer f_μ changes rapidly from close to 0 to $f_\mu \approx 0.9$. In the log-layer f_μ approaches 1 asymptotically. The different boundary layer regions are as described in figure E.1 as viscous sub-layer $y^+ < 4$, buffer layer $4 < y^+ < 30$, log-law layer $30 < y^+ < 200$ and outer layer $y^+ > 200$.

The second function f_2 given by equation (2.45) is used to multiply the energy dissipation. In regions of small k/ε, near the walls, $f_2 \approx 0.7$. Reducing the turbulent energy dissipation. In order to make up for the lower dissipation an additional dissipative term is added which should predict better the near wall turbulence dissipation. This term E, which is also a function of f_2 is given by equation (2.44). This term is a function of the wall distance y^* and represents an additional turbulence dissipation term near the wall. Because of f_2 the wall treatment of the Shih* and Lien models is not limited to the near wall anymore, but more intrusive into the rest of the flow field. f_2 can be 0.7 in the far field with the additional

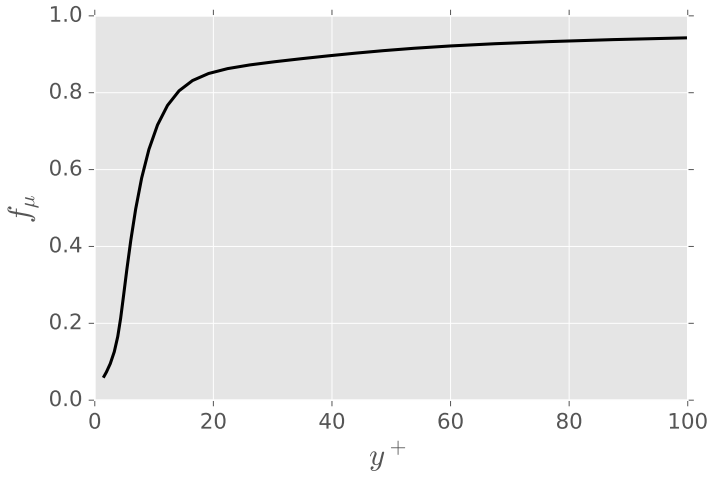

Figure 7.10: Behaviour of f_μ (2.42) on a backward facing step as found by (Basara, 2006).

term E disappearing due to very large y^* values. This could explain the prediction of a lower boundary layer thickness in figure 7.1.

The Shih* and Lien models under predicted the boundary layer growth of the flat plate. This can now be attributed to the change in turbulence dissipation in the form of f_2 and E and the damping function f_μ. It was not possible in this research to single out the importance of each of these parameters. It is expected that f_2 and E are the dominant drivers for this difference rather than f_μ. Whilst f_μ is considered to be responsible for influencing the near wall stress induced vorticity. In example by not predicting vortices in the square- and rectangular-duct flows.

7.4.2 Turbulent viscosity

The eddy viscosity for the linear and global-coefficient non-linear turbulence models is defined as $\nu_t = k/\omega$ and for the Shih model as $\nu_t = C_\mu k^2/\varepsilon$. The Shih* and Lien models use $\nu_t = f_\mu C_\mu k^2/\varepsilon$ because of which it is considered part of wall damping and due to interactions between f_μ and C_μ no effect could be singled out. The differences between the two eddy viscosities, $\nu_t = k/\omega$ and $\nu_t = C_\mu k^2/\varepsilon$, is the function C_μ and the fact that one uses ε with the other using ω dimensionally proportional to ε/k. The first is considered the important difference since the second is merely a different format for the same information. C_μ is a function of the strain and rotation rates as defined in table 2.1. Several different C_μ functions exist, depending on the model as shown in table 2.1. Here only C_μ from the Shih model is considered. C_μ generally takes its largest value ($C_\mu = 0.53$ in this flow) in regions of low strain and rotation, in example the far field. In high strain and rotation regions, such as near walls, C_μ approaches 0. In this case C_μ is small in the beginning of the wing boundary layer and large outside of it. This means that in the junction region, left in figure 7.9, $C_\mu \approx 0.01$, such that the Shih model predicts a smaller turbulent viscosity. The global-coefficient NLEVMs in

this region should then over predict the eddy viscosity compared to the Shih model. However from the pressure contours and velocity profiles of figures 5.7 and 7.5 almost no difference is appreciable between these models.

7.4.3 Global vs local coefficients

The final aspect to be discussed is the use of global vs local coefficients. The Shih and Lien models use a multiplicative function to convert the coefficients β to local coefficients. This means one value per cell. The devised function multiplies all non-linear stresses as $\tau_{\text{non-linear}}/(1000 + (k/\varepsilon|S|)^3)$. Investigating this function it is found that it is ≈ 0.001 throughout most of the flow field with the exemption of just in front of the wing, where the factor is smaller. This led to coefficients of $\beta_1 = 0.015$, $\beta_2 = 0.003$ and $\beta_3 = -0.019$ for most of the flow field. Which are considerably smaller than those from tables 5.1 and 5.2. Using these coefficients as global, without C_μ, in the non-linear $k-\omega$ model the linear model results were reproduced. From this it is concluded that the dominant effect of the Shih model compared to the linear and other non-linear models is the presence of C_μ. With the effect of global vs local coefficients being less important.

7.5 Discussion

The fuselage wing junction was presented and evaluated with different turbulence models. The results were compared to the Devenport and Simpson (1990) experiment. Qualitative comparisons were made to Bordji and Brunet (2015) and the differences between the turbulence models discussed. It was found that the non-linear expansion of the Boussinesq approximation (2.35) is not the only factor influencing improved Reynolds stress and velocity predictions. The near-wall treatment was found to be at least equally as important. Wall damped models were the only ones capable of reproducing clearly all 3 vortices and a realistic corner separation. Unfortunately no linear model with wall damping was evaluated to separate the wall damping effect from that of using a non-linear stress-strain relationship. Also no global-coefficient NLEVM with wall damping was evaluated. This would provide more insight into differences between using local or global coefficients. In conclusion the wall treatment of the turbulence model is considered crucial towards a good result and it needs to be considered with equal care as a non-linear expansion of the Boussinesq approximation.

Chapter 8

Conclusion and recommendations

A study of a global-coefficient non-linear eddy viscosity models (NLEVM) has been performed. Non-linear eddy viscosity models have been developed since the 1970's to improve upon the deficiencies of the Boussinesq approximation (1.2). The Boussinesq approximation was argued by many authors to be unable to represent anisotropy and therefore flow features such as: secondary motions, stream-line curvature or swirl (Lumley, 1970; Pope, 1975; Craft et al., 1996). Improving the anisotropy prediction Pope (1975) derived the most commonly known non-linear eddy viscosity model using a tensor polynomial expansion and repeated application of the Caley-Hamilton theorem. Since Pope many non-linear eddy viscosity models have been proposed, some of which are presented in section 2.5. These models use the Reynolds stress definition (2.35) with tensors (2.36). The arising terms β have been solved as constitutive relationships in explicit algebraic Reynolds stress models (EARSM) and coefficients as shown by the different models in table 2.1. Non of the NLEVMs known to the author has gained widespread use in industry due to a lack of consistent performance and robustness. Whilst these models predict better specific flow features, others get worse, and most industrial flows are simply shear dominated, meaning they satisfy the Boussinesq approximation's assumptions as stated in Gatski and Jongen (2000) and Slotnick et al. (2014).

The starting idea behind this research is the increasing complexity of machine learning (ML) algorithms in turbulence modelling and the little knowledge about their universality and use in industrial applications. The tuning of global-coefficients β on a square-duct was proposed. Predictions on a rectangular-duct and wing-body junction were performed evaluating the limitations of global-coefficients. On the rectangular-duct a similar flow is predicted in which secondary motions are present. In the wing-body junction a far fetched attempt to improve predictions on an industrial flow that shares similar features as the square-duct in the corner region is made.

8.1 Conclusions

8.1.1 Calibration conclusions

Two calibration procedures were evaluated, data-driven and solver-incorporated presented in chapters 4 and 5 respectively.

In the data-driven calibration the DNS results from Pinelli et al. (2010) were used as inputs for the turbulence model. This approach was unsuccessful since the mapping from velocity to Reynolds stresses and then back from Reynolds stresses to velocity was not unique. It was found that using the DNS data as input for evaluating the Reynolds stresses lead to violating the realizability constraint (Schumann, 1977). Furthermore, when implementing the calibrated model into the Reynolds-Averaged Navier-Stokes (RANS) solver, only a weak prediction of secondary motions was achieved. This concluded that the data-driven calibration was unsuited for improving the secondary motion predictions.

As an alternative to the data-driven calibration the solver-incorporated calibration was proposed. In this approach the loss functions (3.7) and (3.8) were minimized by using RANS results as inputs for the turbulence model. Since every turbulence model provides different RANS results, per combination of coefficients β a new solver run needed to be performed. Parallel Monte-Carlo (MC) simulations were performed in order to speed-up the calibration procedure. From the solver-incorporated calibration good performance in terms of secondary motions was achieved. In fact the global-coefficient NLEVMs outperformed the quadratic Shih and Lumley (1993) and cubic Lien et al. (1996) models. The Shih model predicted very weak secondary motions and the Lien model failed to predict the secondary motions due to the use of the wall damping function f_μ. This damping function was concluded to reduce the Reynolds stresses near the walls, meaning that $\tau_{ij} \approx 0$ near the walls. Then near the walls $\tau_{yy} \approx \tau_{zz} \approx 0$ such that no secondary motions are generated from equation (1.5) as explained in the Introduction. When observing the anisotropy, no NLEVM could predict well the training data. The best models in terms of secondary motion prediction showed a correction towards the axi-symmetric contraction on a barycentric map as compared to the training data which is concentrated near the 1-component turbulence (see figures D.1, 5.5 and 5.10). From this it was concluded that the global-coefficient NLEVMs serve as an unphysical map from Reynolds stresses to velocity. Given a specific turbulence model completely erroneous Reynolds stresses could be used to predict the best velocity field. This was also supported from the fact that completely different β obtained similar velocity fields.

8.1.2 Prediction conclusions

Having proven improved performance of the global-coefficient NLEVMs on the square-duct, predictions on flows different to the training data were performed. First predictions on a similar flow, rectangular-duct, followed by predictions on an industrial application, wing-body junction, were made in chapters 6 and 7.

On the rectangular-duct good performance was observed in predicting secondary motions for most models. Similar as for the square-duct, the Lien model failed to predict secondary motions. From the two loss functions L_U (3.8) was found to consistently outperform L_τ (3.7). This supports the conclusion that completely erroneous Reynolds stresses can be used to predict a better velocity field. This conclusion also highlights the limitation in calibration since for extrapolation to a different flow-case the same mapping from Reynolds stresses to velocity will occur. Then if different Reynolds stresses are predicted a flow phenomena that may not exist could be predicted. Limiting the universality of a global-coefficient NLEVM.

The wing-body junction presents a corner region similar to that in a square-duct where two plates are orthogonal to each other, being both themselves orthogonal to the free-stream velocity. At the trailing edge of a wing-body junction Dandois (2014) and Bordji et al. (2014) found that the corner flow separation was over-predicted with the SA turbulence model, but that the SA-QCR turbulence model predicted a more realistic, smaller corner flow separation. Considering that the corner region is similar to that of a square-duct, it was assumed that a NLEVM calibrated on a square-duct could be used to improve the corner flow separation prediction.

From the global-coefficient NLEVMs calibrated on the square-duct only 3 models out of 21 were stable and converged on the wing-body junction. The global-coefficient NLEVMs were calibrated to provide a better representation of the corner flow. However as soon as other phenomena occurred in the flow, such as the junction of two orthogonal boundary layers, most models broke down. This was the first big limitation encountered with the global-coefficient approach. The models were so unstable on the wing-body junction that extrapolation to it is in hindsight considered almost impossible. From the models that did converge, the improvement found in corner flow prediction was also very limited. Similar performance issues were observed by Wu et al. (2016) when injecting corrected anisotropy predictions into the RANS equations. The anisotropy prediction was improved, but the flow field prediction improvement found was small. The Shih and Lien turbulence models were able to predict a smaller corner flow separation compared to the linear $k-\omega$ turbulence model. This was attributed to the near-wall treatment.

Comparing the global-coefficient NLEVMs with the Lien model the main difference is the near-wall treatment. The Lien model reduces the impact of the Reynolds stresses near the walls with $\nu_t \approx 0$ and $\tau_{ij,\text{non-linear}} \approx 0$ near the walls. In the square- and rectangular-duct this was found to cause the secondary motions to not be predicted. On the wing-body junction this aided in representing 3 distinct leading edge vortices and the smallest corner-flow separation. This indicated that the initial assumption that improved secondary motions in a square-duct would provide improved corner flow prediction was wrong.

The difference in Reynolds number on the square-duct and wing-body junction needs to be noted. The global-coefficients where calibrated at $Re = 1,100$ whilst the wing-body junction has a Reynolds number of $Re = 132,560$. Reynolds number effects were already observed by Pinelli et al. (2010) on the Rectangular-duct on flows between $Re = 1,100$ and $Re = 3,500$. Then the difference between $Re = 1,100$ and $Re = 132,560$ may also be a reason for difficulty in stability and prediction performance.

8.1.3 Looking back at research questions

When looking back at the thesis outline, now the research questions can be answered:

- *What are the predictive capabilities of a global-coefficient eddy viscosity model?*

  Global-coefficient NLEVMs can be used to improve predictions of secondary motions in a square- and rectangular-duct. The predictions outperform not only linear eddy viscosity models but also the quadratic Shih and Lumley (1993) and cubic Lien et al. (1996) turbulence models. When extrapolating to a wing-body junction the performance is at best considered marginally improved. The corner flow separation is slightly reduced in size and the leading edge vortices are slightly bigger than with a linear model, but compared to the linear Wilcox (1994b) $k-\omega$ the quadratic Shih and Lumley and cubic Lien and Durbin turbulence models the improvement is almost negligible.

  - *Can the anisotropy be corrected?*

    Anisotropy can be corrected, however this may be futile with a global-coefficient approach. The best results in prediction were obtained from erroneous anisotropy field suggesting that a global-coefficient NLEVM serves as an unphysical map from Reynolds stresses to velocity and vice-versa rather than attempting to predict both quantities well.

  - *Can secondary motions be predicted?*

    Secondary motions can be predicted, even better than with existent NLEVMs. It is also found that the wall treatment can destroy the vorticity generation and that is why the cubic Lien et al. (1996) model fails to predict secondary motions in a square- and rectangular-duct.

  - *Can corner flow separation be reduced?*

    Corner flow separation can be reduced with NLEVMs. However it would appear that the near-wall treatment is at least equally as important as the non-linear expansion of the Boussinesq approximation.

- *What are the limitations of data driven machine learning techniques for calibration?*

  Data driven machine learning requires the existence of large amounts of high fidelity data obtained from direct numerical simulations (DNS) or large eddy simulations (LES) and the availability of clusters. Whilst improvements can be obtained with ML the extrapolation of prediction onto cases different to the training data is yet to be proven universally. In this research it was found that extrapolating to a similar flow such as the rectangular-duct ML provides good performance, but when extrapolating to a largely different flow case such as the wing-body junction stability becomes a major issue. The use of a ramping function such as described in section 3.1 can improve stability but it remains an issue. Furthermore also prediction quality deteriorates.

- *Are secondary motions the driver of corner flow separation?*

  Secondary motions are not the drivers of corner flow separation prediction. Rather the presence of leading edge vortices as argued by Perkins (1970) and Huser and Biringen (1993) are the drivers. Specifically the wing-boundary layer vortex was found to

have a large impact on corner flow separation size. However the performance of the calibrated global-coefficients might have been compromised due to Reynolds number effects rendering this conclusion as suggestive rather than evidence.

8.2 Recommendations

The global-coefficient approach for turbulence modelling has shown limited capabilities. Whilst predicting flows on the same case as it is trained on and extrapolating to very similar cases provided good improvements, extrapolating to different flow cases did not. The biggest problem of global-coefficients is considered to be the limited applicability and stability of the solver. One solution to the stability to this is the use of a ramping function. However this leaves the limited applicability intact. The Shih and Lumley (1993) and Lien et al. (1996) models convert the coefficients to local and make them a function of the turbulent kinetic energy, dissipation and strain rate in order to improve prediction and stability. However deriving new constitutive relationships would introduce an entirely new turbulence model adding to the zoo of NLEVMs. This is considered undesirable by the author since simplicity and universality should be the final goal instead of a zillion NLEVMs. Instead a re-calibration of an existing NLEVM is recommended for specific applications.

Re-calibrating a NLEVM is however not staightforwards. RANS turbulence models are inherently inaccurate since all eddies are modelled and the turbulence model itself has to predict velocity fields from potentially unrealistic Reynolds stresses. Then changing the turbulence model by using a non-linear stress-strain relationship should also require the re-calibration of the original turbulence model coefficients. Whilst global-coefficients can be used for specific applications, to derive a universal NLEVM, this author recommends to use an existing NLEVM such as the Shih model or explicit algebraic reynolds stress model and re-calibrate all coefficients instead of only those expanding the Boussinesq approximation. It was found that the Shih coefficients were 2 to 3 orders of magnitude smaller than those attained with the global-coefficients. Therefore with re-calibration considerable improvement in the Shih model for secondary motion prediction is thought to be achievable.

A re-calibration can also be used for uncertainty quantification. The coefficients can be expressed as probability density functions from which the set of highest likelihood of coefficients is chosen for prediction. Repeating this process for a variety of Reynolds numbers or training cases, the predictions from all sets of highest likelihood coefficients can be averaged providing a mean and variance for the prediction results.

In order to predict a wing-body junction the calibration cases and Reynolds number also need to be re-considered. A set of cases with different features existing in a wing-body junction could be used, i.e. including flow around a blunt object such as a square in two dimensions or a cube in three dimensions. It is also recommended to include calibration cases at higher Reynolds numbers. This means also including LES results as training data.

In terms of loss functions, the ones from this research and others should be considered.

The loss function L_U (3.8) gave a non-convex optimization problem making the selection of coefficients difficult. The loss function L_τ (3.7) would in the opinion of the author be best. However the fact that the anisotropy could not be predicted well for any test case used in this research indicated that the turbulence model is an unphysical map between Reynolds stress and velocity, rendering the hope of improving the velocity field by improving the Reynolds stresses with a global-coefficient NLEVM slim. At best one can expect the same deficiencies in flow prediction in the calibration and prediction cases to make use of this unphysical map. In order to investigate the anisotropy improvement further one can use the barycentric colormap as proposed by Emory (2014) on the flow field. This will aid in the visualization of anisotropy in different regions and thereby in the understanding of the anisotropy prediction by the turbulence model.

In conclusion RANS turbulence modelling remains a complex task and NLEVM shows only limited room for improvement. Whilst flow field predictions can be considerably improved on the training case, the anisotropy may not be predicted well. Then the reason for expanding the Boussinesq approximation is flawed. This is not to say that NLEVMs are superfluous. They have shown that when calibrated on a similar flow the anisotropy can be corrected to a minor degree, but flow features such as secondary motions are improved considerably. Then if one is only interested in the velocity prediction these models can be used for better predictions. If however good Reynolds stresses want to be predicted this author recommends to use alternative approaches. These could be more advanced RANS turbulence models such as EARSM or large eddy simulations. Furthermore, it should be attempted to use a NLEVM as a sub-grid scale in large eddy simulations. Direct numerical simulations could also be used, but their cost make them prohibitively expensive outside academia.

Approaches such as seen by Ling et al. (2016) who proposed a tensor basis neural network (TBNN) and Kaandorp (2018) who proposed a tensor basis random forest (TBRF) for anisotropy predictions are deemed incomplete. Whilst good results were obtained, the extrapolation to industrial cases remains to be seen. In fact this author believes that at the current stage that extrapolation will show similar stability and performance issues as the global-coefficient model. The TBRF requires a similar error in feature to Reynolds stress mapping in the training and prediction cases for good predictions. Furthermore the TBNN and TBRF are only capable of predicting anisotropy based on local quantities, whilst turbulence is known to be a non-local phenomenon. This dependence on local quantities can also introduce jumps in Reynolds stress prediction between cells. A possible solution to this would be to smoothen the coefficients β over the cells. However this might result in the loss of information. In summary using a TBNN or TBRF still presents many issues that requires future research for its use in industrial applications.

As a final word, there remain many possibilities in RANS turbulence modelling which can be explored. The global-coefficient approach is at an early stage of research and might become more attractive in future applications when improving upon some deficiencies encountered during this Master thesis project. I am optimistic that machine learning algorithms will dominate the future of RANS turbulence modelling and with appropriate use can be used successfully to improve turbulence modelling.

References

Abid, R., Speziale, C. G., & Thangam, S. (1991). Application of a New k-tau Model to Near Wall Turbulent Flows. In *29th aerospace schiences meeting* (pp. 0–7). doi: 10.2514/6.1991-614

Akira Yishizawa. (1984). Statistical analysis of the deviation of the Reynolds stress from its eddy-viscosity representation. *Physics of Fluids*, *27*(6), 1377–1387. Retrieved from http://dx.doi.org/10.1063/1.864780{%}5Cnhttp://scitation.aip.org/content/aip/journal/pof1/27/6?ver=pdfcov doi: 10.1017/CBO9781107415324.004

Argyropoulos, C. D., & Markatos, N. C. (2015). *Recent advances on the numerical modelling of turbulent flows* (Vol. 39) (No. 2). Retrieved from http://dx.doi.org/10.1016/j.apm.2014.07.001 doi: 10.1016/j.apm.2014.07.001

Banerjee, S., Krahl, R., Durst, F., & Zenger, C. (2007). Presentation of anisotropy properties of turbulence, invariants versus eigenvalue approaches. *Journal of Turbulence*, *8*(32), N32. Retrieved from https://www.tandfonline.com/doi/full/10.1080/14685240701506896 doi: 10.1080/14685240701506896

Basara, B. (2006). Effectiveness of turbulence models based on elliptic relaxation approach. *Heat and Mass Transfer*, *012403*, 1–21. doi: 10.1088/0169-5983/41/1/012403

Bordji, M., & Brunet, V. (2015). Investigation of a Nonlinear Reynolds-Averaged Navier-Stokes Closure for Corner Flows. *AIAA Journal*. doi: 10.2514/1.J054313

Bordji, M., Gand, F., Brunet, V., & Deck, S. (2014). Comparative study of linear and non-linear RANS models for corner flows. In *32nd aiaa applied aerodynamics conference* (pp. 1–14). Retrieved from http://arc.aiaa.org/doi/abs/10.2514/6.2014-2690 doi: 10.2514/6.2014-2690

Boussinesq, J. (1877). Essai sur la theorie des eaux courantes. *Memoires presentes par divers savants a l'Academie des Sciences de l'Institut National de France*, *XXIII*, 1–770.

Celik, I. B. (1999). *Introductory Turbulence Modeling* (Tech. Rep. No. December).

Craft, T. J., Launder, B. E., & Suga, K. (1996). Development and application of a cubic eddy-viscosity model of turbulence. *International Journal of Heat and Fluid Flow*, *17*(2), 108–115. Retrieved from http://ac.els-cdn.com/0142727X95000796/1-s2.0-0142727X95000796-main.pdf?{_}tid=198b96ae-0d43-11e7-a8ad-00000aacb361{&}acdnat=

1489996930{_}310499c2d4986c4acafe50b454502ac1http://ac.els-cdn.com/0142727X95000796/1-s2.0-0142727X95000796-main.pdf?{_}tid=0ec21ada-0335 doi: 10.1016/0142-727X(95)00079-6

Craft, T. J., Launder, B. E., & Suga, K. (1997). Prediction of turbulent transitional phenomena with a nonlinear eddy-viscosity model. *International Journal of Heat and Fluid Flow*, *18*(1), 15–28. Retrieved from http://www.sciencedirect.com/science/article/pii/S0142727X96001452 doi: 10.1016/S0142-727X(96)00145-2

Dandois, J. (2014). Improvement of Corner Flow Prediction Using the Quadratic Constitutive Relation. *AIAA Journal*, *52*(12), 2795–2806. Retrieved from http://arc.aiaa.org/doi/10.2514/1.J052976 doi: 10.2514/1.J052976

Davidson, P. A. P. A. (2004). *Turbulence : an introduction for scientists and engineers*. Oxford University Press.

Demirdzic, I. (1982). *A finite volume method for computation of fluid flow in complex geometries* (Ph.D. Thesis). University of London.

Devenport, W. J., & Simpson, R. L. (1990). Time-dependent and time-averaged turbulence structure near the nose of a wing-body junction. *Journal of Fluid Mechanics*, *210*.

Duraisamy, B. K., & Durbin, P. A. (2014). Transition modeling using data driven approaches. In *Proceedings of the summer program 2014* (pp. 427–434). Retrieved from https://web.stanford.edu/group/ctr/Summer/SP14/09{_}Large-eddy{_}simulation/07{_}duraisamy.pdf

Edeling, W. N., Cinnella, P., & Dwight, R. P. (2014). Predictive RANS simulations via bayesian model-scenario averaging. *Journal of Computational Physics*, *275*, 65–91. Retrieved from http://dx.doi.org/10.1016/j.jcp.2014.06.052 doi: 10.1016/j.jcp.2014.06.052

Ehrhard, J., & Moussiopoulos, N. (2000). On a new nonlinear turbulence model for simulating flows around building-shaped structures. *Journal of Wind Engineering and Industrial Aerodynamics*, *88*(1), 91–99. Retrieved from http://ac.els-cdn.com/S016761050000026X/1-s2.0-S016761050000026X-main.pdf?{_}tid=1addbfda-0322-11e7-8ab9-00000aacb362{&}acdnat=1488883247{_}bfdf9ea6a73bccf26386fff99c98a7f2 doi: 10.1016/S0167-6105(00)00026-X

Emory, M. (2014). *Estimating Model-Form Uncertainty in Reynolds-Averaged Navier-Stokes closures* (Unpublished doctoral dissertation).

Gand, F., & Choffat, A. (2015). Experimental Study of the Corner Flow Separation on a Simplified Junction. *AIAA Journal*, 1–9. doi: 10.2514/1.J053771

Gatski, T. B., & Jongen, T. (2000). Nonlinear eddy viscocity and algebraic stress models for solving complex turbulent flows. *Progress in Aerospace SciencesAerospace Sciences*, *36*, 655–682.

Gavrilakis, S. (1992). Numerical simulation of low-Reynolds-number turbulent flow through a straight square duct. *Journal of Fluid Mechanics*, *244*, 101–129. doi: 10.1017/S0022112092002982

Ge, X., Arolla, S., & Durbin, P. (2014). A Bypass Transition Model Based on the Intermittency Function. *Flow, Turbulence and Combustion*, 37–61. doi: 10.1007/s10494-014-9533-9

Harris, G. V., Graham, A. J., & Corrsin, S. (1977). Further experiments in nearly homogeneous shear flow. *J. Fluid Mech.*, *81*(8), 657–687. Retrieved from http://www.journals.cambridge.org/abstract{_}S0022112070000538http://

link.aip.org/link/PHFLE6/v9/i11/p3472/s1{&}Agg=doi{%}5Cnhttp://www.journals.cambridge.org/abstract{_}S0022112077002286{%}5Cnhttp://arxiv.org/abs/0902.0893{%}5Cnhttp://linkinghub.elsevier.com/retrie doi: 10.1017/S0022112077002286

Huser, A., & Biringen, S. (1993). Direct numerical simulation of turbulent flow in a square duct. *Journal of Fluid Mechanics*, *257*, 65–95.

Kaandorp, M. (2018). *Machine Learning for Data-Driven RANS Turbulence Modelling* (Unpublished doctoral dissertation).

Kawahara, G., & Kamada, E. (2000). Vortical structures in the corner region ofa turbulent square-duct flow. *JSME International Journal Series B Fluids and Thermal Energy*, *66*(643), 89–97.

Launder, B. E. (1972). Two-Equation of Laminarization With a. *Heat and Mass Transfer*, *15*, 301–314.

Launder, B. E., & Spalding, D. B. (1974). The numerical computation of turbulent flows. *Computer Methods in Applied Mechanics and Engineering*, *3*(2), 269–289. doi: 10.1016/0045-7825(74)90029-2

Lien, F., Chen, W., & Leschziner, M. (1996). Low-Reynolds-Number Eddy-Viscosity Modelling Based on Non-Linear Stress-Strain/Vorticity Relations. In *Engineering turbulence modelling and experiments* (pp. 91–100). Elsevier. Retrieved from http://linkinghub.elsevier.com/retrieve/pii/B9780444824639500150 doi: 10.1016/B978-0-444-82463-9.50015-0

Lien, F., & Durbin, P. (1996). Non-linear k-v$ˆ2$ modeling with application to high-lift. Retrieved from https://web.stanford.edu/group/ctr/ctrsp96/lien

Ling, J., Kurzawski, A., & Templeton, J. (2016, nov). Reynolds averaged turbulence modelling using deep neural networks with embedded invariance. *Journal of Fluid Mechanics*, *807*, 155–166. Retrieved from http://www.journals.cambridge.org/abstract{_}S0022112016006157 doi: 10.1017/jfm.2016.615

Ling, J., & Templeton, J. (2015). Evaluation of machine learning algorithms for prediction of regions of high Reynolds averaged Navier Stokes uncertainty. *Physics of Fluids*, *27*(8). Retrieved from http://dx.doi.org/10.1063/1.4927765http://aip.scitation.org/toc/phf/27/8 doi: 10.1063/1.4927765

Lumley, J. L. (1970). Toward a turbulent constitutive relation. *J . Fluid Mech*, *41*(2), 413–434. Retrieved from https://www-cambridge-org.tudelft.idm.oclc.org/core/services/aop-cambridge-core/content/view/DABCF56E1BA25231945B8B96F30CADE5/S0022112070000678a.pdf/toward{_}a{_}turbulent{_}constitutive{_}relation.pdf doi: 10.1017/S0022112070000678

Nallasamy, M. (1987). Turbulence models and their applications to the prediction of internal flows: a review. , *15*(2), 151–194.

Nisizima, S., & Yoshizawa, A. (1987). Turbulent channel and Couette flows using an anisotropic k-epsilon model. *AIAA Journal*, *25*(3), 414–420. Retrieved from http://arc.aiaa.org.proxygw.wrlc.org/doi/abs/10.2514/3.9639{%}5Cnhttp://arc.aiaa.org/doi/10.2514/3.9639{%}5Cnhttp://sci-hub.cc/10.2514/3.9639 doi: 10.2514/3.9639

Perkins, H. (1970). The formation of streamwise vorticity in turbulent flow. *Journal of Fluid Mechanics*, *44*, 721–740.

Pinelli, A., Uhlmann, M., Sekimoto, A., & Kawahara, G. (2010). Reynolds num-

ber dependence of mean flow structure in square duct turbulence. *Journal of Fluid Mechanics*, *653*, 537. Retrieved from http://www.journals.cambridge.org/abstract{_}S0022112010001849 doi: 10.1017/S0022112010001849

Pope, S. B. (1975). A more general effective-viscosity hypothesis. *Journal of Fluid Mechanics*, *72*(2), 331–340. doi: 10.1017/S0022112075003382

Prandtl, L. (1925). Bericht uber untersuchungen zur ausgebildeten turbulenz. *Journal of Applied Mathematics and Mechanics / Zeitschrift für Angewandte Mathematik und Mechanik*, *5*, 136–139. Retrieved from https://ci.nii.ac.jp/naid/10025613914/en/

Rubinstein, R., & Barton, J. M. (1990). Nonlinear Reynolds stress models and the renormalization group. *Physics of Fluids A: Fluid Dynamics*, *2*(8), 1472–1476. Retrieved from http://scitation.aip.org/content/aip/journal/pofa/2/8/10.1063/1.857595 doi: 10.1063/1.857595

Saltelli, A. (2002). Making best use of model evaluations to compute sensitivity indices. *Computer Physics Communications*, *145*, 280–297.

Saltelli, A., Annoni, P., Azzini, I., Campolongo, F., Ratto, M., & Tarantola, S. (2010). Variance based sensitivity analysis of model output. Design and estimator for the total sensitivity index. *Computer Physics Communications*, *181*(2), 259–270. Retrieved from http://dx.doi.org/10.1016/j.cpc.2009.09.018 doi: 10.1016/j.cpc.2009.09.018

Schmitt, F. G. (2008). About Boussinesq's turbulent viscosity hypothesis: historical remarks and a direct evaluation of its validity.

Schumann, U. (1977). Realizability of Reynoldsstress turbulence models. , *20*, 721–725. doi: 10.1063/1.861942

Shih, T. H., & Lumley, J. L. (1993). Remarks on turbulent constitutive relations. *Mathematical and Computer Modelling*, *18*(2), 9–16. Retrieved from http://ac.els-cdn.com/089571779390002G/1-s2.0-089571779390002G-main.pdf?{_}tid=b020355a-25a5-11e7-880f-00000aacb360{&}acdnat=1492678101{_}a765bf2266ac2c161d7b8fe64782e1d4 doi: 10.1016/0895-7177(93)90002-G

Slotnick, J., Khodadoust, A., Beach, H., Alonso, J., Darmofal, D., Gropp, W., ... Mavriplis, D. (2014). CFD Vision 2030 Study: A Path to Revolutionary Computational Aerosciences. (March 2014).

Sobol, I. M. (2001). Global sensitivity indices for nonlinear mathematical models and their Monte Carlo estimates. *Mathematics and Computers in Simulation*, *55*, 271–280.

Spalart, P. R. (2000). Strategies for turbulence modelling and simulations. *International Journal of Heat and Fluid Flow*, *21*(3), 252–263. doi: 10.1016/S0142-727X(00)00007-2

Spalart, P. R., & Allmaras, S. (1992). A one-equation turbulence model for aerodynamic flows. In *30th aerospace sciences meeting and exhibit* (Vol. 1, pp. 5–21). Retrieved from http://arc.aiaa.org/doi/10.2514/6.1992-439 doi: 10.2514/6.1992-439

Speziale, C. G., & Ngo, T. (1987). Numerical Solution of Turbulent Flow Past a Backward Facing Step Using a Non-Linear k-epsilon model. *NASA contractor report*. Retrieved from https://ntrs.nasa.gov/archive/nasa/casi.ntrs.nasa.gov/19880005807.pdf

Tracey, B. (2015). *Machine Learning for Model Unvertainties in Turbulence Models and Monte-Carlo Integral Approximation* (Unpublished doctoral dissertation). Stanford University.

von Karman, T. (1931). *Mechanical Simulitude and Turbulence: Reprint from Nachrichten von der Gesellshaft der Wissenshaften zu Gottingen* (Tech. Rep.). National Advisory

Comittee for Aeronautics.

Wallin, S., & Johansson, A. V. (2000). An explicit algebraic Reynolds stress model for incompressible and compressible turbulent flows. *Journal of Fluid Mechanics*, *403*, 89–132. Retrieved from http://www.journals.cambridge.org/abstract{_}S0022112099007004 doi: 10.1017/S0022112099007004

Wang, J.-X., Wu, J., Ling, J., Iaccarino, G., & Xiao, H. (2017). A Comprehensive Physics-Informed Machine Learning Framework for Predictive Turbulence Modeling. , 1–35. Retrieved from http://arxiv.org/abs/1701.07102

Wang, J.-X., Wu, J.-L., & Xiao, H. (2017). A Physics Informed Machine Learning Approach for Reconstructing Reynolds Stress Modeling Discrepancies Based on DNS Data. *Physical Review Fluids*. Retrieved from http://arxiv.org/abs/1606.07987{%}0Ahttp://dx.doi.org/10.1103/PhysRevFluids.2.034603 doi: 10.1103/PhysRevFluids.2.034603

Weatheritt, J., & Sandberg, R. (2016). A novel evolutionary algorithm applied to algebraic modifications of the RANS stress-strain relationship. *Journal of Computational Physics*, *325*(August), 22–37. Retrieved from http://dx.doi.org/10.1016/j.jcp.2016.08.015 doi: 10.1016/j.jcp.2016.08.015

White, F. M. (1991). *Viscous Fluid Flow*. McGraw-Hill. Retrieved from https://books.google.nl/books?id=G6IeAQAAIAAJ

Wilcox, D. C. (1994a). *Turbulence Modeling for CFD*. DCW Industries, Incorporated. Retrieved from https://books.google.nl/books?id=VwlRAAAAMAAJ

Wilcox, D. C. (1994b). *Turbulence Modeling for CFD* (No. 2). Retrieved from http://inis.jinr.ru/sl/vol2/Physics/œμμ/Wilcox,{_}Turbulence{_}Modeling{_}for{_}CFD,1994/contents.pdf doi: 10.1017/CBO9781107415324.004

Wu, J.-l., Wang, J.-x., & Xiao, H. (2016). Quantifying Model Form Uncertainty in RANS Simulation of Wing-Body Junction Flow. , 1–31.

Xiao, H., Wu, J. L., Wang, J. X., Sun, R., & Roy, C. J. (2016). Quantifying and reducing model-form uncertainties in Reynolds-averaged Navier-Stokes simulations: A data-driven, physics-informed Bayesian approach. *Journal of Computational Physics*, *324*, 115–136. Retrieved from https://arxiv.org/pdf/1508.06315.pdf doi: 10.1016/j.jcp.2016.07.038

Yakhot, V., & Orszag, S. A. (1986). Renormalization-group analysis of turbulence. *Physical Review Letters*, *57*(14), 1722–1724. Retrieved from http://mathunion.org/ICM/ICM1986.2/Main/icm1986.2.1395.1399.ocr.pdf doi: 10.1103/PhysRevLett.57.1722

Appendix A

Derivation of Reynolds-Averaged Navier-Stokes and turbulence model transport equations

In this appendix the RANS equations and transport equations from the turbulence models in chapter 2 are derived. First Reynolds time averaging is explained in section A.1. In section A.2 the RANS equations for incompressible flow are derived. The derivation of the Reynolds stresses is preformed in section A.3. The transport equations for the turbulent kinetic energy and dissipation are derived in sections A.4 and A.5.

A.1 Reynolds time averaging

For the derivation of the Reynolds-Averaged Navier-Stokes (RANS) equations Reynolds time averaging is performed. The main idea behind time averaging is to express any variable $\phi(x,t)$ as a sum of a mean and a perturbation

$$\phi(x,t) = \bar{\phi}(x) + \phi'(x,t). \tag{A.1}$$

For stationary turbulence the average of $\phi(x,t)$ is defined by

$$\overline{\phi(x,t)} = \lim_{\tau\to\infty} \frac{1}{\tau} \int_t^{t+\tau} \phi(x,t)dt = \bar{\phi}(x). \tag{A.2}$$

With the above definition in mind, the following rules apply:

1. The time average of a constant a is constant

$$\bar{a} = a. \tag{A.3}$$

2. The time average of an average is the average it self

$$\bar{\bar{a}} = \bar{a}. \tag{A.4}$$

3. The time average of a perturbation is zero

$$\bar{a'} = 0. \tag{A.5}$$

4. The time average of a sum is the sum of time averages

$$\overline{\sum_i a_i} = \sum_i \bar{a}_i. \tag{A.6}$$

5. The time average of a product between mean and perturbation is zero

$$\overline{\bar{a}a'} = \bar{a}\overline{a'} = 0. \tag{A.7}$$

6. The time average of a product is the product of time averages plus a time average of the perturbations

$$\overline{\prod_i a_i} = \prod_i \bar{a}_i + \prod_i \bar{a}_i'. \tag{A.8}$$

It is important for this rule to not forget the disturbances since

$$\begin{aligned} \overline{ab} &= \overline{(\bar{a} + a')\left(\bar{b} + b'\right)} \\ &= \overline{\bar{a}\bar{b} + \bar{a}b' + a'\bar{b} + a'b'} \\ &= \overline{\bar{a}\bar{b}} + \overline{\bar{a}b'} + \overline{a'\bar{b}} + \overline{a'b'} \\ &= \bar{a}\bar{b} + \overline{a'b'}. \end{aligned} \tag{A.9}$$

which is different to $\bar{a}\bar{b}$.

7. The time average of a spatial derivative is the spatial derivative of the average

$$\overline{\frac{\partial \phi}{\partial x}} = \overline{\frac{\partial \bar{\phi} + \phi'}{\partial x}} = \overline{\frac{\partial \bar{\phi}}{\partial x}} + \overline{\frac{\partial \phi'}{\partial x}} = \frac{\partial \bar{\phi}}{\partial x} + \frac{\partial \overline{\phi'}}{\partial x} = \frac{\partial \bar{\phi}}{\partial x}. \tag{A.10}$$

8. The time average of a time derivative is zero for stationary turbulence. For non-stationary turbulence the time average of a time derivative is the time derivative of the average similar as with the spatial derivative

$$\overline{\frac{\partial \phi}{\partial t}} = \frac{\partial \bar{\phi}}{\partial t}. \tag{A.11}$$

For the following derivation the chain rule will often be applied and is therefore reviewed here. The chain rule states that the derivative of the product of two variables is equals to the first variable times the derivative of the second plus the second variable times the derivative of the first. This is defined mathematically as

$$\frac{\partial ab}{\partial x} = a\frac{\partial b}{\partial x} + b\frac{\partial a}{\partial x}. \tag{A.12}$$

A.2 Derivation of Reynolds-Averaged Navier-Stokes equations

The Reynolds-Averaged Navier-Stokes (RANS) equations are obtained from splitting the flow field into a mean and perturbation as explained in section A.1 and applying time averaging. The incompressible Navier-Stokes (NS) equations for an incompressible Newtonian fluid are given by the continuity and momentum equation as

$$\frac{\partial u_i}{\partial x_i} = 0, \tag{2.3}$$

$$\frac{\partial u_i}{\partial t} + u_j \frac{\partial u_i}{\partial x_j} = -\frac{1}{\rho}\frac{\partial p}{\partial x_i} + \frac{\partial}{\partial x_j}\left[\nu\left(\frac{\partial u_i}{\partial x_j} + \frac{\partial u_j}{\partial x_i}\right)\right]. \tag{2.4}$$

Applying Reynolds time averaging to the continuity equation results in

$$\frac{\partial\left(\bar{u}_i + u_i'\right)}{\partial x_i} = 0 \Rightarrow \frac{\partial \bar{u}_i}{\partial x_i} = 0 \tag{A.13}$$

and the momentum equation in

$$\overline{\frac{\partial\left(\bar{u}_i + u_i'\right)}{\partial t}} + \overline{\left(\bar{u}_j + u_j'\right)\frac{\partial\left(\bar{u}_i + u_i'\right)}{\partial x_j}} = -\overline{\frac{1}{\rho}\frac{\partial p}{\partial x_i}} + \overline{\frac{\partial}{\partial x_j}\left[\nu\left(\frac{\partial\left(\bar{u}_i + u_i'\right)}{\partial x_j} + \frac{\partial\left(\bar{u}_j + u_j'\right)}{\partial x_i}\right)\right]}. \tag{A.14}$$

Using the 7 rules as described in section A.1, the momentum equation can be simplified. First (A.14) is rewritten to $\partial(\bar{u}_i + u_i') = \partial\bar{u}_i + \partial u_i'$ using rule 4. Then the terms $\overline{u_i'}$ can be eliminated. Rearranging yields the RANS momentum equation

$$\frac{\partial \bar{u}_i}{\partial t} + \bar{u}_j\frac{\partial \bar{u}_i}{\partial x_j} = -\frac{1}{\rho}\frac{\partial \bar{p}}{\partial x_j} + \frac{\partial}{\partial x_j}\left[\nu\left(\frac{\partial \bar{u}_i}{\partial x_j} + \frac{\partial \bar{u}_j}{\partial x_i}\right) - u_i'u_j'\right]. \tag{A.15}$$

This equation looks very similar to the original NS momentum equation with an additional term $\overline{u_i'u_j'}$. This term is commonly known as the Reynolds stresses $\tau_{ij} = -\overline{u_i'u_j'}$.

A.3 Derivation of the Reynolds stress equation

From the RANS momentum equation the Reynolds stresses have been defined as $\tau_{ij} = -\overline{u_i'u_j'}$. To find an equation for the Reynolds stresses let us consider the components of the momentum equation and multiply them by the perturbation u_i' and u_j' finding

$$u_j'\frac{\partial u_i}{\partial t} + u_j'u_k\frac{\partial u_i}{\partial x_k} = -u_j'\frac{1}{\rho}\frac{\partial p}{\partial x_i} + u_j'\frac{\partial}{\partial x_k}\left[\nu\frac{\partial u_i}{\partial x_k}\right], \tag{A.16}$$

$$u_i'\frac{\partial u_j}{\partial t} + u_i'u_k\frac{\partial u_j}{\partial x_k} = -u_i'\frac{1}{\rho}\frac{\partial p}{\partial x_j} + u_i'\frac{\partial}{\partial x_k}\left[\nu\frac{\partial u_j}{\partial x_k}\right]. \tag{A.17}$$

Now consider the time average of the sum of (A.16) and (A.17)

$$\overbrace{u'_j\frac{\partial u_i}{\partial t}+u'_i\frac{\partial u_j}{\partial t}}^{\text{(I)}}+\overbrace{u'_j u_k\frac{\partial u_i}{\partial x_k}+u'_i u_k\frac{\partial u_j}{\partial x_k}}^{\text{(II)}}=-\overbrace{u'_j\frac{1}{\rho}\frac{\partial p}{\partial x_i}-u'_i\frac{1}{\rho}\frac{\partial p}{\partial x_j}}^{\text{(III)}}+\overbrace{u'_j\frac{\partial}{\partial x_k}\left[\nu\frac{\partial u_i}{\partial x_k}\right]+u'_i\frac{\partial}{\partial x_k}\left[\nu\frac{\partial u_j}{\partial x_k}\right]}^{\text{(IV)}}. \tag{A.18}$$

The next step is introducing the RANS approximation $u=\bar{u}+u'$. Since this would lead to an unreadable equation it will be analyzed term by term. Term (I) is the unsteady term, term (II) is the convective term, term (III) is the pressure term and term (IV) are the viscous stresses.

A.3.1 Term (I)

The unsteady term is derived from splitting the flow field into a mean and perturbation $u=\bar{u}+u'$

$$\text{(I)}=\overline{\mathrm{u}'_\mathrm{j}\frac{\partial\bar{\mathrm{u}}_\mathrm{i}+\mathrm{u}'_\mathrm{i}}{\partial \mathrm{t}}+\mathrm{u}'_\mathrm{i}\frac{\partial\bar{\mathrm{u}}_\mathrm{j}+\mathrm{u}'_\mathrm{j}}{\partial \mathrm{t}}}. \tag{A.19}$$

Using the rules described in section A.1 the components can be split up and the first and third term eliminated

$$\begin{aligned}\text{(I)}=&\overline{u'_j\frac{\partial\bar{u}_i}{\partial t}}+\overline{u'_j\frac{\partial u'_i}{\partial t}}+\overline{u'_i\frac{\partial\bar{u}_j}{\partial t}}+\overline{u'_i\frac{\partial u'_j}{\partial t}}\\=&\overline{u'_j\frac{\partial u'_i}{\partial t}}+\overline{u'_i\frac{\partial u'_j}{\partial t}}.\end{aligned} \tag{A.20}$$

Finally applying the chain rule $u_j\partial u_i+u_i\partial u_j=\partial\left(u_iu_j\right)$, term (I) is given by

$$\text{(I)}=\frac{\partial\overline{\mathrm{u}'_\mathrm{i}\mathrm{u}'_\mathrm{j}}}{\partial \mathrm{t}}. \tag{A.21}$$

A.3.2 Term (II)

Using the same approach as for term (I), the convective term is found as

$$\begin{aligned}\text{(II)}=&\overline{u'_j\left(\bar{u}_k+u'_k\right)\frac{\partial\left(\bar{u}_i+u'_i\right)}{\partial x_k}+u'_i\left(\bar{u}_k+u'_k\right)\frac{\partial\left(\bar{u}_j+u'_j\right)}{\partial x_k}}\\=&\overline{u'_j\bar{u}_k\frac{\partial\bar{u}_i}{\partial x_k}}+\overline{u'_j\bar{u}_k\frac{\partial u'_i}{\partial x_k}}+\overline{u'_ju'_k\frac{\partial\bar{u}_i}{\partial x_k}}+\overline{u'_ju'_k\frac{\partial u'_i}{\partial x_k}}\\&+\overline{u'_i\bar{u}_k\frac{\partial\bar{u}_j}{\partial x_k}}+\overline{u'_i\bar{u}_k\frac{\partial u'_j}{\partial x_k}}+\overline{u'_iu'_k\frac{\partial\bar{u}_j}{\partial x_k}}+\overline{u'_iu'_k\frac{\partial u'_j}{\partial x_k}}.\end{aligned} \tag{A.22}$$

This expression can be simplified using the time averaging rules given in section A.1. The first and fifth terms are zero due to u'. The second and sixth terms and the fourth and eight terms can be combined using the chain rule. This yields

$$(\text{II}) = \bar{u}_k \frac{\partial\left(\overline{u_i' u_j'}\right)}{\partial x_k} + \overline{u_j' u_k'} \frac{\partial \bar{u}_i}{\partial x_k} + \overline{u_i' u_k'} \frac{\partial \bar{u}_j}{\partial x_k} + \overline{u_k' \frac{\partial\left(u_i' u_j'\right)}{\partial x_k}}. \tag{A.23}$$

We can express the chain rule as

$$\overline{\frac{\partial\left(u_i' u_j' u_k'\right)}{\partial x_k}} = \overline{u_k' \frac{\partial\left(u_i' u_j'\right)}{\partial x_k}} + \overline{u_i' u_j' \frac{\partial\left(u_k'\right)}{\partial x_k}} \tag{A.24}$$

were the last term is zero to write

$$(\text{II}) = \bar{u}_k \frac{\partial\left(\overline{u_i' u_j'}\right)}{\partial x_k} + \overline{u_j' u_k'} \frac{\partial \bar{u}_i}{\partial x_k} + \overline{u_i' u_k'} \frac{\partial \bar{u}_j}{\partial x_k} + \frac{\partial\left(\overline{u_i' u_j' u_k'}\right)}{\partial x_k}. \tag{A.25}$$

A.3.3 Term (III)

The pressure term is derived by splitting the pressure into a mean and perturbation as $p = \bar{p} + p'$ and considering the time average as

$$(\text{III}) = -\overline{\mathrm{u_j'} \frac{1}{\rho} \frac{\partial \mathrm{\bar{p}}}{\partial \mathrm{x_i}}} - \overline{\mathrm{u_j'} \frac{1}{\rho} \frac{\partial \mathrm{p'}}{\partial \mathrm{x_i}}} - \overline{\mathrm{u_i'} \frac{1}{\rho} \frac{\partial \mathrm{\bar{p}}}{\partial \mathrm{x_j}}} - \overline{\mathrm{u_i'} \frac{1}{\rho} \frac{\partial \mathrm{p'}}{\partial \mathrm{x_j}}}. \tag{A.26}$$

The $\partial\bar{p}$ terms are zero and using the chain rule the second and fourth term can be rewritten. Rearranging the expression and using the Kronecker delta results in

$$\begin{aligned}(\text{III}) &= \overline{p' \frac{1}{\rho} \frac{\partial u_j'}{\partial x_i}} - \overline{\frac{1}{\rho} \frac{\partial\left(p' u_j'\right)}{\partial x_i}} + \overline{p' \frac{1}{\rho} \frac{\partial u_i'}{\partial x_j}} - \overline{\frac{1}{\rho} \frac{\partial\left(p' u_i'\right)}{\partial x_j}} \\ &= \overline{\frac{1}{\rho} p' \left[\frac{\partial u_i'}{\partial x_j} + \frac{\partial u_j'}{\partial x_i}\right]} - \frac{1}{\rho} \frac{\partial}{\partial x_k} \left[\overline{p' u_i'} \delta_{jk} + \overline{p' u_j'} \delta_{ik}\right].\end{aligned} \tag{A.27}$$

A.3.4 Term (IV)

In the viscous term the velocities u are replaced by the mean plus perturbation. The new terms are solved similarly as for the unsteady term, reducing term (IV) to

$$(\text{IV}) = \overline{u_j' \frac{\partial}{\partial x_k} \left[\nu \frac{\partial u_i'}{\partial x_k}\right]} + \overline{u_i' \frac{\partial}{\partial x_k} \left[\nu \frac{\partial u_j'}{\partial x_k}\right]} \tag{A.28}$$

and applying the chain rule as

$$u_j' \frac{\partial}{\partial x_k} \left[\nu \frac{\partial u_i'}{\partial x_k}\right] = \frac{\partial}{\partial x_k} \left[\nu u_j' \frac{\partial u_i'}{\partial x_k}\right] - \left[\nu \frac{\partial u_i'}{\partial x_k}\right] \frac{\partial u_j'}{\partial x_k}, \tag{A.29}$$

$$u_i' \frac{\partial}{\partial x_k} \left[\nu \frac{\partial u_j'}{\partial x_k}\right] = \frac{\partial}{\partial x_k} \left[\nu u_i' \frac{\partial u_j'}{\partial x_k}\right] - \left[\nu \frac{\partial u_j'}{\partial x_k}\right] \frac{\partial u_i'}{\partial x_k} \tag{A.30}$$

yields

$$(\text{IV}) = \overline{\frac{\partial}{\partial x_k}\left[\nu\left(u'_j\frac{\partial u'_i}{\partial x_k} + u'_i\frac{\partial u'_j}{\partial x_k}\right)\right]} - \overline{2\nu\frac{\partial u'_j}{\partial x_k}\frac{\partial u'_i}{\partial x_k}}. \tag{A.31}$$

Applying the chain rule again results in

$$(\text{IV}) = \overline{\frac{\partial}{\partial x_k}\left[\nu\frac{\partial u'_i u'_j}{\partial x_k}\right]} - \overline{2\nu\frac{\partial u'_j}{\partial x_k}\frac{\partial u'_i}{\partial x_k}}. \tag{A.32}$$

A.3.5 Reynolds stress transport equation

The Reynolds stress transport equation is the combination of the terms (I)-(IV) and some rearranging. The combination of terms (I)-(IV) gives

$$\begin{aligned}
(\text{I}): \quad & \frac{\partial\overline{u'_i u'_j}}{\partial t} + \\
(\text{II}): \quad & \bar{u}_k\frac{\partial\left(\overline{u'_i u'_j}\right)}{\partial x_k} + \overline{u'_j u'_k}\frac{\partial\bar{u}_i}{\partial x_k} + \overline{u'_i u'_k}\frac{\partial\bar{u}_j}{\partial x_k} + \frac{\partial\left(\overline{u'_i u'_j u'_k}\right)}{\partial x_k} = \\
(\text{III}): \quad & \overline{\frac{1}{\rho}p'\left[\frac{\partial u'_i}{\partial x_j} + \frac{\partial u'_j}{\partial x_i}\right]} - \frac{1}{\rho}\frac{\partial}{\partial x_k}\left[\overline{p'u'_i}\delta_{jk} + \overline{p'u'_j}\delta_{ik}\right] + \\
(\text{IV}): \quad & \overline{\frac{\partial}{\partial x_k}\left[\nu\frac{\partial u'_i u'_j}{\partial x_k}\right]} - \overline{2\nu\frac{\partial u'_j}{\partial x_k}\frac{\partial u'_i}{\partial x_k}}.
\end{aligned} \tag{A.33}$$

Multiplying this expression by the density $-\rho$, using τ_{ij} for $-\overline{u'_i u'_j}$ and rearranging yields the Reynolds stress transport equation

$$\rho\frac{\partial\tau_{ij}}{\partial t} + \rho\bar{u}_k\frac{\partial\tau_{ij}}{\partial x_k} = -\rho\tau_{jk}\frac{\partial\bar{u}_i}{\partial x_k} - \rho\tau_{ik}\frac{\partial\bar{u}_j}{\partial x_k} + \varepsilon_{ij} - \Pi_{ij} + \frac{\partial}{\partial x_k}\left[\nu\overline{\frac{\partial\rho\tau_{ij}}{\partial x_k}} + C_{ijk}\right] \tag{A.34}$$

where the terms on the left hand side represent the rate of change and transport by convection respectively. The first two terms on the right hand side are the stress production terms, ε_{ij} is the dissipation, Π_{ij} is the pressure-strain interaction and C_{ijk} represents the molecular and turbulent diffusion. The additional terms ε_{ij}, Π_{ij} and C_{ijk} are expressed as

$$\varepsilon_{ij} = \overline{2\mu\frac{\partial u'_j}{\partial x_k}\frac{\partial u'_i}{\partial x_k}}, \tag{A.35}$$

$$\Pi_{ij} = \overline{p'\left[\frac{\partial u'_i}{\partial x_j} + \frac{\partial u'_j}{\partial x_i}\right]}, \tag{A.36}$$

and

$$C_{ijk} = \overline{p'u'_i}\delta_{jk} + \overline{p'u'_j}\delta_{ik} + \overline{u'_i u'_j u'_k}. \tag{A.37}$$

The Reynolds stress equation (A.34) introduces several higher order terms, whose modeling is the basis of finding closure equations.

A.4 Derivation of turbulent-kinetic-energy equation

Let the turbulent kinetic energy be defined as the mean-squared of the velocity perturbations as

$$k = \frac{1}{2}\left(\overline{u'^2} + \overline{v'^2} + \overline{w'^2}\right) \tag{A.38}$$

and the Reynolds stresses as

$$\tau_{ij} = -\overline{u_i' u_j'}. \tag{A.39}$$

Observing the above definitions a relation between turbulent kinetic energy and Reynolds stresses can be made. Let the turbulent kinetic energy be defined as the trace of the Reynolds stresses

$$k = \mathrm{tr}(\tau_{ij}). \tag{A.40}$$

Then by taking the trace of the Reynolds stress equation (A.34) the turbulent kinetic energy transport equation can be found. Expressing the Reynolds stress equation in terms of $\overline{u_i' u_j'}$ and dividing it by ρ yields

$$\begin{aligned} -\frac{\partial \overline{u_i' u_j'}}{\partial t} - \bar{u}_k \frac{\partial \overline{u_i' u_j'}}{\partial x_k} =& \overline{u_j' u_k'} \frac{\partial \bar{u}_i}{\partial x_k} + \overline{u_i' u_k'} \frac{\partial \bar{u}_j}{\partial x_k} + \overline{2\nu \frac{\partial u_j'}{\partial x_k} \frac{\partial u_i'}{\partial x_k}} \\ & - \frac{1}{\rho} \overline{p' \left[\frac{\partial u_i'}{\partial x_j} + \frac{\partial u_j'}{\partial x_i} \right]} + \frac{\partial}{\partial x_k} \left[-\nu \frac{\partial \overline{u_i' u_j'}}{\partial x_k} + \overline{p' u_i'} \delta_{jk} + \overline{p' u_j'} \delta_{ik} + \overline{u_i' u_j' u_k'} \right]. \end{aligned} \tag{A.41}$$

In order to obtain the trace, in Einstein summation convention the indices need to be equal. This is obtained by setting $j = i$ and $k = j$

$$\begin{aligned} -\frac{\partial \overline{u_i' u_i'}}{\partial t} - \bar{u}_j \frac{\partial \overline{u_i' u_i'}}{\partial x_j} =& 2\overline{u_i' u_j'} \frac{\partial \bar{u}_i}{\partial x_j} + \overline{2\nu \frac{\partial u_i'}{\partial x_j} \frac{\partial u_i'}{\partial x_j}} \\ & - \frac{1}{\rho} \overline{p' \left[\frac{\partial u_i'}{\partial x_i} + \frac{\partial u_i'}{\partial x_i} \right]} + \frac{\partial}{\partial x_j} \left[-\nu \frac{\partial \overline{u_i' u_i'}}{\partial x_j} + 2\overline{p' u_i'} \delta_{ij} + \overline{u_i' u_i' u_j'} \right]. \end{aligned} \tag{A.42}$$

From incompressibility condition $\partial_x u_i'$ the third term on the right hand side disappears. The Kronecker delta can be eliminated since only $i = j$ is relevant when $\delta_{i=j} = 1$. Then multiplying this expression by $-1/2$ and summing up the xx, yy and zz components gives

$$\frac{\partial k}{\partial t} + \bar{u}_j \frac{\partial k}{\partial x_j} = -\overline{u_i' u_j'} \frac{\partial \bar{u}_i}{\partial x_j} - \overline{\nu \frac{\partial u_i'}{\partial x_j} \frac{\partial u_i'}{\partial x_j}} - \frac{\partial}{\partial x_j} \left[-\nu \frac{\partial k}{\partial x_j} + \overline{p' u_j'} + \frac{1}{2} \overline{u_i' u_i' u_j'} \right]. \tag{A.43}$$

In this equation $\overline{u_i' u_j'}$ can be expressed in terms of τ_{ij} and the second term on the right hand side as the dissipation

$$\varepsilon_{ij} = \overline{\nu \frac{\partial u_i'}{\partial x_j} \frac{\partial u_i'}{\partial x_j}}. \tag{A.44}$$

Then the turbulent kinetic energy transport equation becomes

$$\frac{\partial k}{\partial t} + \bar{u}_j \frac{\partial k}{\partial x_j} = \tau_{ij} \frac{\partial \bar{u}_i}{\partial x_j} - \varepsilon_{ij} - \frac{\partial}{\partial x_j} \left[-\nu \frac{\partial k}{\partial x_j} + \overline{p' u_j'} + \frac{1}{2} \overline{u_i' u_i' u_j'} \right]. \tag{A.45}$$

A.5 Derivation of the dissipation rate equation

The dissipation rate equation is derived starting at the incompressible NS momentum equation for Newtonian fluid and substituting in the mean plus perturbation for the flow field components as

$$\begin{aligned}\frac{\partial\left(\bar{u}_i+u_i'\right)}{\partial t}&+\left(\bar{u}_j+u_j'\right)\frac{\partial\left(\bar{u}_i+u_i'\right)}{\partial x_j}\\&=-\frac{1}{\rho}\frac{\partial\left(\bar{p}+p'\right)}{\partial x_i}+\frac{\partial}{\partial x_j}\left[\nu\left(\frac{\partial\left(\bar{u}_i+u_i'\right)}{\partial x_j}+\frac{\partial\left(\bar{u}_j+u_j'\right)}{\partial x_i}\right)\right]\end{aligned} \tag{A.46}$$

$$\begin{aligned}\frac{\partial\bar{u}_i}{\partial t}&+\frac{\partial u_i'}{\partial t}+\bar{u}_j\frac{\partial\bar{u}_i}{\partial x_j}+\bar{u}_j\frac{\partial u_i'}{\partial x_j}+u_j'\frac{\partial\bar{u}_i}{\partial x_j}+u_j'\frac{\partial u_i'}{\partial x_j}\\&=-\frac{1}{\rho}\frac{\partial\bar{p}}{\partial x_i}-\frac{1}{\rho}\frac{\partial p'}{\partial x_i}+\frac{\partial}{\partial x_j}\left[\nu\left(\frac{\partial\bar{u}_i}{\partial x_j}+\frac{\partial u_i'}{\partial x_j}+\frac{\partial\bar{u}_j}{\partial x_i}+\frac{\partial u_j'}{\partial x_i}\right)\right].\end{aligned} \tag{A.47}$$

Taking the time average results in

$$\frac{\partial\bar{u}_i}{\partial t}+\bar{u}_j\frac{\partial\bar{u}_i}{\partial x_j}+\overline{u_j'\frac{\partial u_i'}{\partial x_j}}=-\frac{1}{\rho}\frac{\partial\bar{p}}{\partial x_i}+\frac{\partial}{\partial x_j}\left[\nu\left(\frac{\partial\bar{u}_i}{\partial x_j}+\frac{\partial\bar{u}_j}{\partial x_i}\right)\right]. \tag{A.48}$$

Taking the difference between the previous two relations yields

$$\frac{\partial u_i'}{\partial t}+\bar{u}_j\frac{\partial u_i'}{\partial x_j}+u_j'\frac{\partial\bar{u}_i}{\partial x_j}+u_j'\frac{\partial u_i'}{\partial x_j}-\overline{u_j'\frac{\partial u_i'}{\partial x_j}}=-\frac{1}{\rho}\frac{\partial p'}{\partial x_i}+\frac{\partial}{\partial x_j}\left[\nu\left(\frac{\partial u_i'}{\partial x_j}+\frac{\partial u_j'}{\partial x_i}\right)\right]. \tag{A.49}$$

From continuity for incompressible flow $\partial u_j/\partial x_j=0$ and using the chain rule

$$\overline{u_j'\frac{\partial u_i'}{\partial x_j}}=\overline{\frac{\partial u_i'u_j'}{\partial x_j}}-\underbrace{\overline{u_i'\frac{\partial u_j'}{\partial x_j}}}_{=0} \tag{A.50}$$

the dissipation equation can be rewritten to

$$\frac{\partial u_i'}{\partial t}+\bar{u}_j\frac{\partial u_i'}{\partial x_j}+u_j'\frac{\partial\bar{u}_i}{\partial x_j}+u_j'\frac{\partial u_i'}{\partial x_j}=-\frac{1}{\rho}\frac{\partial p'}{\partial x_i}+\frac{\partial}{\partial x_j}\left[\nu\left(\frac{\partial u_i'}{\partial x_j}+\frac{\partial u_j'}{\partial x_i}\right)\right]+\frac{\partial\overline{u_i'u_j'}}{\partial x_j}. \tag{A.51}$$

Since epsilon is given as in equation (A.44) as $\varepsilon_{ik}=\overline{\nu\frac{\partial u_i'}{\partial x_k}\frac{\partial u_i'}{\partial x_k}}$ the above expression is differentiated with respect to x_k and multiplied by $\partial u_i'/\partial x_k$. Following the derivation from (Celik, 1999) (this is the only derivation I could not replicate myself) term by term the expression

becomes

$$(I) = \overline{\frac{\partial u_i'}{\partial x_k}\frac{\partial}{\partial x_k}\left(\frac{\partial u_i'}{\partial t}\right)} = \frac{\partial}{\partial t}\left[\frac{1}{2}\overline{\left(\frac{\partial u_i'}{\partial x_k}\right)^2}\right] \tag{A.52}$$

$$(II) = \overline{\frac{\partial u_i'}{\partial x_k}\frac{\partial}{\partial x_k}\left(\bar{u}_j\frac{\partial u_i'}{\partial x_j}\right)} = \frac{\partial \bar{u}_j}{\partial x_k}\overline{\frac{\partial u_i'}{\partial x_k}\frac{\partial u_i'}{\partial x_j}} + \bar{u}_j\overline{\frac{\partial}{\partial x_j}\left[\frac{1}{2}\left(\frac{\partial u_i'}{\partial x_k}\right)^2\right]} \tag{A.53}$$

$$(III) = \overline{\frac{\partial u_i'}{\partial x_k}\frac{\partial}{\partial x_k}\left(u_j'\frac{\partial \bar{u}_i}{\partial x_j}\right)} = \frac{\partial \bar{u}_i}{\partial x_j}\overline{\frac{\partial u_i'}{\partial x_k}\frac{\partial u_j'}{\partial x_k}} + \overline{u_j'\frac{\partial u_i'}{\partial x_k}\frac{\partial^2 \bar{u}_i}{\partial x_k x_j}} \tag{A.54}$$

$$(IV) = \overline{\frac{\partial u_i'}{\partial x_k}\frac{\partial}{\partial x_k}\left(u_j'\frac{\partial u_i'}{\partial x_j}\right)} = \overline{\frac{\partial u_i'}{\partial x_k}\frac{\partial u_j'}{\partial x_k}\frac{\partial u_i'}{\partial x_j}} + \overline{u_j'\frac{\partial}{\partial x_j}\left[\frac{1}{2}\left(\frac{\partial u_i'}{\partial x_k}\right)^2\right]} \tag{A.55}$$

$$(V) = \overline{\frac{\partial u_i'}{\partial x_k}\frac{\partial}{\partial x_k}\left(\frac{1}{\rho}\frac{\partial p'}{\partial x_i}\right)} = -\overline{\frac{1}{\rho}\frac{\partial u_i'}{\partial x_k}\frac{\partial^2 p'}{\partial x_k x_i}} \tag{A.56}$$

$$(VI) = \overline{\frac{\partial u_i'}{\partial x_k}\frac{\partial}{\partial x_k}\left(\frac{\partial}{\partial x_j}\left[\nu\left(\frac{\partial u_i'}{\partial x_j}+\frac{\partial u_j'}{\partial x_i}\right)\right]\right)} = \overline{\frac{\partial u_i'}{\partial x_k}\left(\frac{\partial}{\partial x_j}\left[\nu\left(\frac{\partial^2 u_i'}{\partial x_j x_k}+\frac{\partial^2 u_j'}{\partial x_i x_k}\right)\right]\right)} \tag{A.57}$$

$$(VII) = \overline{\frac{\partial u_i'}{\partial x_k}\frac{\partial}{\partial x_k}\left(\frac{\partial \overline{u_i'u_j'}}{\partial x_j}\right)} = 0. \tag{A.58}$$

The final expression becomes

$$\begin{aligned}
&\frac{\partial}{\partial t}\left[\frac{1}{2}\overline{\left(\frac{\partial u_i'}{\partial x_k}\right)^2}\right] + \frac{\partial \bar{u}_j}{\partial x_k}\overline{\frac{\partial u_i'}{\partial x_k}\frac{\partial u_i'}{\partial x_j}} + \bar{u}_j\overline{\frac{\partial}{\partial x_j}\left[\frac{1}{2}\left(\frac{\partial u_i'}{\partial x_k}\right)^2\right]} \\
+\frac{\partial \bar{u}_i}{\partial x_j}\overline{\frac{\partial u_i'}{\partial x_k}\frac{\partial u_j'}{\partial x_k}} + \overline{u_j'\frac{\partial u_i'}{\partial x_k}\frac{\partial^2 \bar{u}_i}{\partial x_k x_j}} + \overline{\frac{\partial u_j'}{\partial x_k}\frac{\partial u_i'}{\partial x_j}} + \overline{u_j'\frac{\partial u_i'}{\partial x_k}\frac{\partial}{\partial x_j}\left[\frac{1}{2}\left(\frac{\partial u_i'}{\partial x_k}\right)^2\right]} \\
&= -\overline{\frac{1}{\rho}\frac{\partial u_i'}{\partial x_k}\frac{\partial^2 p'}{\partial x_k x_i}} + \overline{\frac{\partial u_i'}{\partial x_k}\left(\frac{\partial}{\partial x_j}\left[\nu\left(\frac{\partial^2 u_i'}{\partial x_j x_k}+\frac{\partial^2 u_j'}{\partial x_i x_k}\right)\right]\right)}.
\end{aligned} \tag{A.59}$$

Multiplying this by 2ν, letting $\varepsilon_{ik} = \overline{\nu\frac{\partial u_i'}{\partial x_k}\frac{\partial u_i'}{\partial x_k}}$ and rearranging the turbulent energy dissipation equation becomes

$$\begin{aligned}
&\frac{\partial \varepsilon}{\partial t} + \bar{u}_j\frac{\partial \varepsilon}{\partial x_j} = -2\frac{\nu}{\rho}\overline{\frac{\partial u_i'}{\partial x_k}\frac{\partial^2 p'}{\partial x_k \partial x_i}} + \nu\frac{\partial}{\partial x_j}\left(\frac{\partial \varepsilon}{\partial x_j}\right) \\
&-\overline{u_j'\frac{\partial}{\partial x_j}\left(\nu\frac{\partial u_i'}{\partial x_k}\frac{\partial u_i'}{\partial x_k}\right)} - 2\nu^2\left(\frac{\partial^2 u_i'}{\partial x_j \partial x_k}\right)^2 - 2\nu\overline{\frac{\partial u_i'}{\partial x_k}\frac{\partial u_j'}{\partial x_k}\frac{\partial \bar{u}_i}{\partial x_k}} \\
&-2\nu\overline{\frac{\partial u_i'}{\partial x_k}\frac{\partial u_i'}{\partial x_j}\frac{\partial \bar{u}_i}{\partial x_k}} - 2\nu\overline{u_j'\frac{\partial u_i'}{\partial x_k}\frac{\partial^2 \bar{u}_i}{\partial x_k \partial x_j}} - 2\nu\overline{\frac{\partial u_i'}{\partial x_k}\frac{\partial u_j'}{\partial x_k}\frac{\partial u_i'}{\partial x_j}}.
\end{aligned} \tag{A.60}$$

Appendix B

Derivation of non-linear stress strain relationship

The non-linear stress-strain relationship (2.35) was derived by Pope (1975) with the repeated use of the Caley-Hamilton theorem. In two-dimensions this theorem states

$$c_{ik}c_{kj} = c_{ij}c_{kk} - \frac{1}{2}\delta_{ij}\left[c_{ii}c_{jj} - c_{ik}c_{ki}\right]. \tag{B.1}$$

Substituting $c_{ij} = a_{ij} + b_{ij}$ into (B.1) gives

$$\begin{aligned}(a_{ik} + b_{ik})(a_{kj} + b_{kj}) = (a_{ij} + b_{ij})(a_{kk} + b_{kk}) \\ - \frac{1}{2}\delta_{ij}\left[(a_{ii} + b_{ii})(a_{jj} + b_{jj}) - (a_{ik} + b_{ik})(a_{ki} + b_{ki})\right]\end{aligned} \tag{B.2}$$

$$\begin{aligned}\underbrace{a_{ik}a_{kj}}_{I} + a_{ik}b_{kj} + b_{ik}a_{kj} + \underbrace{b_{ik}b_{kj}}_{II} = \underbrace{a_{ij}a_{kk}}_{I} + a_{ij}b_{kk} + b_{ij}a_{kk} + \underbrace{b_{ij}b_{kk}}_{II} \\ - \frac{1}{2}\delta_{ij}\left[\left(\underbrace{a_{ii}a_{jj}}_{I} + a_{ii}b_{jj} + b_{ii}a_{ii} + \underbrace{b_{ii}b_{jj}}_{II}\right) - \left(\underbrace{a_{ik}a_{ki}}_{I} + a_{ik}b_{ki} + b_{ik}a_{ki} + \underbrace{b_{ik}b_{ki}}_{II}\right)\right].\end{aligned} \tag{B.3}$$

Identifying that the Caley-Hamilto theorem holds for I and II, these vanish, leaving

$$a_{ik}b_{kj} + b_{ik}a_{kj} = a_{ij}b_{kk} + b_{ij}a_{kk} - \frac{1}{2}\delta_{ij}\left[(a_{ii}b_{jj} + b_{ii}a_{ii}) - (a_{ik}b_{ki} + b_{ik}a_{ki})\right] \tag{B.4}$$

$$a_{ik}b_{kj} + b_{ik}a_{kj} = a_{ij}b_{kk} + b_{ij}a_{kk} - \delta_{ij}\left[a_{ii}b_{jj} - a_{ik}b_{ki}\right] \tag{B.5}$$

Similarly as in (Pope, 1975) multiplying (B.5) by b_{ij} leads to

$$b_{ik}a_{kj}b_{jm} = -a_{ik}b_{kj}b_{jm} + a_{ij}b_{kk}b_{jm} + b_{ij}a_{kk}b_{jm} - b_{ij}\delta_{ij}\left[a_{ii}b_{jj} - a_{ik}b_{ki}\right]. \tag{B.6}$$

Identifying that the Caley-Hamilton theorem (B.1) can be used to express

$$a_{ik}b_{kj}b_{jm} = a_{ik}b_{km}b_{jj} - a_{ik}\frac{1}{2}\delta_{km}\left[b_{kk}b_{mm} - b_{kj}b_{jk}\right] \tag{B.7}$$

and

$$b_{ij}a_{kk}b_{jm} = a_{kk}b_{im}b_{jj} - a_{kk}\frac{1}{2}\delta_{im}\left[b_{ii}b_{mm} - b_{ij}b_{ji}\right], \tag{B.8}$$

(B.6) can be rewritten and simplified to

$$\begin{aligned} b_{ik}a_{kj}b_{jm} =& \underbrace{-a_{ik}b_{km}b_{jj} + a_{ik}\frac{1}{2}\delta_{km}\left[b_{kk}b_{mm} - b_{kj}b_{jk}\right]}_{=-a_{ik}b_{kj}b_{jm}} \\ &+ a_{ij}b_{kk}b_{jm} \\ &\underbrace{+a_{kk}b_{im}b_{jj} - a_{kk}\frac{1}{2}\delta_{im}\left[b_{ii}b_{mm} - b_{ij}b_{ji}\right]}_{=b_{ij}a_{kk}b_{jm}} \\ &- b_{ij}\delta_{ij}\left[a_{ii}b_{jj} - a_{ik}b_{ki}\right] \end{aligned} \tag{B.9}$$

$$\begin{aligned} b_{ik}a_{kj}b_{jm} =& - a_{ik}b_{km}b_{jj} + a_{ik}\frac{1}{2}\delta_{km}\left[b_{kk}b_{mm} - b_{kj}b_{jk}\right] \\ &+ a_{ij}b_{kk}b_{jm} \\ &+ a_{kk}b_{im}b_{jj} - a_{kk}\frac{1}{2}\delta_{im}\left[b_{ii}b_{mm} - b_{ij}b_{ji}\right] \\ &- b_{ij}\delta_{ij}\left[a_{ii}b_{jj} - a_{ik}b_{ki}\right] \end{aligned} \tag{B.10}$$

$$b_{ik}a_{kj}b_{jm} = \frac{1}{2}\left(a_{ik} - a_{kk}\right)\delta_{mi}\left[b_{mm}b_{ii} - b_{kj}b_{jk}\right] + b_{ij}\delta_{ij}a_{ik}b_{ki}. \tag{B.11}$$

Considering a general polynomial expressed as a finite number of successive multiplications of matrices in any order

$$P = A^{\alpha_1}B^{\beta_1}...A^{\alpha_2}B^{\beta_2}...A^{\alpha_r}B^{\beta_r} \tag{B.12}$$

were α_r and β_r are any positive integers and no two adjacent terms are powers of the same matrix. The order of the resulting polynomial is $\alpha_r + \beta_r$ in P, α_r in A and β_r in B.

Its order can be reduced by repeated substitution of the Cayley-Hamilton theorem from (B.1) and (B.11). If the partial order of P ($\alpha_r + \beta_r$) is greater than 1, repeated substitutions of (B.1) can be applied and if the order of P is larger than 2 the order can be reduced to less than 2 by repeated application of (B.11). The possible tensor functions of extension two ($a_{ik}b_{kj}$ and $b_{ik}a_{kj}$), given (B.4) only one is independent. The remaining independent base tensors are δ_{ij}, a_{ij}, b_{ij} and $a_{ik}b_{kj}$ or $b_{ik}a_{kj}$.

The invariants are formed by taking the trace of the base tensors and invariances used to reduce the order of P. The invariants are then a_{ii}, b_{ii}, $a_{ik}a_{ki}$, $b_{ik}b_{ki}$ and $a_{ik}b_{ki}$ or $b_{ik}a_{ki}$.

The tensor function can now be expressed as

$$\phi(a_{ij}, b_{ij}) = \sum_n g_n T^{(n)} = g_1 I + g_2 a + g_3 b + g_4 ab \tag{B.13}$$

with g_1, ..., g_4 being functions of the invariants.

Appendix C

Implementation and verification

The turbulence model proposed in chapter 3 was included into OpenFOAM (OF) with $k-\omega$ and $k-\varepsilon$ transport equations. Verification was done using the existent quadratic (ShihQuadraticKE) and cubic (LienCubicKE) non-linear models implemented in OF. As verification test case a backward facing step was used. This is a common selection for turbulence model analysis due to the well documented inaccuracies of reproducing the separation length.

C.1 Implementation

The implementation of the proposed model from chapter 3 is detailed in this section.

The first step for the implementation was the study of all non-linear models existent in OF. This search brought to light the quadratic model from Shih (1987) and the cubic model from Lien (1996). Disregarding the wall function that is used in the Lien model, the non-linear stress-strain relationship from these models is used as basis. The relationship is expanded using the tensors from Pope (1975) (2.36). The stress-strain relationship is added in such a way that it automatically propagates the correct Reynolds stresses into any other OF functions.

The OF implementation in its most basic form is a new function with output *nonlinearstress* in the Turbulence model *.C* file as

```
void <newTurbulenceModel>::correctNonlinearStress(const volTensorField &gradU)
{
    volScalarField tau_(1 / (omega_));// k-omega model
    volScalarField tau_(k / (epsilon_));// k-epsilon model

    volSymmTensorField S = tau_ * symm(gradU);
    volTensorField W = tau_ * (skew(gradU));

    // Base tensors
    volSymmTensorField T2 = twoSymm( S & W );
    volSymmTensorField T3 = dev( symm( S & S ) );
    volSymmTensorField T4 = dev( symm( W & W ) );
    volSymmTensorField T5 = twoSymm( W & ( S & S ) );
    volSymmTensorField T6 = dev2( twoSymm( symm( W & W ) & S ) );
```

```
    volSymmTensorField T7 = twoSymm( W & ( S & symm( W & W ) ) );
    volSymmTensorField T8 = twoSymm( ( S & W ) & ( S & S ) ) ;
    volSymmTensorField T9 = dev2( twoSymm( symm( W & W ) & ( S & S ) ) );
    volSymmTensorField T10 = twoSymm( W & ( ( S & S ) & symm( W & W ) ) );


    nonlinearStress_ = k_ * (
                            (b2_*T2 + b3_*T3 + b4_*T4) + //quadratic
                            (b5_*T5 + b6_*T6) + // cubic
                            (b7_*T7 + b8_*T8 + b9_*T9) + // cuartic
                            (b10_*T10)// quintic
                           );


    this->nut_ = k_/omega_; // k-omega
    this->nut_ = Cmu_ * sqr(k_)/epsilon_; k-epsilon
    this->nut_.correctBoundaryConditions();
}
```

The production term is updated as

```
volScalarField G
(
    this->GName(),
    (( nut_ * dev(twoSymm(tgradU())) - nonlinearStress_ ) && tgradU())
);
```

The new variables $b2\_$ to $b10\_$ need to be loaded into OF by being defined in the *.H* file

```
dimensionedScalar b2_;
```

and *.C* files

```
b2_
(
    dimensioned<scalar>::lookupOrAddToDict
    (
        "b2",
        this->coeffDict_,
        0
    )
),
```

The coefficients β are modified through a python routine for easier implementation of optimization routines as

```
# Modify turbulenceProperties file
# @param - targetDirectory: case file location
# @param - turbulenceModel: chose turbulence model
# @param - coefficients: coefficients for the turbulence model
# @return - write new turbulenceProperties file
def modifyTurbulenceProperties(targetDirectory, coefficients, turbulenceModel):

    file = ParsedParameterFile(target + "/constant/turbulenceProperties")
    file["RAS"]["RASModel"] = turbulenceModel

    coeffs.update({
            "b2": coefficients[0],
            "b3": coefficients[1],
            "b4": coefficients[2],
            "b5": coefficients[3],
            "b6": coefficients[4],
            "b7": coefficients[5],
            "b8": coefficients[6],
            "b9": coefficients[7],
            "b10": coefficients[8]
        })

    file["RAS"][turbulenceModel+"Coeffs"] = coeffs
    file.writeFile()
```

The OpenFOAM cases are run by loading the OF module into python and executing the following function

```
# Installation directory OpenFOAM
path = '. /opt/OpenFOAM/OpenFOAM-3.0.1/etc/bashrc;'

def runOpenFOAM(solver, caseDirectory, np=1):
    if np == 1:
        print 'Running ', solver, ' in series'
        print 'cd ' + caseDirectory + '; ' + solver
            + ' > log.' + solver
        p = subprocess.Popen(path + 'cd ' + case_dir + '; ' + solver
            + ' > log.' + solver, shell=True)
        p.wait()
    else:
        print 'Running ', solver, ' in parallel'
        print 'cd ' + case_dir + '; mpirun -np ' + str(np) + ' ' + solver
            + ' -parallel > log.' + solver
        os.system('cd ' + caseDirectory
            + '; decomposePar -force> log.decomposePar')
        os.system('cd ' + caseDirectory + '; mpirun -np ' + str(np) + ' '
            + solver + ' -parallel > log.' + solver)
        os.system('cd ' + caseDirectory
            + '; reconstructPar > log.reconstructPar')
```

C.2 Verification

The verification is divided in two two sections; 1) verification of implementation of non-linear stresses and 2) verification of calibration procedure.

C.2.1 Turbulence model verification

Turbulent flow over a backward facing step has established itself as a benchmark to evaluate turbulence model performance. The main challenge for turbulence models are to predict the reattachment length. The reattachment length is defined as the distance downstream from the step up to where the stream-wise velocity changes sign. An intuitive representation of this phenomenon is given in figure C.1. A vortex occurs right behind the step providing a flow pattern where the velocity experienced on the lower wall is in opposite direction to the free stream velocity. The point at which the velocity on the lower wall reverts back in the same direction as the free stream is defined as the reattachment point. The distance from the step to the reattachment point is the reattachment length. Turbulence models such as the $k-\varepsilon$ model are known to under-predict this distance by 20 to 25% (Demirdzic, 1982; Nallasamy, 1987; Abid, Speziale, & Thangam, 1991). This makes the backward facing step a good candidate to be used as verification case.

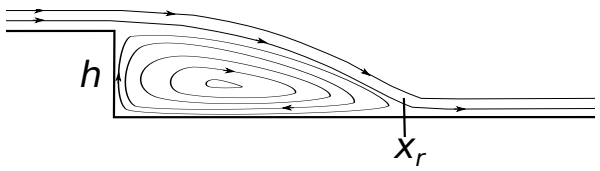

Figure C.1: Intuitive representation of the vortex experienced behind the step in a backward facing step flow and definition of reattachment length, defined as the distance between the step and x_r.

Figure C.2 shows the geometry used for verification. All length scales are expressed in terms of the step height h. The boundary conditions related to the faces of figure C.2 are given

in table C.1. The physical quantities are set such that the flow is fully developed at a step Reynolds number of $Re_h = 5,100$.

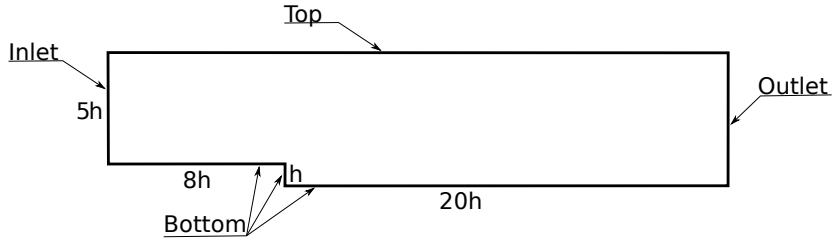

Figure C.2: Geometry of the backward facing step in terms of the step height h.

Table C.1: Boundary conditions of backward facing step

Face	Boundary condition
Inlet	Developed turbulent flow velocity inlet
Outlet	Pressure outlet
Top	Slip velocity
Bottom	No-slip wall

Verification was done in four steps, represented in figure C.3;

1. the non-linear stress-strain relationship is built in and tested whilst all coefficients $\beta = 0$,
2. the Shih quadratic $k - \varepsilon$ model is reproduced,
3. the Lien cubic $k - \varepsilon$ model is reproduced,

The proposed model overlaps exactly the existing linear, quadratic and cubic models from OpenFOAM, see figure C.3, thereby verifying the implementation has been done successfully.

C.2.2 Verification of calibration procedure

The calibration routine was verified by reproducing the Shih model on a square duct. A very simplified approach of only evaluating the Eddy viscosity (2.35) was set up. The minimization problem was as posed in section 3.2. The velocity, turbulent kinetic energy and turbulence dissipation were constant during the calibration. The initial conditions of the coefficients was $\beta_1 = \beta_2 = \beta_3 = 0$. The result of calibration is given in table C.2. Although the match is not perfect, the calibrated coefficients approach the Shih coefficients. The difference is likely to arise due to interactions between the first and third non-linear tensor of (2.36). The interactions are discussed in chapters 4 and 5.

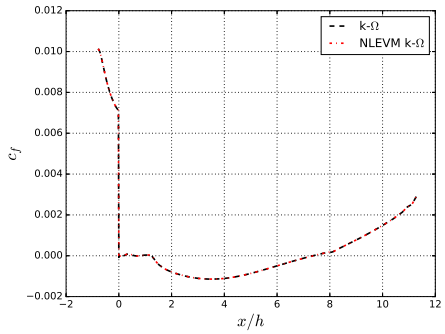

(a) Linear $k - \omega$

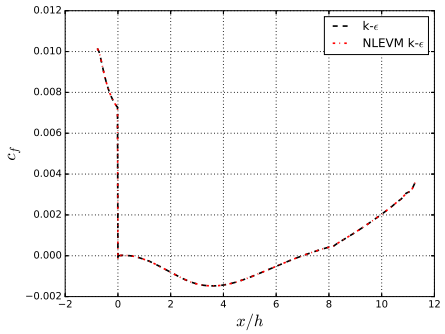

(b) Linear $k - \varepsilon$

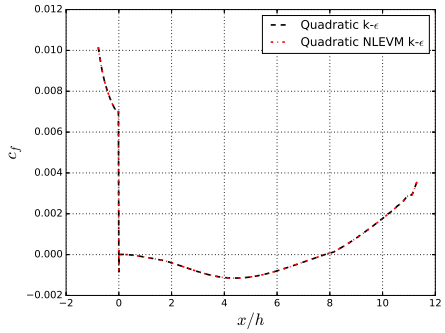

(c) Quadratic $k - \varepsilon$

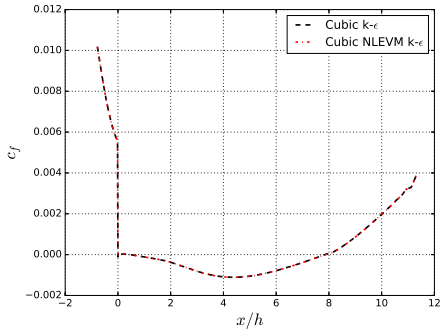

(d) Cubic $k - \varepsilon$

Figure C.3: Verification of implementation of non-linear Eddy viscosity model.

Table C.2: Shih coefficients and reproduced coefficients from calibration routine.

Coefficient	Shih	Calibrated
β_1	3	4.47
β_2	15	15
β_3	-19	-17.5

Appendix D

Barycentric map and realizability constraints

In this appendix the barycentric map from Banerjee et al. (2007) and realizability constraints presented in Schumann (1977) are introduced.

D.1 Barycentric map

An intuitive way of visualizing anisotropy is the anisotropy-invariant map (Lumley, 1970) or the barycentric map (Banerjee et al., 2007), used in this report. A barycentric map is essentially a triangle in which all turbulent flows can be classified depending on its state. The boundaries of the triangle also work as physical boundaries of turbulence properties, specifically the realizability constraints explained in the next section.

The three corners of the triangle are defined as the 1-, 2- and 3-component limiting states. Which mean 1, 2 and 3 eigenvalues of a_{ij} are non-zero respectively. The lines connecting these states are then defined as the axi-symmetric expansion, contraction and two-component limit. A fourth line, originating from the 3-component limiting state and going to in between the 1- and 2-component limiting state, is generally shown, which depicts the plane-strain. This fourth line is the isotropic turbulence state on which all Bousinesq approximation simulations lay. A typical barycentric map with explanations is depicted in Fig. D.1 (Banerjee et al., 2007).

The coordinates of a turbulence state on the barycentric map are calculated from

$$x = C_{1c}x_{1c} + C_{2c}x_{2c} + C_{3c}x_{3c}, \tag{D.1}$$

$$z = C_{1c}z_{1c} + C_{2c}y_{2c} + C_{3c}y_{3c}. \tag{D.2}$$

Where C_{1c} to C_{3c} are determined by the eigenvalues ($\lambda_{1 \text{ to } 3}$) of a_{ij} as

$$C_{1c} = \lambda_1 - \lambda_2, \tag{D.3}$$
$$C_{2c} = 2\left(\lambda_2 - \lambda_3\right), \tag{D.4}$$
$$C_{3c} = 3\lambda_3 + 1. \tag{D.5}$$

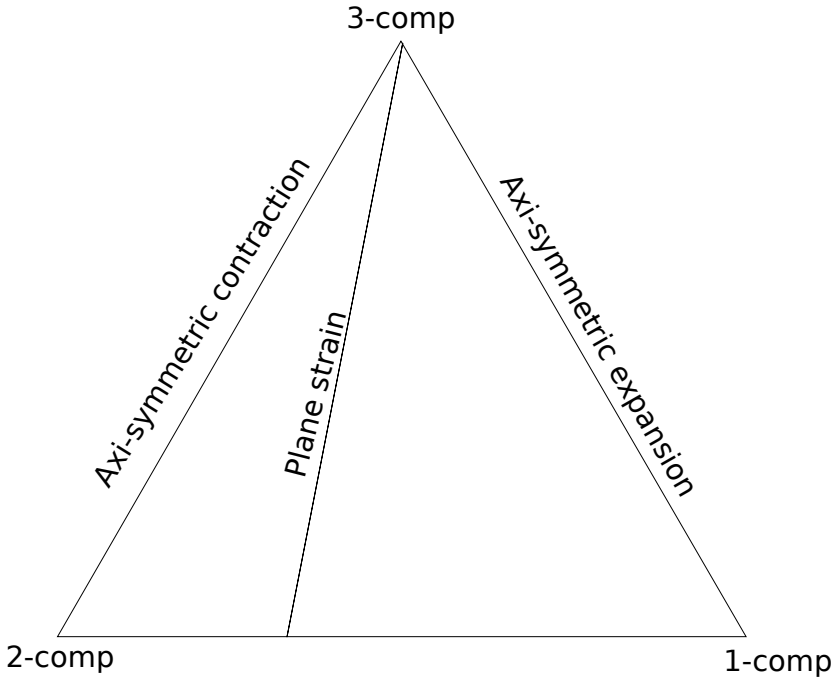

Figure D.1: Barycentric map adapted from (Banerjee et al., 2007).

D.2 Realizability constraints

The realizability constraints presented in Schumann (1977) stipulate that the Reynolds stress tensor τ_{ij} be Symmetric Positive semi-Definite (SPD). This is a necessary condition for real velocities and to satisfy the Schwarz inequality. Then the Reynolds stress tensor has to satisfy the following conditions:

- $\tau_{ij} = \tau_{ji}$
- $\tau_{ii} \geq 0$
- $\det(\tau_{ij}) \geq 0$
- $\tau_{ij}^2 \geq \tau_{ii}\tau_{jj}$.

Appendix E

Wall treatment

Turbulence models used for RANS simulations generally require one of two conditions; 1) a mesh resolution of $y^+ < 1$ or 2) the use of wall functions. If a mesh resolution of $y^+ < 1$ is chosen the first cell is well within the viscous sublayer of the boundary allowing the turbulence model to resolve all features of the boundary layer. This however can be prohibitively expensive since it requires very fine meshes near walls. Therefore wall functions have been introduced. These generally require a resolution of at least $30 < y^+ < 300$ for good results. Wall functions are based on the law of the wall. This one states that the average velocity u^+ of a turbulent flow near the wall is proportional to the logarithm of the distance to the wall y^+ as shown in figure E.1[1] (von Karman, 1931). Two regions can be identified, inner region composed of a viscous sublayer, buffer layer and log-law layer and the outer layer. The viscous sub-layer

$$u^+ = y^+ \tag{E.1}$$

is modeled as one cell with this cell height commonly being defined by $y^+ = 20$ or 30. The log-law

$$u^+ = \frac{1}{\kappa} \ln y^+ + B \tag{E.2}$$

stretches from the first cell height to about $y^+ \approx 150$. κ in (E.2) is the von Karman constant $\kappa \approx 0.41$ and B is a constant often chosen as 5.1. The non-dimensional velocity u^+ is defined as

$$u^+ = \frac{u}{u_\tau} \tag{E.3}$$

with

$$u_\tau = \sqrt{\frac{\tau_w}{\rho}} \tag{E.4}$$

where τ_w is the wall shear stress.

[1] Retrieved on 12/03/2018 from: https://en.wikipedia.org/wiki/Law_of_the_wall#/media/File:Law_of_the_wall_(English).svg

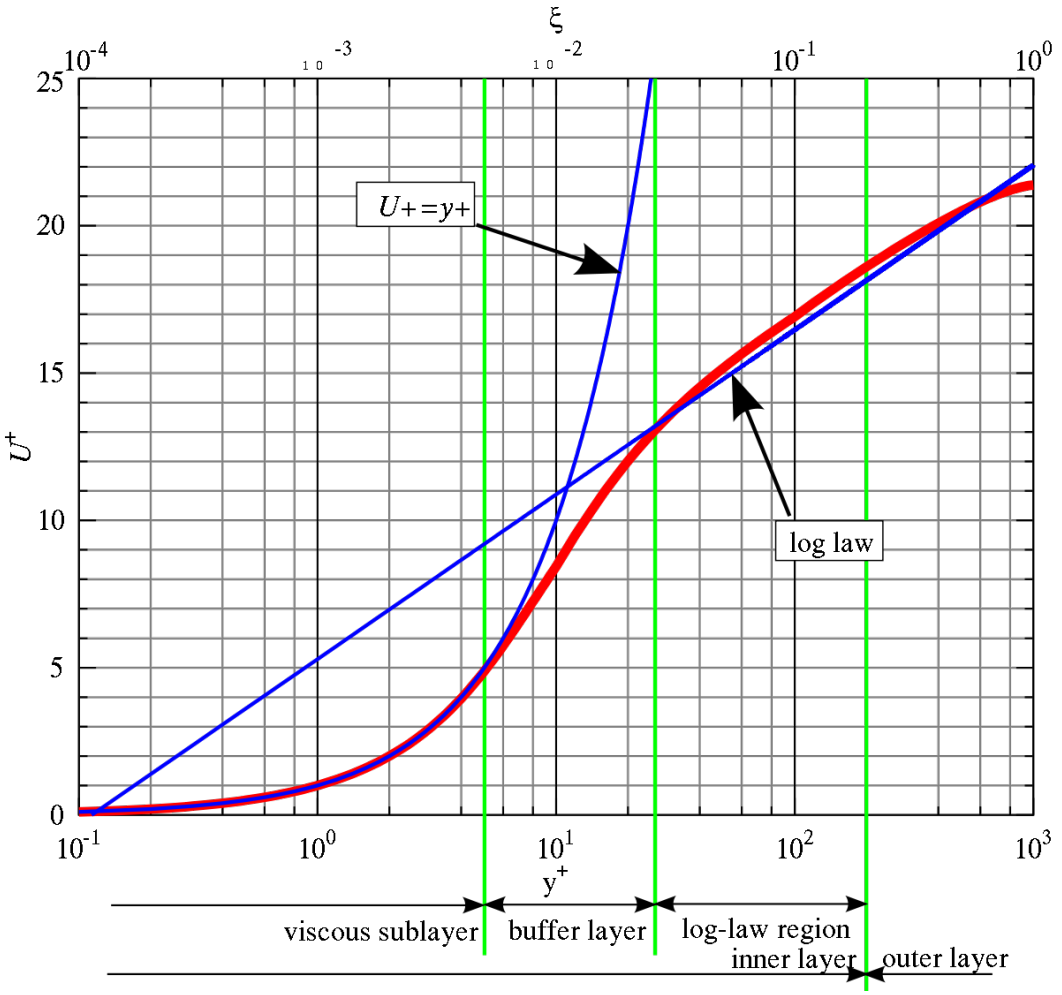

Figure E.1: Near wall behavior of flow velocity. Two regions are identified, inner and outer region. The inner region is composed of the viscous sublayer, buffer layer and log-law layer. The viscous sublayer is modeled by the first cell, then the log-law is used up to $y^+ \approx 150$. No wall function remains in the outer region.